Adsorbate Structures and Catalytic Reactions Studied in the Torr Pressure Range by Scanning Tunneling Microscopy

by

Kevin Shao-Lin Hwang

B.A. (Rice University) 1999

A dissertation submitted in partial satisfaction of the

requirements for the degree of

Doctor of Philosophy
in

Chemistry

in the

GRADUATE DIVISION

of the

UNIVERSITY OF CALIFORNIA, BERKELEY

Committee in charge:

Professor Gabor A. Somorjai, Chair
Professor Alex Pines
Professor Michael Crommie

Spring 2003

The dissertation of Kevin Shao-Lin Hwang is approved:

_____

Chair Date

_____

Date

_____

Date

University of California, Berkeley

Spring 2003

Adsorbate Structures and Catalytic Reactions Studied in the Torr Pressure Range by Scanning Tunneling Microscopy

by

Kevin Shao-Lin Hwang

Abstract

Adsorbate Structures and Catalytic Reactions Studied in the Torr Pressure Range by Scanning Tunneling Microscopy

by

Kevin Shao-Lin Hwang

Doctor of Philosophy in Chemistry

University of California, Berkeley

Professor Gabor A. Somorjai, Chair

High-pressure, high-temperature scanning tunneling microscopy (HPHTSTM) was used to study adsorbate structures and reactions on single crystal model catalytic systems. Studies of the automobile catalytic converter reaction [$CO + NO \rightarrow 1/2\ N_2 + CO_2$] on Rh(111) and ethylene hydrogenation [$C_2H_4 + H_2 \rightarrow C_2H_6$] on Rh(111) and Pt(111) elucidated information on adsorbate structures in equilibrium with high-pressure gas and the relationship of atomic and molecular mobility to chemistry.

STM studies of NO on Rh(111) showed that adsorbed NO forms two high-pressure structures, with the phase transformation from the (2 × 2) structure to the (3 × 3) structure occurring at 0.03 Torr. The (3 × 3) structure only exists when the surface is in equilibrium with the gas phase. The heat of adsorption of this new structure was determined by measuring the pressures and temperatures at which both (2 × 2) and (3 ×

3) structures coexisted. The energy barrier between the two structures was calculated by observing the time necessary for the phase transformation to take place.

High-pressure STM studies of the coadsorption of CO and NO on Rh(111) showed that CO and NO form a mixed (2 × 2) structure at low NO partial pressures. By comparing surface and gas compositions, the adsorption energy difference between top-site CO and NO was calculated. Occasionally there is exchange between top-site CO and NO, for which we have described a mechanism for. At high NO partial pressures, NO segregates into islands, where the phase transformation to the (3 × 3) structure occurs.

The reaction of CO and NO on Rh(111) was monitored by mass spectrometry (MS) and HPHTSTM. From MS studies the apparent activation energy of the catalytic converter reaction was calculated and compared to theory. STM showed that under high-temperature reaction conditions, surface metal atoms become mobile.

Ethylene hydrogenation and its poisoning by CO was also studied by STM on Rh(111) and Pt(111). Poisoning was found to coincide with decreased adsorbate mobility. Under ethylene hydrogenation conditions, no order is detected by STM at 300 K, as hydrogen and ethylidyne, the surface species formed by gas-phase ethylene, are too mobile. When CO is introduced, the reaction stops, and ordered structures appear on the surface. For Rh(111), the structure is predominantly a mixed c(4 × 2), though there are some areas of (2 × 2). For Pt(111), the structure is hexagonal and resembles the Moiré pattern seen when Pt(111) is exposed to pure CO. From these studies it is concluded that CO poisons by stopping adsorbate mobility. This lack of adsorbate mobility prevents the adsorption of ethylene from the gas phase by hindering the creation of adsorption sites.

Dedicated to my parents, Warren and Cordelia Hwang.

Table of Contents

List of Figures

Acknowledgements

There have been many people who have helped me achieve my goal of earning a Ph.D. First I would like to thank my research advisor, Professor Gabor Somorjai, for giving me the opportunity me to work in his research group. His vision and support over the last four years were invaluable. I would also like to thank Dr. Miquel Salmeron for his advice and guidance. His knowledge of STM was critical in obtaining and interpreting the results described in this dissertation.

The help and friendship of past and present members of the Somorjai and Salmeron groups were essential in helping me finish graduate school. Keith Rider introduced me to both UHV and STM, while providing guidance on how to be a successful graduate student. David Tang and Max Montano, who also worked with me on STM projects, will now comprise the HPHTSTM team. Others who deserve thanks are Kaori Kitano, Mark Rose, Frank Ogletree, Yong Chen, Craig Tewell, Saskia Hoffer, Keith McCrea, Ji Zhu, Aric Opdahl, Minchul Yang, Steve Baldelli, Jeff Grunes, Telly Koffas, Rob Rioux, Staffan Westerberg, Sasha Kweskin, Anthony Contreras, and especially Jessica Gaughan, who also critically read parts of this dissertation.

The staffs at the U. C. Berkeley College of Chemistry and Lawrence Berkeley National Laboratory were very helpful. I would like to particularly thank Inger Coble, Carmen Ross, Jim Severens, Eric Gravilund, Henry Chan, Chip Flor, and Peter Ruegg.

My friends outside the lab made sure that I did not spend the last four years only doing research. My thanks goes to Steve Robertson, Stephen Prilliman, Jeremy and Dennise Templeton, Sean O'Rourke, Todd Thompson, Aaron Pierce, Chelsea Valdes-

Pierce, Ed Feng, Erik Scher, Brendan Cowles, Dan and Erin Sandler, and especially Dennis and Cheryl Geels.

Finally I would like to thank my parents. Despite their encouragement to pursue any educational direction I wanted, I followed in their footsteps to earn an advanced degree in chemistry. All along the way they have provided their love and support, and they deserve most of the credit for where I am today.

Chapter 1: Introduction

Surface science is the study of interfaces involving condensed phases. There are a wide variety of everyday phenomena that involve surfaces: friction at the solid-solid interface is responsible for the movement of tires, the forming of dew on a window involves the gas-solid interface, evaporation occurs at the gas-liquid interface. There are also important biological interfaces, such as the surface of implants with regards to bio-rejection.

It is important to recognize that surfaces often behave much differently than bulk materials. Metals, for example, will often reconstruct at the surface so the metal atoms there order differently than those in the bulk [1]. Polymers can change their configuration to have hydrophobic or hydrophilic groups near the surface, depending on which is more energetically favorable [2].

An industrially important area of surface science is heterogeneous catalysis. In heterogeneous catalysis, the catalyst, which is usually a solid, interacts with reactants and products in a different phase--gas or liquid. The purpose of the catalyst is to enhance the activity, meaning the amount of product produced, or selectivity, the ratio of products for systems that have more than one possible reaction. Metal heterogeneous catalysts are used today for many purposes, including refining hydrocarbons from petroleum and synthesizing ammonia.

Surface physical chemists studying heterogeneous catalysts are concerned with the structure and composition of the catalyst before, during, and after the reaction. Other issues are the conditions of pressure and temperature under which the catalysis can occur and the rate of the possible reactions.

Studying an actual catalyst used in industry can be quite complicated, as they are often metals of unknown surface structure supported on oxides. In surface science, model catalysts are often used instead. While these are simplified versions, data obtained by studying them is often easier to interpret. Metal single crystals are often used as model catalysts. They provide a uniform surface that is catalytically relevant as industrial catalysts often contain metal particles that are not amorphous, but instead have many facets that are single crystals.

In this work, Rh(111) and Pt(111) single crystals are used. Rhodium and platinum are both face-centered cubic metals. This means that their repeating unit cell consists of a cube with atoms at each corner and at the center of each face, as shown in Figure 1.1. A single crystal will have a different structure depending on the angle it is cut relative to the unit cell. The Miller indices (hkl) determine how the plane of each layer of a crystal intersects the unit cell, and thus its structure. The (111) face, shown in Figure 1.2 along with two other commonly studied crystal surface structures, is the most energetically stable state and should thus be abundant in real catalytic systems.

Much of the work in this dissertation involves studying the surface structures that molecules form on the metal surface. The surface structure of Rh(111) and Pt(111) is hexagonal with a unit cell designated as (1 × 1). Molecules or atoms adsorbed or bound to the surface will often form an ordered structure with a repeating unit cell. This adsorbate unit cell is described relative to the unit cell of the substrate, with (2 × 2) indicating that each side of the adsorbate unit cell is twice as long as that in the metal unit cell. Sometimes the unit cell is rotated with respect to the substrate, such as ($\sqrt{3}$ ×

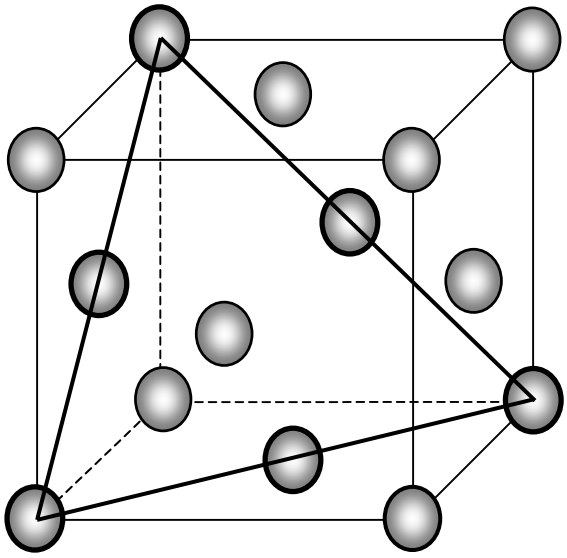

Figure 1.1 The unit cell of a face centered cubic crystal structure. The atoms making up the (111) surface plane are heavily outlined.

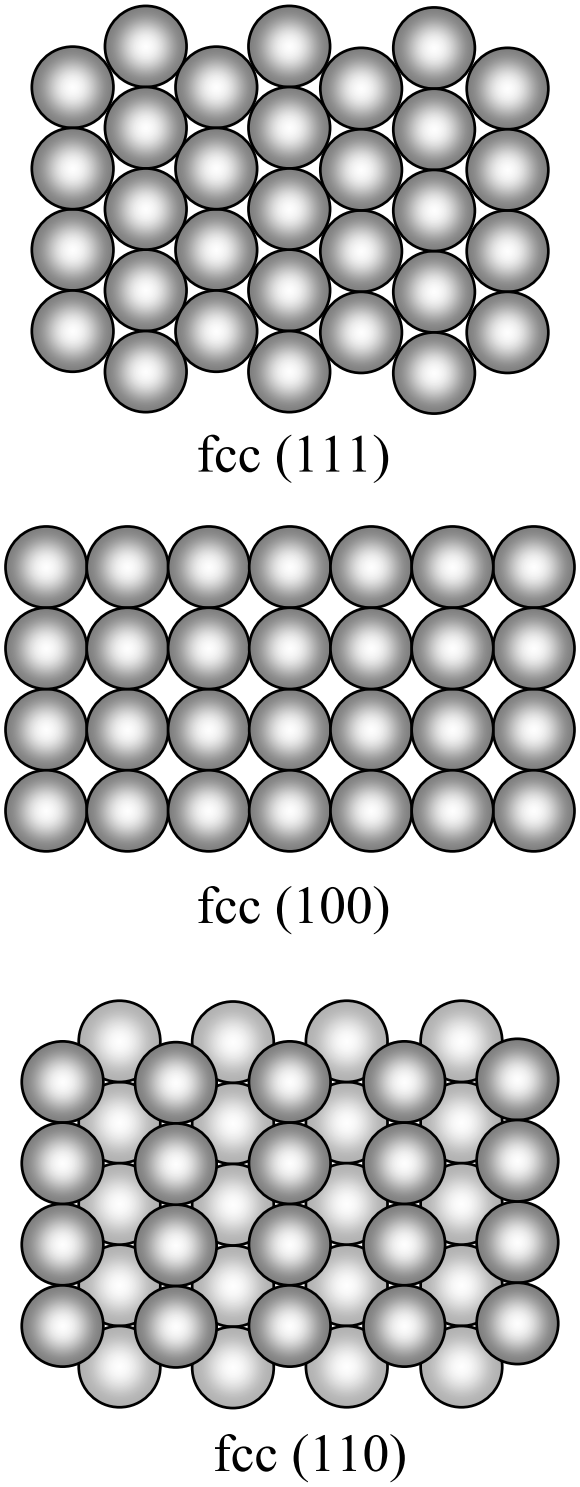

Figure 1.2 Top views of three low-miller-index structures of an fcc crystal.

$\sqrt{3}$)R30º, which indicates a unit cell rotated 30º with respect to the substrate where each side is $\sqrt{3}$ times the length of the metal unit cell. It is important to remember that unless otherwise specified, the adsorbate unit cell always has the same shape as that of the substrate. A c(4 × 2) unit cell, a (4 × 2) unit cell with a molecule or atom in the center of the cell, for example, may not be the most intuitive way to describe the rectangular looking adsorbate layer. The three preceding adsorbate structures are shown in Figure 1.3.

There are over 70 surface science techniques available for determining surface structure and composition before and after a catalytic reaction [3]. Some common techniques that have been extensively used include temperature programmed desorption (TPD), which gives molecular binding energies, low energy electron diffraction (LEED), which gives surface structure, Auger electron spectroscopy (AES), which gives atomic surface composition, and electron energy loss spectroscopy (EELS), which gives molecular vibrations [4].

While the techniques given above can give a powerful and complete picture of a surface, they can only operate in low pressure (< 1×10^{-4} Torr). Traditionally surface science experiments have been done in ultrahigh vacuum (UHV). In this pressure range of less than 10^{-9} Torr, not only can electron-based experimental techniques work, but also the surface will remain free of contaminants for over an hour, long enough to study with surface science techniques. This can be seen from the kinetic theory of gases:

$$F = \frac{N_A P}{\sqrt{2\pi MRT}}$$

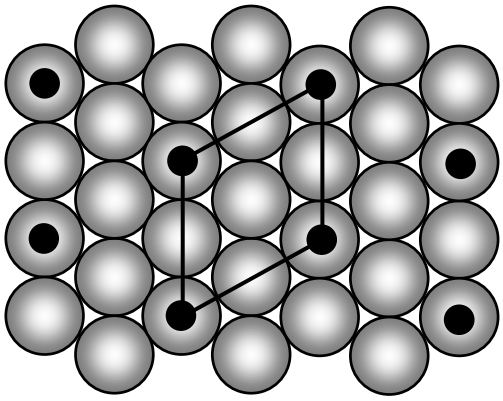

(2×2)

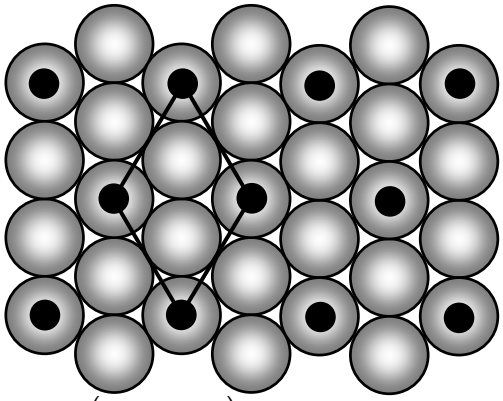

$\left(\sqrt{3} \times \sqrt{3}\right)$ R30º

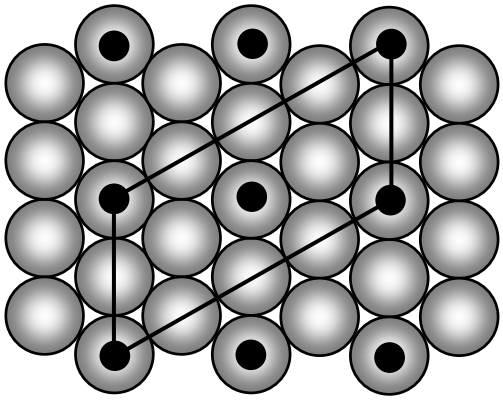

c(4 × 2)

Figure 1.3 Examples of notation used to describe adsorbate structures.

where F is the flux of molecules striking the surface, and M is the molecular mass of these molecules. Since the surface of a solid has on the order of 10^{15} atoms cm^{-2}, keeping a surface clean for an hour requires a flux less than about 10^{12} molecules cm^{-2} s^{-1}. Calculating for typical molecules such as CO at room temperature, a pressure less than 10^{-9} Torr is necessary.

Traditionally, for reaction studies, surface science reaction experiments have been done using a high-pressure reaction cell attached to the vacuum chamber. The sample can be cleaned in UHV before being transferred to the reaction cell. After the reaction, the sample is transferred back to the UHV chamber for analysis. During the reaction, the surface is not studied, while progress of the reaction can be monitored by analyzing the gases using techniques such as gas chromatography (GC).

This, of course, means that the surface itself is not characterized during the reaction. In some cases reaction condition data can be extrapolated from low-pressure, low-temperature data, but in these cases the surface is not in equilibrium with the gas phase and the surface molecules are kinetically frozen. For many years there was a "pressure gap" that existed from the high pressures of real catalytic reactions and the low pressures where surface science instrumentation worked.

In recent years, surface physical chemists have developed techniques that allow one to probe the surface under reaction conditions. Sum-frequency generation (SFG) is an inherently surface sensitive vibrational spectroscopy that has been used to study heterogeneous catalysis under reaction conditions [5], as well as biologically important systems such as contact lenses [6] and protein adsorption related to implant rejection [7]. Unlike infrared spectroscopy, SFG generates no signal from centrosymmetric media.

This means that it does not suffer as much from gas phase absorption and probes only the surface, where symmetry is broken, as most materials are centrosymmetric.

Another promising technique is high-pressure x-ray photoelectron spectroscopy (XPS) [8]. XPS is related to AES and also gives atomic surface composition. It is possible to differentially pump an electron analyzer, keeping the pressure it sees low while still examining a surface exposed to gas in the Torr pressure range. Preliminary results suggest this will be an important technique for studying heterogeneous catalysis.

Neither of the two previous techniques gives surface structure. It is possible to use grazing-angle x-ray diffraction to get this information on metals, but the scattering cross section of important adsorbates such as carbon and oxygen is too low for the technique to be useful for studying heterogeneous catalysis. Scanning tunneling microscopy (STM) can be used under high pressure to study surface structure at the atomic level [9]. The purpose of this research project is to study catalytic systems such as the automobile catalytic converter and ethylene hydrogenation under realistic temperature and pressure conditions. In this way we can learn how molecules arrange and react under high pressure and see if this is different from analogous low-pressure studies.

This dissertation describes experiments performed from 1999 to 2003 using a high-pressure, high-temperature STM. Chapter 2 is an introduction to the technique of STM. Our experimental apparatus and complementary experimental techniques are described in Chapter 3. Chapters 4 and 5 describe results obtained from experiments on a model system for catalytic converter reactions. NO on Rh(111) was found to form a new structure under high-pressure conditions. This result, described in Chapter 4, was one of

the first indicating that low-pressure results cannot always be extrapolated to the high pressures under which catalytic reactions take place. Chapter 5 discusses adsorbate structures of CO and NO on Rh(111), while Chapter 6 discusses their reactions. While analysis of adsorbate structures led to interesting conclusions on adsorbate mobility, reaction studies were limited in that at the elevated temperatures necessary to obtain enough products to monitor using a mass spectrometer, molecular resolution was lost. This led us to study ethylene hydrogenation, which is fast enough at room temperature to track using mass spectrometry. Chapter 7 discusses reaction studies and surface structures on Rh(111) and Pt(111) during ethylene hydrogenation and when the reaction was poisoned with CO. We found that CO poisons ethylene hydrogenation by stopping adsorbate mobility on the surface. Conclusions and future directions for research are given in Chapter 8.

References

(1) Chan, C. M.; Van Hove, M. A.; Weinberg, W. H.; Williams, E. D. *Surface Science* **1980**, *91*, 440-448.

(2) Chen, Z.; Ward, R.; Tian, Y.; Baldelli, S.; Opdahl, A.; Shen, Y. R.; Somorjai, G. A. *Journal of the American Chemical Society* **2000**, *122*, 10615-10620.

(3) Somorjai, G. A. *Introduction to Surface Chemistry and Catalysis*; John WIley & Sons: New York, 1994.

(4) Woodruff, D. P.; Delchar, T. A. *Modern Techniques of Surface Science*; 2nd ed.; Cambridge University Press: Cambridge, 1994.

(5) McCrea, K. R.; Parker, J. S.; Somorjai, G. A. *Journal of Physical Chemistry B* **2002**, *106*, 10854-10863.

(6) Kim, S. H.; Opdahl, A.; Marmo, C.; Somorjai, G. A. *Biomaterials* **2002**, *23*, 1657-1666.

(7) Kim, J.; Somorjai, G. A. *Journal of the American Chemical Society* **2003**, *125*, 3150-3158.

(8) Bluhm, H.; Ogletree, D. F.; Fadley, C. S.; Hussain, Z.; Salmeron, N. *Journal of Physics-Condensed Matter* **2002**, *14*, L227-L233.

(9) McIntyre, B. J.; Salmeron, M.; Somorjai, G. A. *Rev. Sci. Instrum.* **1993**, *64*, 687-691.

Chapter 2: Scanning Tunneling Microscopy

Scanning Tunneling Microscopy (STM) is a technique that allows one to achieve atomic or molecular resolution of a conducting or semiconducting surface. It was invented in the early 1980's by Gerd Binnig and Heinrich Rohrer [1,2], and they received the Nobel Prize in physics in 1986 for their invention. STM is a scanning probe microscopy where a sharp, metal tip is in close proximity to the surface. An advantage over optical microscopies is that working in the near-field regime allows for spatial resolution that is not wavelength limited. It is unique in that it is able to give such high resolution under varying conditions, from ultra-high vacuum (UHV) of 1×10^{-10} Torr [3,4] to aqueous environments [5]. On metals, which STM was first used on, metal surface structure and reconstructions can be examined [3]. Adsorbates surface structures [3] and single molecules [6] can also be studied. Today, STM can be used to study a wide range of systems, including semiconductor [3], biological [7], and electrochemical [8] systems. One of the recent advances of STM is the ability to work in controlled high-temperature, high-pressure conditions, which allows one to study systems more closely related to industrial heterogeneous catalysis [9-13]. This chapter discusses theoretical and experimental aspects of STM.

2.1 Theory

STM operates by measuring the current caused by electrons tunneling between two conductors. Classically, electrons in a metal are confined by a potential barrier. Quantum mechanically, the electronic wavefunctions of a conductor will leak out of their potential well. Bringing these wavefunctions within a few angstroms of each other

allows for wavefunction overlap and quantum mechanical tunneling if a potential is applied between the two conductors. The current that flows across a gap "d" can be expressed as

$$I \propto Ve^{-2Kd},$$

where K is the inverse decay length given by

$$K = \hbar^{-1}\sqrt{2m\phi}.$$

In the previous equation, "m" is the mass of the tunneling electron and ϕ is the effective local work function, which is the average of the effective work functions of the tip and sample. The exponential relationship between current and distance means that the current decreases by an order of magnitude when the gap "d" is changed by only 1 Å. This is what allows the atomic resolution achieved by STM.

In practice this tunneling occurs between a conducting surface and a metal tip. This tip is macroscopically extremely sharp, but on the molecular level it has a radius of curvature on the order of 10 Å, as shown in Figure 2.1. While the ideal tip would be a perfect cone or pyramid terminating in a single atom, many tips of varying and usually unknown shapes are able to produce images of atomic resolution. This is due to the exponential relationship between distance and tunneling described above. As long as one atom of the tip extends slightly further than any other, tunneling current will preferentially flow through that atom.

In addition to the distance between the tip and surface, the electronic structures of the two also need to be considered. The STM current does not purely give the topography of the surface. A more detailed examination of the tunneling current [4], shows that it represents the local density of states (LDOS) at the Fermi level, or the

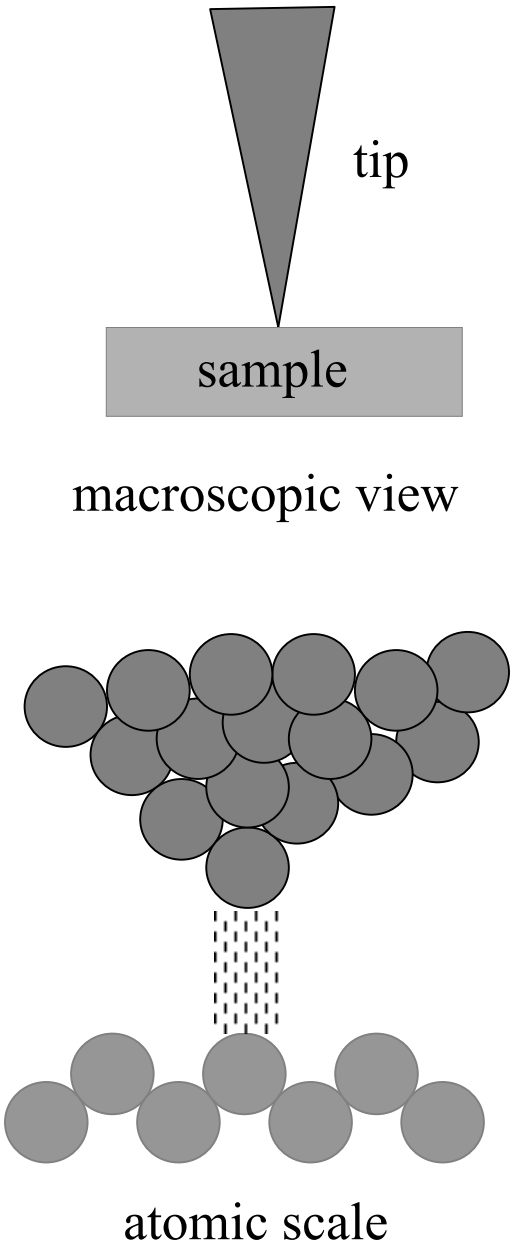

Figure 2.1 Macroscopic and microscopic views of the STM tip-sample junction. The dotted lines indicate the tunneling of electrons.

electron density at the Fermi level, at the position of the tip. For a metal, the LDOS is similar to the electron density and hence STM images resemble topography. Adsorbates though, can modify the LDOS at the Fermi level due to their electronic orbitals.

There are two modes of operation possible for the STM: positive and negative bias, as shown in Figure 2.2, where the bias is designated ΔE. These refer to how the tip is biased relative to the sample. In positive bias, described on the right, electrons flow from the occupied states of the tip into unoccupied states of the sample. The only states that participate are those with energy between the Fermi levels of the sample and tip, denoted here as E_F and $E_F + \Delta E$, respectively. In negative bias, electrons flow from the occupied states of the sample into the unoccupied states of the tip. States with energies between E_F and $E_F - \Delta E$ participate in this case.

2.2 Experimental Considerations

Piezoelectric materials (piezos), such as quartz, are what enabled STM to move from a theoretical device to a practical one. One of the difficulties in doing STM is keeping the tip a fixed distance away from the surface with a precision of less than an angstrom. Piezos are ferroelectric materials that can be polarized by applying a large voltage across them while heating. Once the ferroelectric domains have aligned along a certain direction, piezos will contract or expand when a voltage is applied across them, or vice versa, as shown in Figure 2.3. Piezos can reproducibly move with sub-angstrom precision as long as they are not heated above their Curie temperature. Combining multiple piezos enables one to have precise translational control in three dimensions.

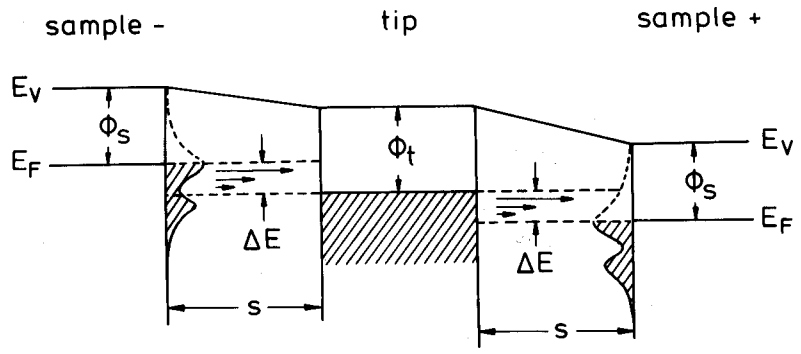

Figure 2.2 Energy diagram of tunneling for both positive and negative sample bias. The shaded areas represent filled states. From [3].

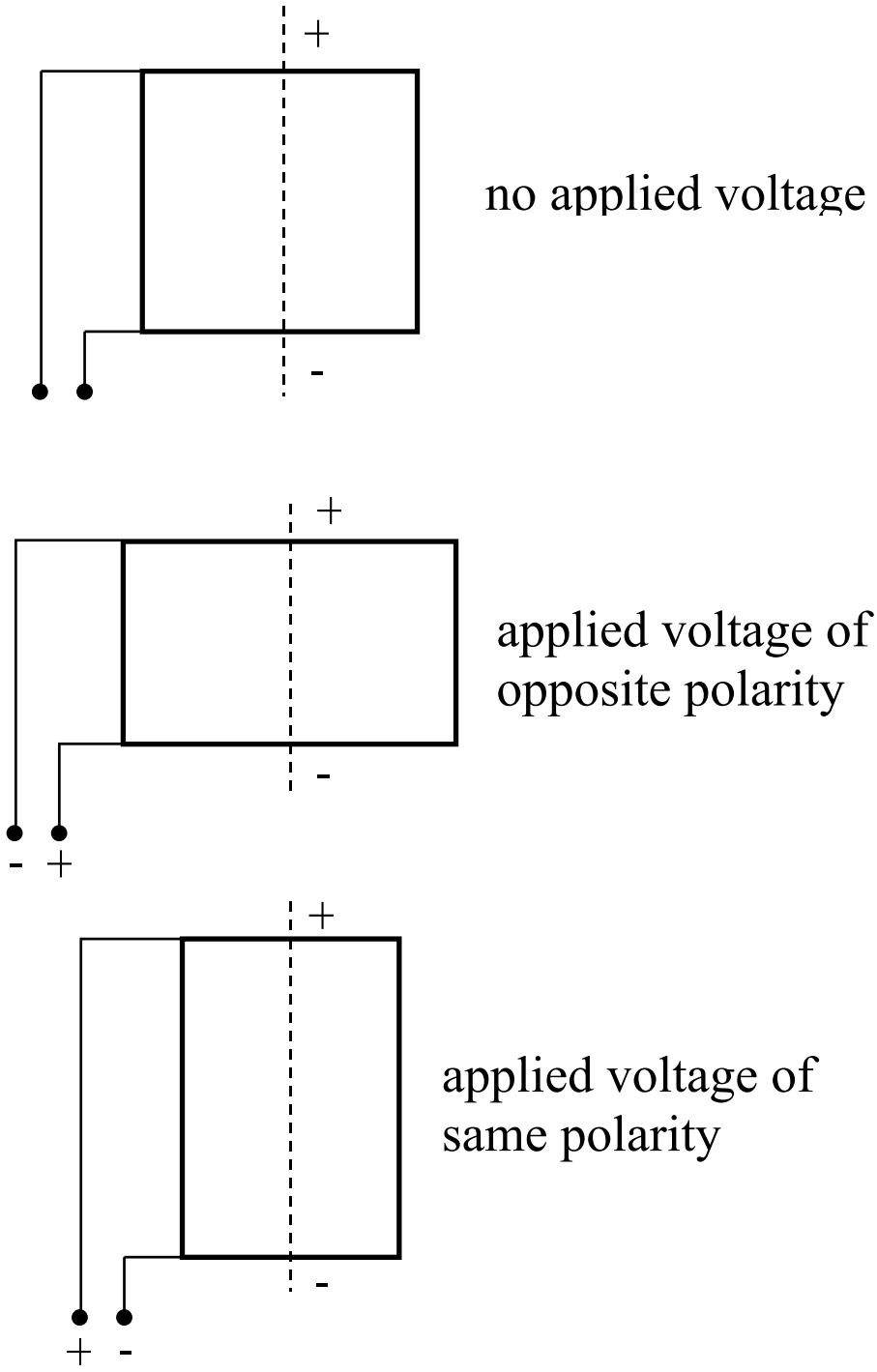

Figure 2.3 Piezoelectric deformation caused by an applied voltage.

STM is powerful in that many different types of experiments can be performed with the same instrumentation depending on the scan mode chosen. Topography, spectroscopy, and work function studies are some examples. Two common scan modes for obtaining topographic information are constant-current and constant-height, as shown in Figure 2.4. Both involve rastering the tip across the surface. In constant-current mode, a feedback loop attempts to keep the current (usually between 0.1 and 10 nA) constant as the tip is rastered across the surface at about 1 Å/ms in the x-direction and 1 Å/s in the y-direction. If the tip moves to an area that is further away from the tip in the z-direction, the current will drop. In response, the feedback loop will indicate that the tip should move closer to the surface to return the current to its previous level. Similarly, moving to an area closer to the tip will cause the tip to pull back. Tracking the movement of the tip allows the STM to give an image of the constant-current map of the surface.

In constant-height mode, the tip is simply rastered across the surface while kept at the same z-position, and the current change is measured. From this the constant-current map of the surface can be calculated. The advantage to working in constant-height mode is that scans can be done up to three orders of magnitude faster than in constant-current mode, as the feedback loop time-constant is decreased. A disadvantage is that there is a risk of damaging the tip unless the surface is very flat. Any significant protrusions will touch and possibly destroy the tip.

The actual resolution achievable with a given STM depends on the noise in the system, including electrical, vibrational, and chemical noise. With the tunneling current as small as 0.1 nA, amplification by many orders of magnitude is necessary before it can be sent from the STM to the processing electronics without significant loss. Before this

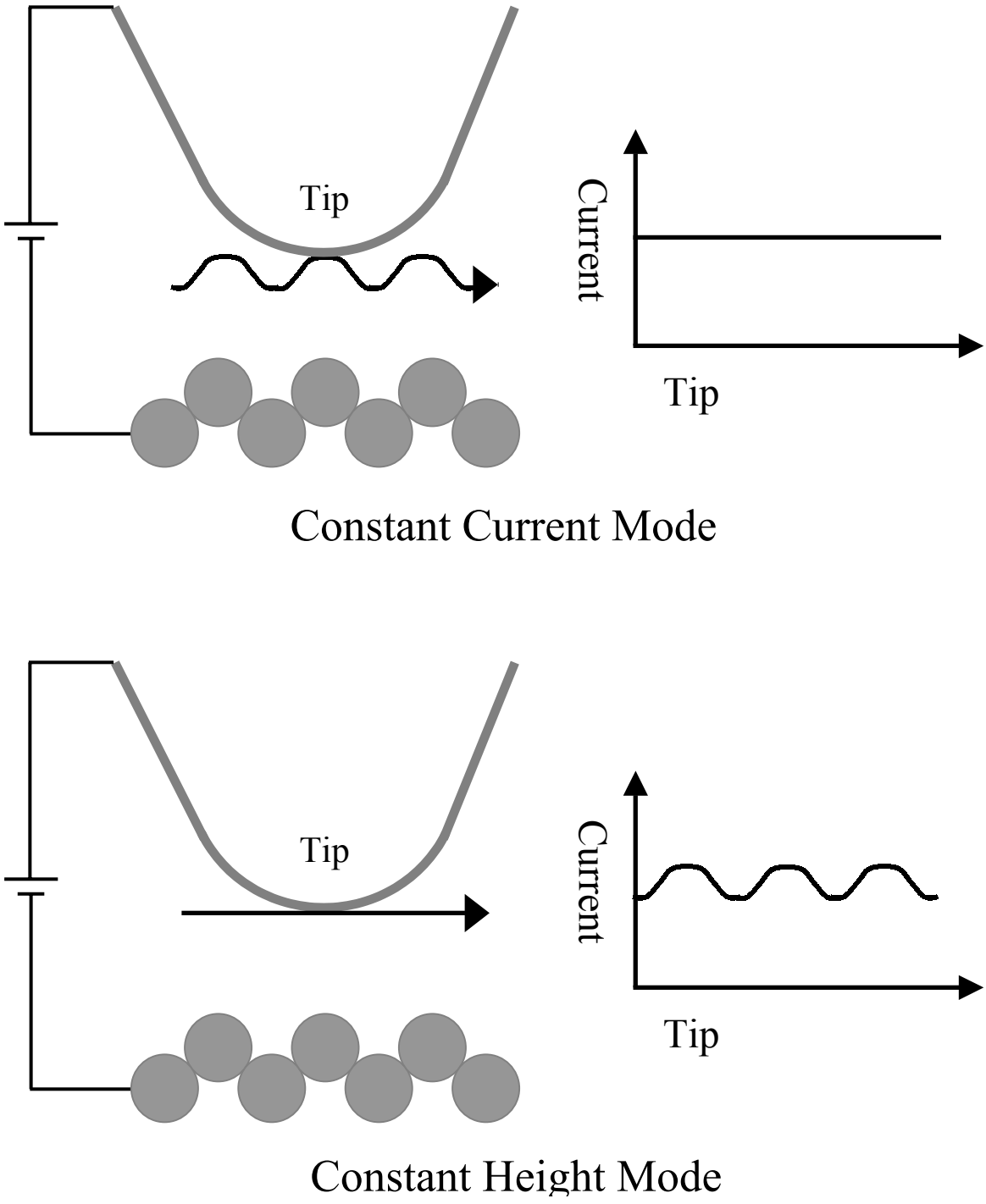

Figure 2.4 Two common scanning modes of STM.

amplification, any extrinsic electrical signals present will cause significant electrical noise that can obscure the true tunneling current. Ground loops and coiled cables can also introduce electrical noise.

Mechanical vibrations can also cause noise problems in an STM. Vibrational noise can occur from loose components of the STM itself or building vibrations propagating through the STM apparatus. A well-designed STM can compensate for some vibrations by being small and rigid. Various vibration isolation and dampening devices are also usually used in an effort to minimize vibrational noise.

A third source of noise is chemical noise, which is due to molecules moving through the tunneling gap. This is not a large problem for experiments done under low temperature and pressure conditions, where there are few gas molecules and diffusion rates are low. Under high pressure, however, chemical noise can become the largest source of noise, as the tunneling probability will change depending on how clean the gap is.

References

(1) Binnig, G.; Rohrer, H.; Gerber, C.; Weibel, E. *Physical Review Letters* **1982**, *49*, 57-61.

(2) Binnig, G.; Rohrer, H.; Gerber, C.; Weibel, E. *Applied Physics Letters* **1982**, *40*, 178-180.

(3) Guntherodt, H.-J.; Wiesendanger, R., Eds. *Scanning Tunneling Microscopy I*; Springer-Verlag: Berlin, 1992.

(4) Wiesendanger, R.; Guntherodt, H.-J., Eds. *Scanning Tunneling Microscopy III*; Springer-Verlag: Berlin, 1993.

(5) Sonnenfeld, R.; Hansma, P. K. *Science* **1986**, *232*, 211-213.

(6) Lu, X. H.; Grobis, M.; Khoo, K. H.; Louie, S. G.; Crommie, M. F. *Physical Review Letters* **2003**, *90*, art. no.-096802.

(7) Brask, J.; Wackerbarth, H.; Jensen, K. J.; Zhang, J. D.; Chorkendorff, I.; Ulstrup, J. *Journal of the American Chemical Society* **2003**, *125*, 94-104.

(8) Oppenheim, I. C.; Trevor, D. J.; Chidsey, C. E. D.; Trevor, P. L.; Sieradzki, K. *Science* **1991**, *254*, 687-689.

(9) McIntyre, B. J.; Salmeron, M.; Somorjai, G. A. *Rev. Sci. Instrum.* **1993**, *64*, 687-691.

(10) Rasmussen, P. B.; Hendriksen, B. L. M.; Zeijlemaker, H.; Ficke, H. G.; Frenken, J. W. M. *Review of Scientific Instruments* **1998**, *69*, 3879-3884.

(11) Jensen, J. A.; Rider, K. B.; Chen, Y.; Salmeron, M.; Somorjai, G. A. *Journal of Vacuum Science & Technology B* **1999**, *17*, 1080-1084.

(12) Weeks, B. L.; Durkan, C.; Kuramochi, H.; Welland, M. E.; Rayment, T. *Review of Scientific Instruments* **2000**, *71*, 3777-3781.

(13) Laegsgaard, E.; Osterlund, L.; Thostrup, P.; Rasmussen, P. B.; Stensgaard, I.; Besenbacher, F. *Review of Scientific Instruments* **2001**, *72*, 3537-3542.

Chapter 3: Experimental Apparatus

The work described in this dissertation was performed using a high-pressure, high-temperature scanning tunneling microscope (HPHTSTM), shown in Figure 3.1. This system combines an ultrahigh vacuum (UHV) chamber for sample preparation and characterization with an STM chamber where the pressure can be changed from UHV conditions to over 1 atm. Tips and samples can be exchanged through a load-lock that prevents the two chambers from being exposed to air, and a magnetically-coupled transfer arm moves the sample from one chamber to the other. The entire chamber rests on four air legs to dampen floor vibrations (Newport Laminar Flow Isolators, I-2000 Series). This chapter describes the instruments used in the UHV chamber and the STM design and capabilities.

3.1 UHV Chamber

The UHV chamber is a Varian surface analysis chamber equipped with a cylindrical mirror analyzer (CMA) for Auger electron spectroscopy, mass spectrometer, ion sputtering gun, and electron beam heater. It is pumped by a 200 L/s ion pump and a titanium sublimation pump to provide a base pressure below 5×10^{-10} Torr.

3.1.1 Sample Preparation

Before performing surface science experiments, the sample is cleaned and characterized to ensure that the metal crystal is free of contaminants. First the sample is sputtered with argon or oxygen ions to remove contaminants on the metal surface. These ions are created using an electron beam with energy of 400 eV and intensity of 20 mA.

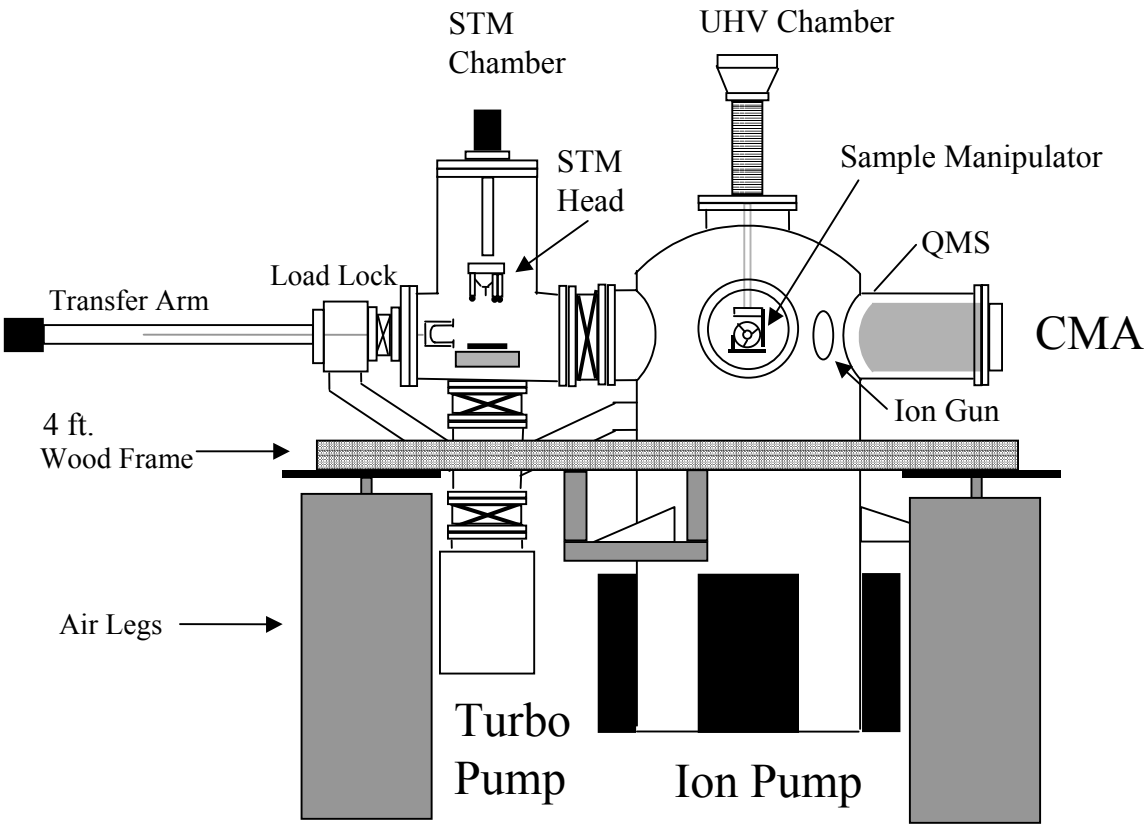

Figure 3.1 Diagram of HPHTSTM apparatus. Adapted from [1].

The gas pressure during sputtering is kept between 0.5-5 × 10^{-5} Torr for 10-20 minutes. The crystal is then heated in vacuum by electron bombardment to 700-860º C for 1-2 minutes to anneal out defects caused by sputtering so the crystal forms an atomically smooth surface again. Occasionally heating in oxygen is used to further clean the sample if carbon contamination is shown to be a large problem.

3.1.2 Auger Electron Spectroscopy

Sample cleanliness is checked using Auger electron spectroscopy (AES). In AES, a the metal surface is bombarded with high-energy electrons, and some of the surface atoms are ionized by having a core electron ejected, as shown in Figure 3.2. To reduce the significant potential energy of this ionized state, an electron from a shallower level relaxes into the vacant hole, and energy is released by the ejection of another shallow electron, the Auger electron [2]. The kinetic energy of the Auger electron can be calculated by

$$KE = E_A - E_B - E_C.$$

This kinetic energy usually ranges from 10-1000 eV, and thus these electrons have short mean-free-paths in a solid (less than 10 Å). This is what gives rise to the surface specificity of AES, as while many atoms may be ionized by a 1-3 keV electron beam, their Auger electrons will not leave the sample unless they are very close to the surface.

In this work, an electron gun bombards the surface with energies near 3 keV. The ejected Auger electrons are collected using a cylindrical mirror analyzer (CMA), shown in Figure 3.3. Unlike a retarding field analyzer (RFA), which acts as a high pass filter, a

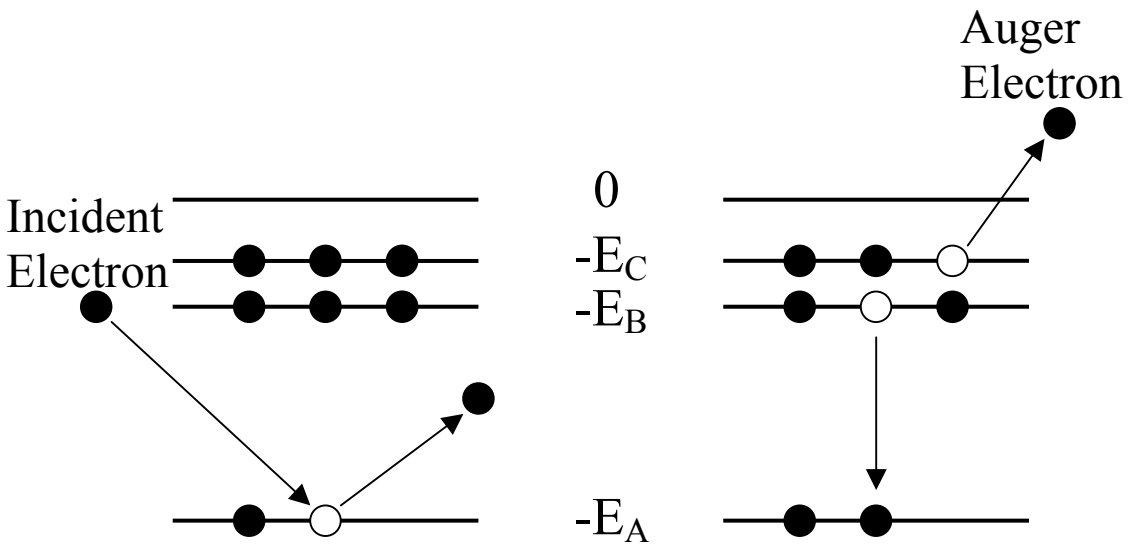

Figure 3.2 Energy level diagram showing the Auger electron process. The levels are labeled with their one-electron binding energies.

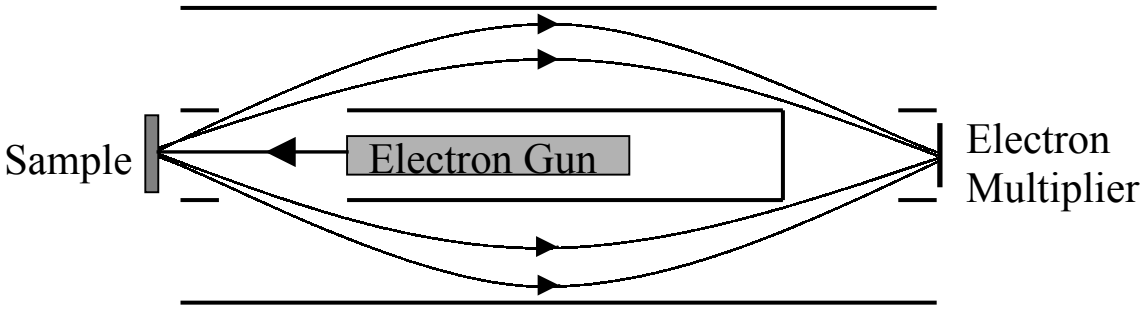

Figure 3.3 Schematic of cylindrical field analyzer (CMA) used for AES. The inner and outer cylinders are electrodes used to deflect the paths of electrons. Only those electrons within a small energy range will reach the electron multiplier.

CMA acts as a band pass in order to measure the number of electrons within a certain energy range. It uses cylindrical electrodes and has better signal-to-noise than an RFA.

While the raw data collected from AES is of the form number of electrons vs. electron energy, N(E) vs. E, Auger spectra are normally plotted as dN(E)/dE. Taking the derivative eliminates the secondary electron background and makes otherwise small peaks easier to see. In this work, AES is used to qualitatively check the cleanliness of the surface before performing STM experiments. Our detection limit for carbon, the most common contaminant, is about four percent of a monolayer. An Auger spectrum of Rh(111) is shown in Figure 3.4. The three distinguishing features of rhodium can be seen with valleys near 222, 256, and 302 eV. A small shoulder near 272 eV may indicate small amounts of carbon, while oxygen is not present as it would appear at 510 eV.

3.1.3 Mass Spectrometry

The UHV chamber is equipped with an SRS mass spectrometer (MS) used for residual gas analysis. A mass spectrum of the residual gas background of the UHV chamber is shown in Figure 3.5. The background consists mostly of hydrogen at mass 2, CO at 28, water at 18, and CO_2 at 40. In addition to analyzing the background pressure of the UHV when checking for chamber leaks, the apparatus has been designed so that analyzing gases from the STM chamber is also possible. Since the working pressure of the MS is below 1×10^{-4} Torr, having the MS directly mounted on the high-pressure STM chamber is not practical. Instead, a feedthrough about 4 ft. long leads from the STM chamber to a leak valve mounted below the MS. Inside the UHV chamber, a 1/8" stainless steel tube leads from the leak valve to a tantalum shroud covering the ionizer of

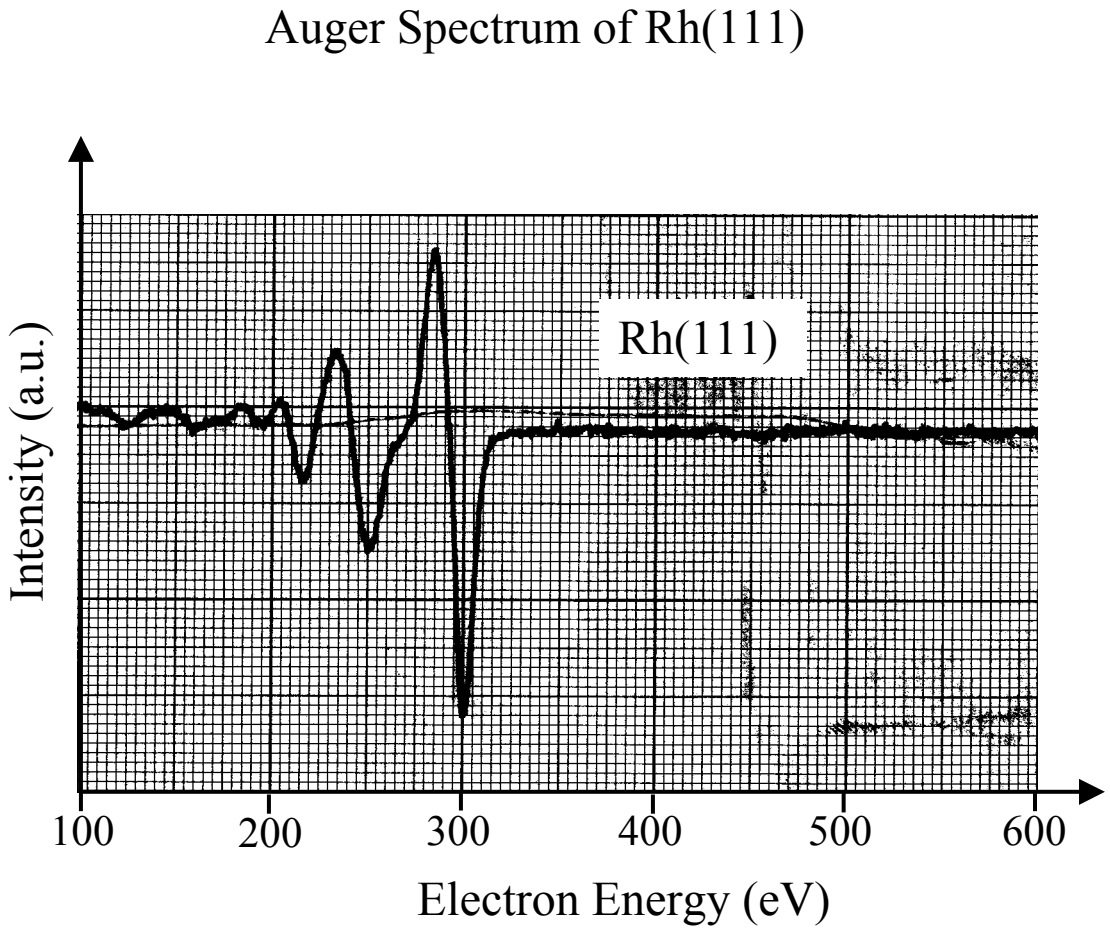

Figure 3.4 Auger spectrum of Rh(111).

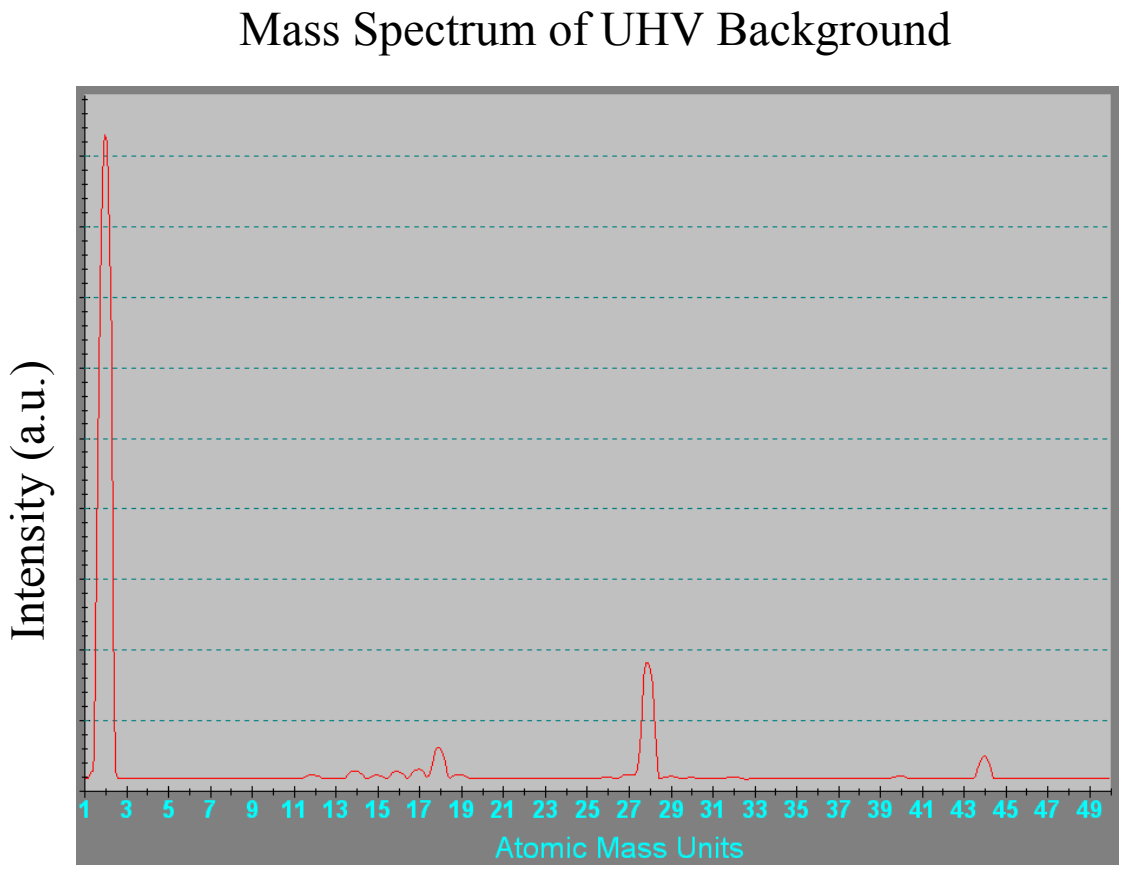

Figure 3.5 Composition of residual gas in UHV chamber.

the MS. This enables a controlled leak of high-pressure gas from the STM chamber to be introduced to the MS.

3.1.4 Manipulator

The UHV manipulator is based on a commercial XYZθ manipulator and is shown in Figure 3.6. It holds the sample on a stainless steel fork so that the thermocouple leads of the sample holder align with those on the manipulator. Behind the sample holder is a thoriated tungsten filament for electron beam heating. The filament is mounted in a ceramic tube on a carriage that can be moved using a rack-and-pinion gear to within 1 mm of the sample, thus reducing heating of the surrounding holder and manipulator. The front of the carriage, which touches the sample holder, is made of copper and is attached to a copper braid that connects to a liquid nitrogen cooling system. This cooling system decreases the cooling time after annealing, reducing contamination of the sample.

3.2 Transfer System and Sample Holder

The transfer system consists of a 36” long, magnetically coupled rotating fork that fits into grooves on a specially designed sample holder. This transfer arm moves the sample from the UHV chamber to the STM chamber and vice versa. This holder, based on a commercial RHK holder, is shown in Figure 3-7. The top piece of the holder has the molybdenum ramps used for the coarse approach, which is described later. The sample is attached to a thin, tantalum disc by spot-welding tantalum strips over opposite ends of the sample, which is a disc with a diameter of 0.5-1 cm. The tantalum disc is attached to the rest of the holder by three leaf springs that will not loosen with thermal expansion. A

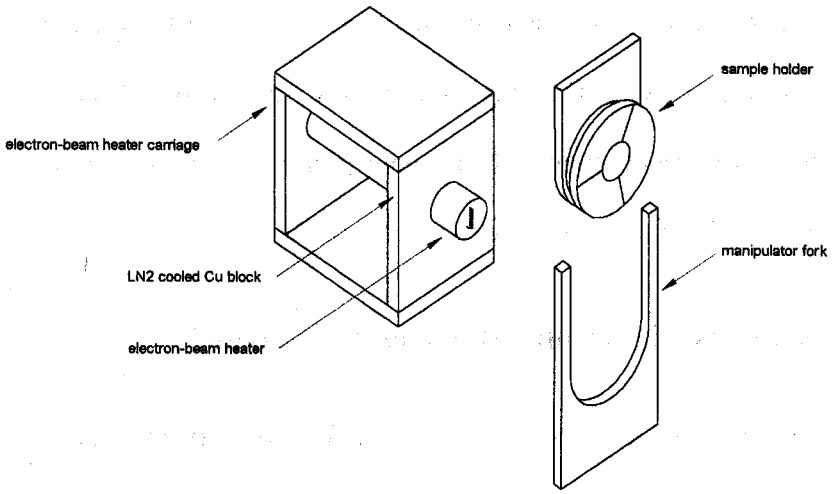

Figure 3.6 Diagram of UHV manipulator. The fork holds the sample holder so that thermocouple leads on the holder and manipulator align. A rack-and-pinion gear (not shown) moves the electron-beam heater within 1 mm of the sample. The front of the carriage is cooled via a cooper braid (not shown). From [1].

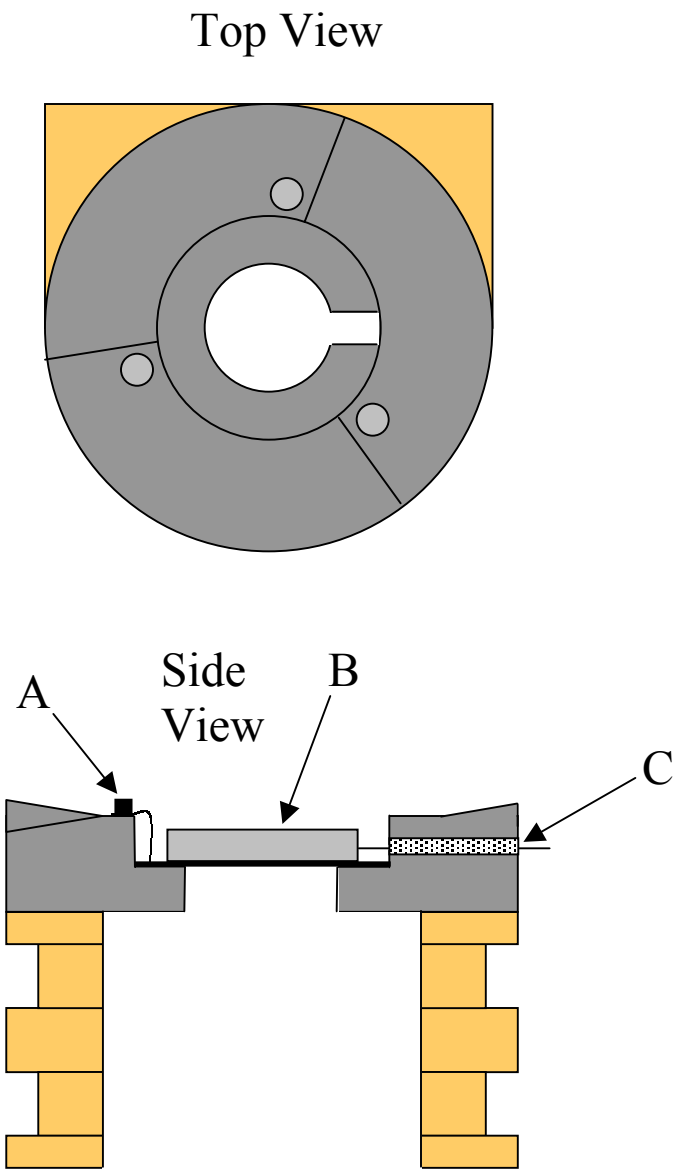

Figure 3.7 Sample holder: Top view (top) shows three ramps and screw holes for holding spring clips. Cut-away side view (bottom) shows hollow area for lamp to fit in and A: spring clip held down by screw, which holds in place B: sample mounted on 0.010" tantalum disc. C: thermocouple fed through insulating ceramic aligns with matching thermocouples on UHV manipulator and STM stage.

type K (chromel-alumel) thermocouple that touches the sample is isolated by a ceramic tube and extends about 4 mm away from the sample holder. These wires are positioned so they align with matching wires on both the STM stage and UHV manipulator. The bottom of the holder is a hollow piece of stainless steel coated with gold. It is designed so that a heating lamp can be placed about 1 mm from the sample. There are two grooves that allow the sample to be transferred throughout the apparatus using forks.

3.3 STM Chamber

The STM Chamber consists of a 10 L chamber with the STM stage mounted on an 8" flange at the back and the STM manipulator mounted on a 6" flange on top. The chamber is pumped by an ion pump and a 260 L/s turbomolecular pump (Balzers-Pfeiffer TMU 260).

3.3.1 Scan Head

The STM used in this work is an inverted-Besocke or Beetle-style STM that is commercially available (RHK VT-UHV300). Besocke invented an STM head in 1986 [3] that used three outer piezoelectric tubes for the coarse movement and a fourth, central tube for scanning. The sample rested on top of the three outer tubes. These tubes were smaller than piezo arrangements typically used at the time that were stacks of three piezos oriented in three orthogonal directions to give movement in the x, y, and z-directions. The reduced size of the piezos and STM meant that the STM had better vibrational characteristics.

Our STM is similar, though the sample is below the STM head and none of the piezos directly touch the sample. Each tube is made of lead zirconate titanate (PZT) and is coated on the inside and outside with zinc to make electrodes. The outer electrode is divided lengthwise into four sections. Once polarized, the piezos work reproducibly below 365 ºC, the Curie temperature of PZT. Movement in the z direction is obtained by applying a voltage between the inner electrode and the four outer ones. This causes a change in tube length of $\frac{\Delta L}{L} = d_{31}\frac{V}{w}$, where w is the wall thickness, V is the voltage, and d_{31} is the piezoelectric coefficient, which is 1.71 Å/V for PZT. Movement in the x or y direction is achieved by applying a positive bias between one outer electrode and the inner one and a negative bias between the opposite outer electrode and the inner one. The lateral displacement is given by $\Delta x = 2\sqrt{2}\cdot d_{31}\frac{L^2 V}{\pi D w}$, where D is the inner diameter of the tube. Vector addition of voltages in the x and y directions enable the piezo to move freely in two dimensions.

The coarse approach of the tip to the sample is done using the three outer piezos. These have sapphire balls attached to the end that rest on the three helical ramps of the sample holder, as shown in Figure 3.8. These ramps are 1 mm high, and the tip is placed in the head so it is about 0.5 mm from the sample when the legs are at the top of each ramp. The course approach consists of the head walking down the ramps until the tip, mounted on the central piezo, is within tunneling range. The walking is accomplished by slowly tilting each leg down the ramp and then quickly bringing them back to their equilibrium position. During the fast motion the balls slide along the ramps and the head ends up slightly down the ramp from where it started. After each step, the tip is extended

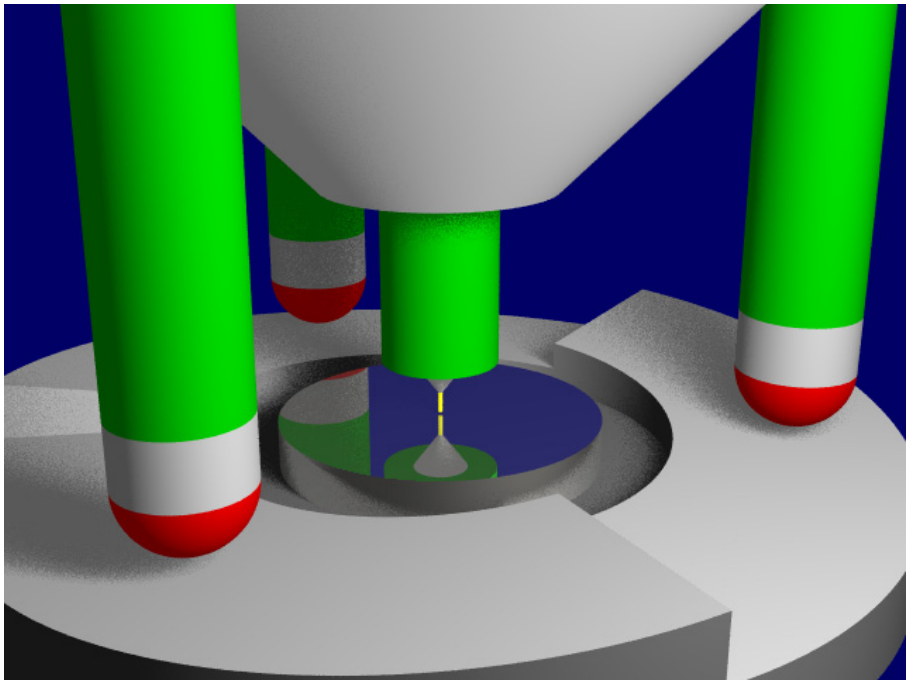

Figure 3.8 Model of STM scan head. The three outer piezos support the head and rest on three helical ramps. The central scan piezo holds the tip. The sample is 1 cm in diameter. From [1].

and tunneling current is looked for. If there is none, then the process is repeated until the tip enters tunneling range. Once the tip is within tunneling range, the central scan piezo is used to position the tip. It has a 5 μm range in the lateral directions.

3.3.2 STM Stage

The STM stage holds the sample during experiments and also contains the heating element. The stage rests on Viton spacers to decouple the working STM from the rest of the chamber. These spacers dampen high-frequency vibrations while still being rigid enough to hold the stage in place for sample and tip exchange.

Heating in high pressures ($> 1 \times 10^{-4}$ Torr) is not possible with an electron beam heater due to the short mean-free-path of the electrons. For STM experiments we use a modified light bulb that would normally be used for an overhead projector (82 V, 250 W). The modification process is shown in Figure 3.9. First the reflective shielding surrounding the actual bulb must be cut away. Then the epoxy surrounding the two electrical leads and bulb base must be removed. After this, the edges of the base of the bulb must be ground down until the bulb fits snugly in the opening on the sample stage. Finally, any remaining epoxy is sandblasted away. The modified bulb can be positioned about 1 mm from the sample to provide radiative heating without a mechanical contact. A variable autotransformer is used to control the power supplied to the bulb and thus the temperature. In 1 atm of gas the sample can easily be heated above 900 K.

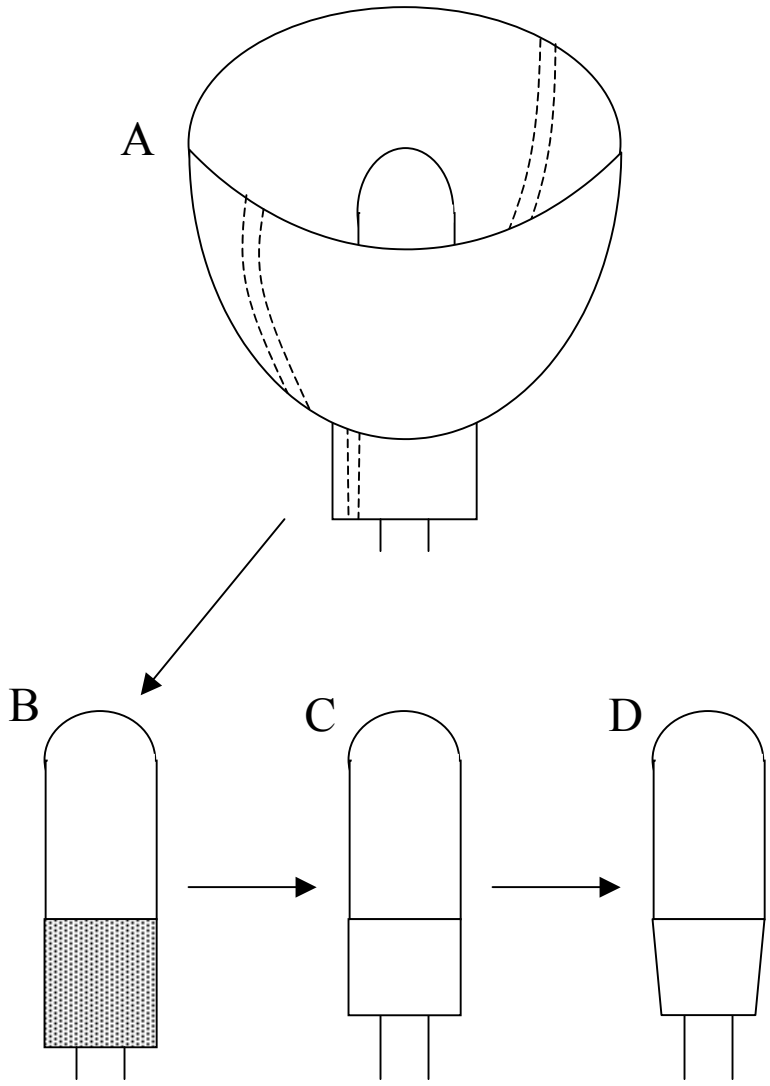

Figure 3.9 Lamp preparation for STM heating. First the reflective shielding is cut away by making to opposing cuts (A). This leaves a bulb with epoxy covering much of the base (B). After grinding away the epoxy, the metal leads are fully exposed (C). The glass base then needs to be tapered so the bulb will fit inside the STM (D).

3.3.3 Tips

The tip is often the limiting factor in achieving high-quality STM images and hence the productivity of the apparatus. This is especially true when doing experiments under high-pressure and high-temperature conditions. New tip materials and preparations are constantly being tried in an effort to make better tips.

The work in this dissertation was done using tungsten tips. Tungsten tips provide stable imaging under high pressures of CO, NO, hydrogen, and hydrocarbons. However, they are unstable in the presence of oxygen as they form a surface layer of insulating tungsten oxide. Tungsten is also very hard and less susceptible to blunting than metals such as gold.

Our tips are made by electrochemical etching, which is shown in Figure 3.10. A 0.010" tungsten wire is suspended through a loop of Pt wire. This loop holds a film of 2 M KOH. Initially a 1.5 V bias is used until the diameter of the wire has decreased significantly. As gravity pulls on the wire blow the film, a taper begins to form. Waiting until the wire falls off leads to a tip with a long taper which will vibrate more than one with a short taper [4]. In order to achieve a short taper, the wire is flipped over after the initial etching so the section with the long taper is above the electrolyte film and the short taper section will become the tip. The voltage is also decreased to 0.3 V at this stage. When the wire has etched all the way through, the part below the wire loop is caught and used as a tip.

Various combinations of tungsten and carbon were tried, but none worked any better than pure tungsten. Ion implantation and heating in acetylene were attempted to make tungsten carbide tips. Carbon nanotube tips were also tried using an attachment

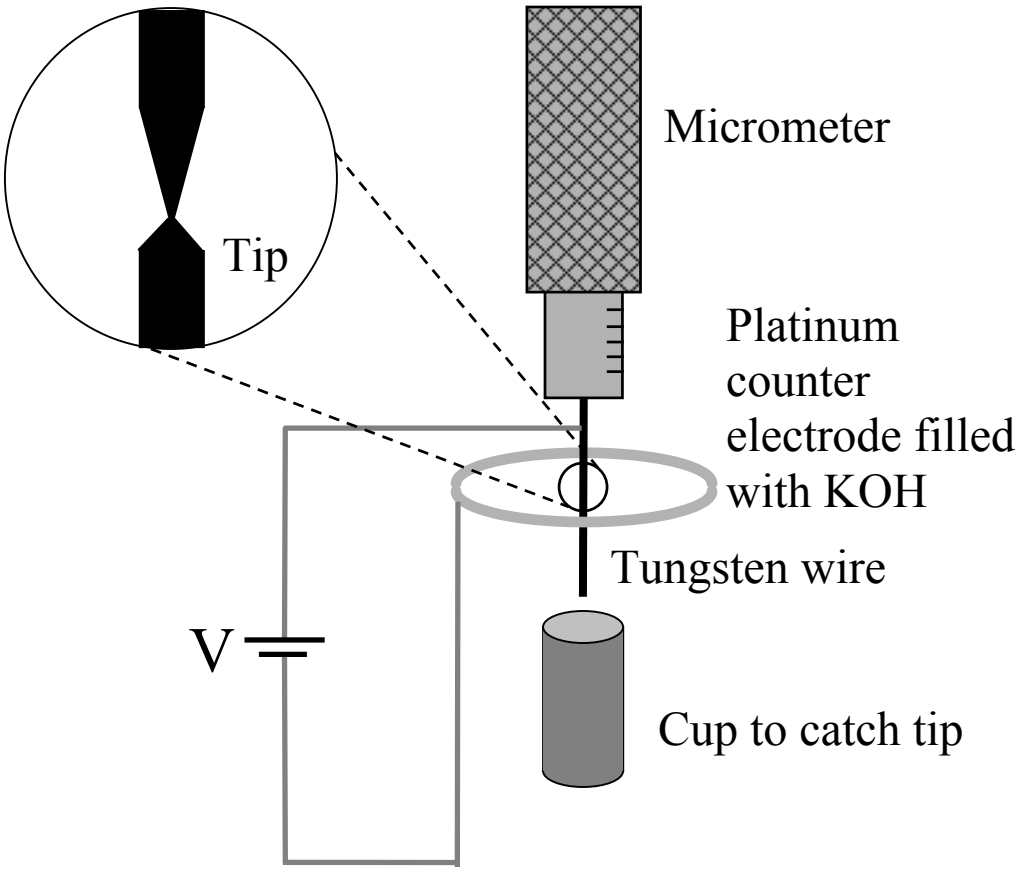

Figure 3.10 Tip-making apparatus. The inset shows the wire after it has been flipped to ensure that the tip will have a short taper.

method shown to work for atomic force microscope tips [5], but they never showed molecular resolution when used for STM.

3.3.4 Tip Exchange

When working with high-pressure, high-temperature experiments, tip lifetimes are short due to the gas molecules interacting with the tip. In many STMs, tip exchange requires removing the entire STM from the vacuum chamber in order to perform the delicate tip exchange manually in air. This would be extremely inconvenient for an STM that is usually operated under high pressures of gas, as the entire chamber must then be baked out in order to remove adsorbed water and other contaminants from the walls. Our STM avoids this problem by using a small load lock to transfer a specially made tip exchanger from vacuum to air. Venting only this small volume during tip exchange means that UHV conditions can be restored overnight, without baking.

The tip exchanger, shown in Figure 3.11, is designed to require minimal manual input so that only wobble stick equipped with a fork is necessary to perform the exchange. The exchanger has three posts identical in height to the outer legs of the STM head. When the sample holder is replaced with the tip exchanger, the head can be lowered onto the exchanger. Holes in the head are aligned opposite the posts on the exchanger, and holes on the exchanger are aligned opposite the legs of the head. These six contacts ensure that the tip holder, which is being held on the central scan piezo by friction, will align with a hole on the center of the exchanger. When the head is lowered all the way down, a wire on the exchanger can be bent around the tip holder and secured behind a set screw. In doing this, the wire will fit into a groove on the tip holder and pin

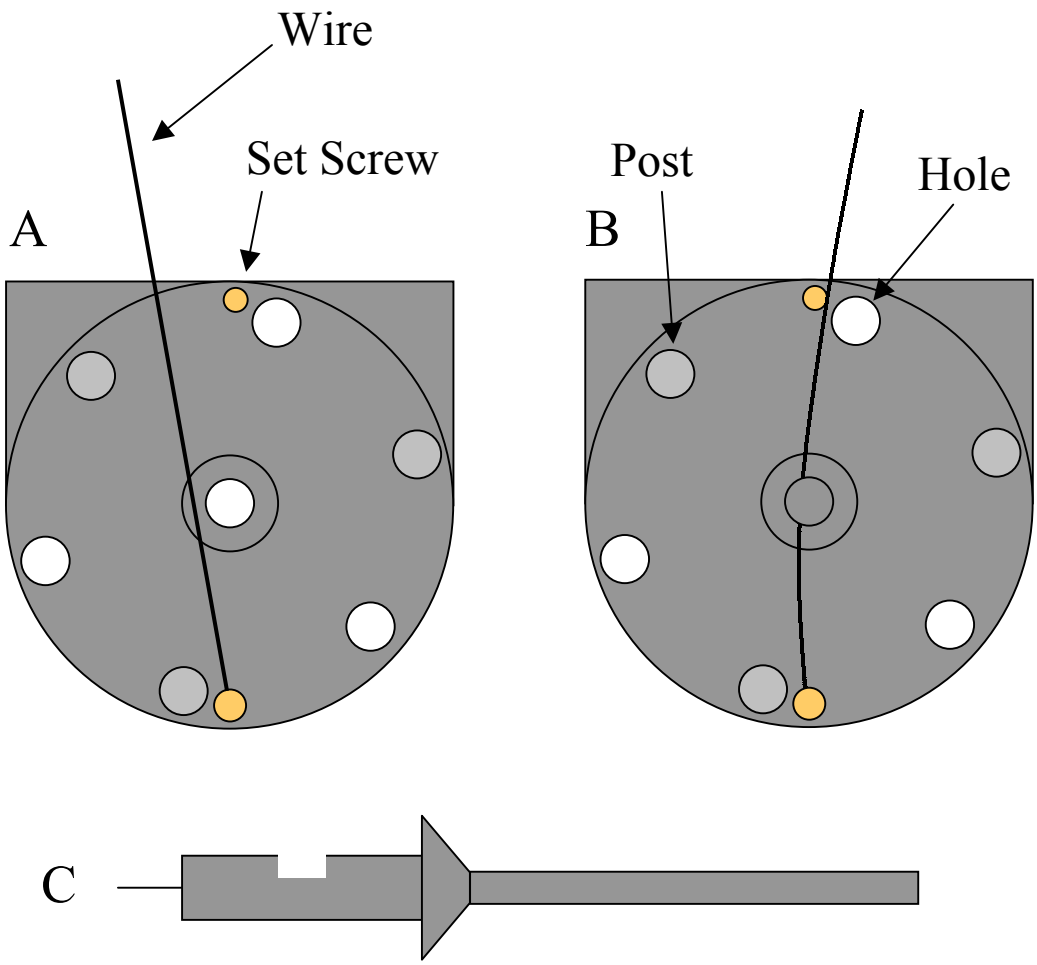

Figure 3.11 Tip exchanger (A & B) and tip holder (C). In position A, the tip holder is free to form a friction fit with the STM. In position B, the wire is caught in the groove on the tip holder, keeping the tip holder on the tip exchanger.

it onto the exchanger. When the head is lifted, the tip holder will remain on the tip exchanger, which can then be transferred out of the apparatus via the load-lock.

References

(1) Rider, K. B. *Ph.D. Thesis, University of California* **2001**.

(2) Woodruff, D. P.; Delchar, T. A. *Modern Techniques of Surface Science*; 2nd ed.; Cambridge University Press: Cambridge, 1994.

(3) Besocke, K. *Surf. Sci.* **1987**, *181*, 145-153.

(4) Klein, M.; Schwitzgebel, G. *Rev. Sci. Instrum.* **1997**, *68*, 3099-3103.

(5) Stevens, R. M. D.; Frederick, N. A.; Smith, B. L.; Morse, D. E.; Stucky, G. D.; Hansma, P. K. *Nanotechnology* **2000**, *11*, 1-5.

Chapter 4: NO on Rh(111)

This chapter describes how high-pressure, high-temperature scanning tunneling microscopy (HPHTSTM) was used to study nitric oxide structures on Rh(111). We discovered that NO formed a new structure in equilibrium with the gas phase near room temperature and at pressures in the Torr range. Two dense phases form with (2×2) and (3×3) periodicity. Regions of the surface transform from one phase to the other as the pressure and temperature change around the equilibrium *P-T* boundary line. By measuring the pressures and temperatures of coexistence, we determined the heat of adsorption of the previously unknown (3×3) structure. From the dynamics of the phase boundary line, the activation energy barrier between the two phases could be estimated. The results demonstrate that unique information can be obtained from high-pressure and high-temperature studies, expanding our understanding of gas-surface interfaces on the atomic scale.

4.1 Introduction

Our understanding of the elementary steps of gas-surface reactions comes primarily from experiments performed under low-pressure (10^{-4} - 10^{-10} Torr) conditions. The motivation for studying many gas-surface reactions is the industrial importance of selective adsorption and heterogeneous catalysis. The difference between traditional low-pressure surface science studies and industrial applications, which are normally carried out at high pressure, is known as the pressure-gap. In addition, the sample temperature during a low-pressure experiment must be very low if the coverage is to remain the same as that obtained at high pressures. This means that in the divide between

traditional surface science and its industrial motivation, there is not only a pressure-gap, but also a concomitant temperature-gap. Bridging these gaps is critical for a fundamental understanding of catalytic phenomena. Although the high surface coverage that prevails in industrial operations at high pressure can be achieved at low pressure by lowering the temperature, the structures formed under the two conditions might not be the same, as we have shown recently in the case of Pt(111) in 200 Torr of CO [1]. At high pressure and temperature, dense structures are formed in equilibrium with the gas phase, while at low temperature, the structures must be kinetically frozen and not in equilibrium. In addition, the low temperature is likely to prevent the formation of structures that are reached through an activated process such as surface reconstruction. In our laboratory, these problems have been overcome through the development of a high-pressure, high-temperature scanning tunneling microscope in our laboratory.

Here, we report the discovery of new structures of NO on Rh(111) formed at pressures in the Torr range and their transformation dynamics. Two ordered structures are found with (2 × 2) and (3 × 3) periodicity relative to the rhodium substrate, which are only slightly different in density, as we shall see. Regions of the surface transform from one structure to the other with small changes of temperature and pressure around a phase equilibrium line. The heat of adsorption of molecules in the (3 × 3) structure was determined using the two-dimensional analog of the Clausius-Clapeyron equation.

Several ordered structures of NO on Rh(111) are known. A LEED and HREELS study [2] found that NO binds in hollow sites at 95 K without lateral order. Adsorption of small amounts of NO at higher temperatures causes dissociation into N and O adatoms [3]. At 120 K, 0.5 ML (monolayers) of NO forms a c(4 × 2) structure with all of the

molecules on the same adsorption site, most likely a three-fold hollow site [4,5]. At 250 K, 0.75 ML of NO forms at a (2 × 2)-3NO structure with two molecules in hollow sites and one on a top site. The known adsorption structures of NO on Rh(111) are summarized in Table 4.1.

A (2 × 2) structure with coverage of 0.75 ML is known to form either by large (~20 Langmuir) exposures to NO at 200 K, or by small (~2 Langmuir) exposures at 40 K, followed by annealing to 200 K. At room temperature, it is possible to maintain this structure with a constant background of 10^{-8} Torr. X-ray photoelectron diffraction [4] and automated tensor LEED [6] studies indicate that the unit cell of this structure contains three NO molecules, one on a top site and two in three-fold hollow sites. The on-top NO molecule sits 0.4 Å higher than the hollow site molecules.

4.2 Experimental

The STM was housed in a reactor chamber, which was connected to a standard ultra-high vacuum surface science apparatus where the samples were prepared and characterized. After transferring the sample to the reactor chamber, gate valves were closed to isolate the chamber and gases at high pressure were introduced. The capabilities of the instrument are described in detail elsewhere [7,8].

The sample was cleaned by Ar^+ sputtering and by annealing in O_2. Auger spectroscopy revealed that carbon, which is the most common contaminant, made up less than 5% of the surface. After cleaning, the sample was moved to the high-pressure chamber and imaged by STM using etched tungsten tips.

Surface Structure	**Coverage**	**Adsorption Site(s)**	**Reference**
(3 × 3) electrochemical	0.44	Top, Bridge	[9]
c(4 × 2)	0.5	Hollow	[10]
(2 × 2)	0.75	Top, Hollow	[10,11]
(3 × 3) high pressure	0.77	Top, Hollow	[11]

Table 4.1 The known adsorption energies of NO on Rh(111).

4.3 Results and Discussion

In the range of 10^{-8} to 0.01 Torr of NO at room temperature, the images show the same (2 × 2) periodicity, with only one maximum per unit cell. The structure is similar to the one formed by CO on Rh(111) and Pd(111). STM studies of these two structures also show one maximum per unit cell [12]. According to theoretical calculations, that maximum corresponds to the CO molecule in the top site [13]. It is likely that the same is true for the (2 × 2)-3NO structure.

When the NO pressure in the STM chamber is increased at approximately 0.001 Torr/minute, the adsorbed layer of NO molecules remains in equilibrium with the gas phase. As the pressure entered the range between 0.01 and 0.05 Torr, areas of the surface were seen that were covered with a (3 × 3) pattern. These areas grow over the course of a few hours until the entire surface is covered by the (3 × 3) structure. Figure 4.1 shows a series of 100 Å × 100 Å images taken 55 seconds apart on the same area of the surface in 0.03 Torr of NO. In image 1a, the majority of the surface is covered with the (2 × 2) pattern with one corner showing a small area of the (3 × 3) pattern. The boundary line (shown in white) propagates at a rate of about 20 Å/minute from the upper-right corner to the lower-left. In images 1a and 1b, a defect has been marked as a reference.

In Figure 4.2, we show an island of (3 × 3) structure (inside the dotted line) surrounded by areas with the (2 × 2) structure. Two straight lines have been drawn that separate two unit cells of the (3 × 3) structure or three unit cells of the (2 × 2) structure. The cursor profile along line A-B (shown at the bottom) reveals two interesting differences between these NO structures: (1) The corrugation of the (3 × 3) structure is always higher, and (2) the apparent height is also higher in the (3 × 3) regions. In the

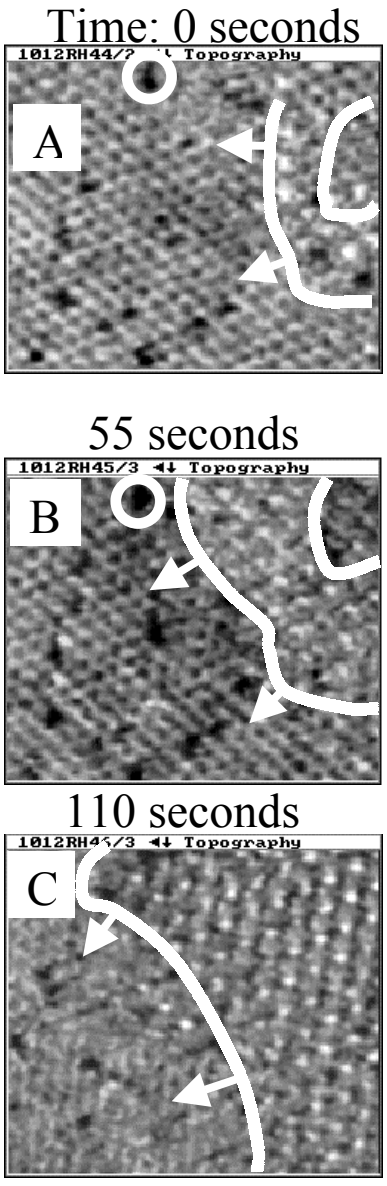

Figure 4.1 STM images of Rh(111) taken in 0.03 Torr of NO at 25ºC, showing the phase transition between a (2 × 2) and a (3 × 3) structure. The 100 Å × 100 Å images were taken at 55 seconds intervals (I = 440 pA, V = 99 mV). In image a, the majority of the surface shows the (2 × 2) structure, except for the upper right-hand corner which shows the (3 × 3) structure. In images b and c, the domain boundary between the two phases moves across the image at a rate of ~20 Å /minute. Images a and b share a common defect, marked with a circle. The close packed rows of both patterns are aligned, and the maxima separated by multiples of the Rh-Rh distance. This indicates that the bright spots correspond to NO molecules on similar sites in both the (2 × 2) and the (3 × 3) structure.

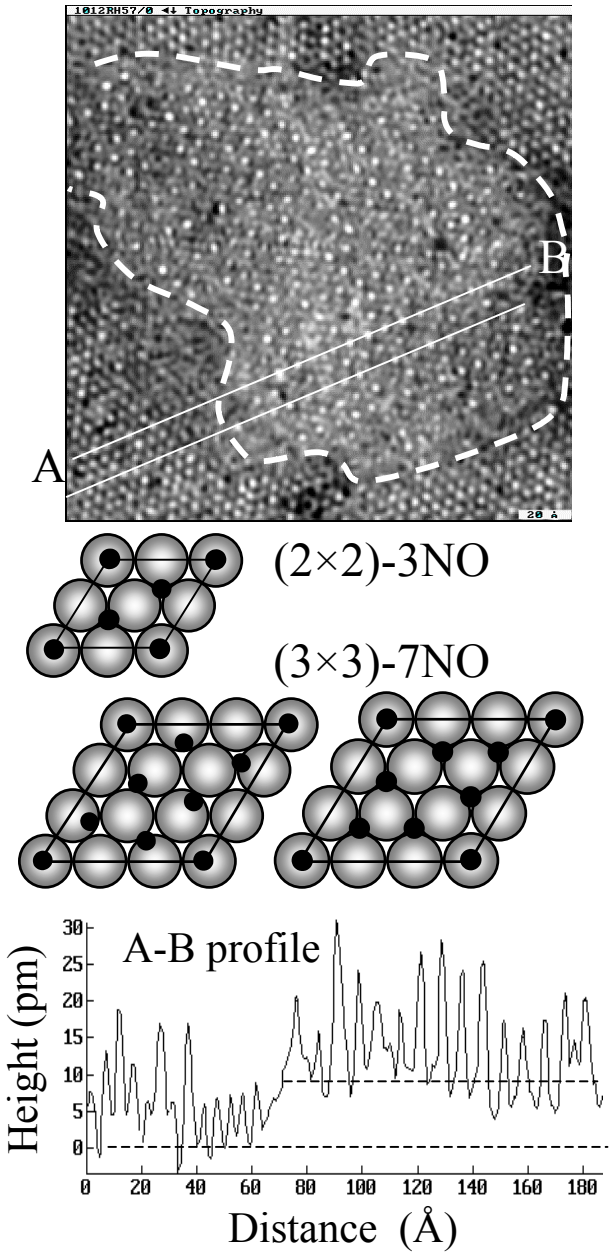

Figure 4.2 A 200 Å × 200 Å STM image taken in 0.03 Torr NO at 25ºC, showing a (3 × 3) domain surrounded by the (2 × 2) structure. It is known that the (2 × 2)-3NO structure contains one top-site NO molecule and two molecules on hollow-sites. Two similar models are proposed for the (3 × 3) structure. The first (left) consists of one top-site NO molecule and 6 molecules near hollow-sites. In the second model (right), the near hollow-site molecules are allowed to relax so that they can occupy 3-fold hollow-sites. Both models have a 0.778 ML coverage and are consistent with the STM images. A line profile taken from line A-B on the image is shown. Note the higher corrugation in the (3 × 3) domain and its higher apparent height, ~0.1 Å above that of the (2 × 2) domain.

present image the corrugation in the (3 × 3) region is 0.2 Å on average, compared with the 0.1 Å corrugation of the (2 × 2) region. These values vary by a factor of two from image to image, as a result of different tunneling conditions and tip structures. On average, the (3 × 3) to (2 × 2) corrugation ratio is 4 to 1. Also in the same figure, the apparent height of the regions covered by the (3 × 3) structure is ~0.1 Å higher than that of the regions covered by the (2 × 2) structure. In general, this apparent height difference varies between 0.1 and 0.5 Å, again depending on tunneling conditions and tip structure. While the higher corrugation of the (3 × 3) structure could be the result of the larger dimensions of the unit cell, which causes the top-site NO molecules to be farther apart and allows the tip to better follow the molecular contours, results from Chapter 5 argue against this. More likely, it is the result of a restructuring of the rhodium substrate. The higher elevation of the base line in the denser structure might indicate an expansion of the top layer of rhodium atoms. The answer to these interesting questions requires experiments with other techniques such as grazing angle X-ray diffraction.

While the (2 × 2) structure has been solved by LEED, no information is available concerning the (3 × 3) structure. The models shown in the middle of Figure 4.2 are proposed based on the following considerations. First, the coverage in the (3 × 3) structure must be only slightly higher than the coverage of the (2 × 2) structure (0.75 ML) because the (2 × 2) structure is already very dense (only 3.16 Å separates adjacent molecules). Second, the STM images show that the rows of maxima in both structures are parallel and are separated by multiples of the Rh-Rh distance. This indicates that the NO molecules producing the maxima occupy similar on-top sites in both structures. A (3 × 3) structure satisfying these two conditions and preserving the hexagonal packing of

NO found in the (2 × 2)-3NO can be obtained by a rigid rotation of the NO layer by 10.9º followed by a linear compression of 1.8%. A more symmetric structure with NO molecules in 3-fold hollow sites can be obtained by allowing a small relaxation of the NO molecules inside the cell. In both of these models the surface coverage is 0.778 ML, only 3.7% larger than the (2 × 2)-3NO coverage.

Another interesting observation is the facile displacement of the boundary between the two NO structures, which is indicative of a dynamic equilibrium between the gas and surface. Figure 4.3 illustrates this phenomenon more dramatically. A series of 500 Å × 500 Å images were taken at a constant pressure of 0.01 Torr. Although the large size of these images does not allow the individual cells to be visible, high-resolution images show that the bright areas are domains of the (3 × 3) structure and that the dark areas are domains of the (2 × 2) structure. In image a, several (3 × 3) domains can be seen, labeled 1, 2 and 3. Initially, domains 1 and 2 are part of a larger domain. In images b-e, this domain splits in half and domain 1 dissipates. In image f, domains 1 and 2 have dissipated, but domain 3 remains. In the next image (which is not shown), domain 3 has also dissipated, leaving a surface entirely covered by the (2 × 2) structure. The formation of the (3 × 3) domains does not appear to be affected by the presence of the tip, since similar phenomena are observed whether the gas is added with the tip far from the surface or within tunneling range. The facile displacement of the boundary between the two structures, which occurs in a time scale of seconds, indicates that they are energetically separated by a barrier of approximately 0.7 eV [14], which allows thermal fluctuations to convert small areas of the surface from one structure to the other. This

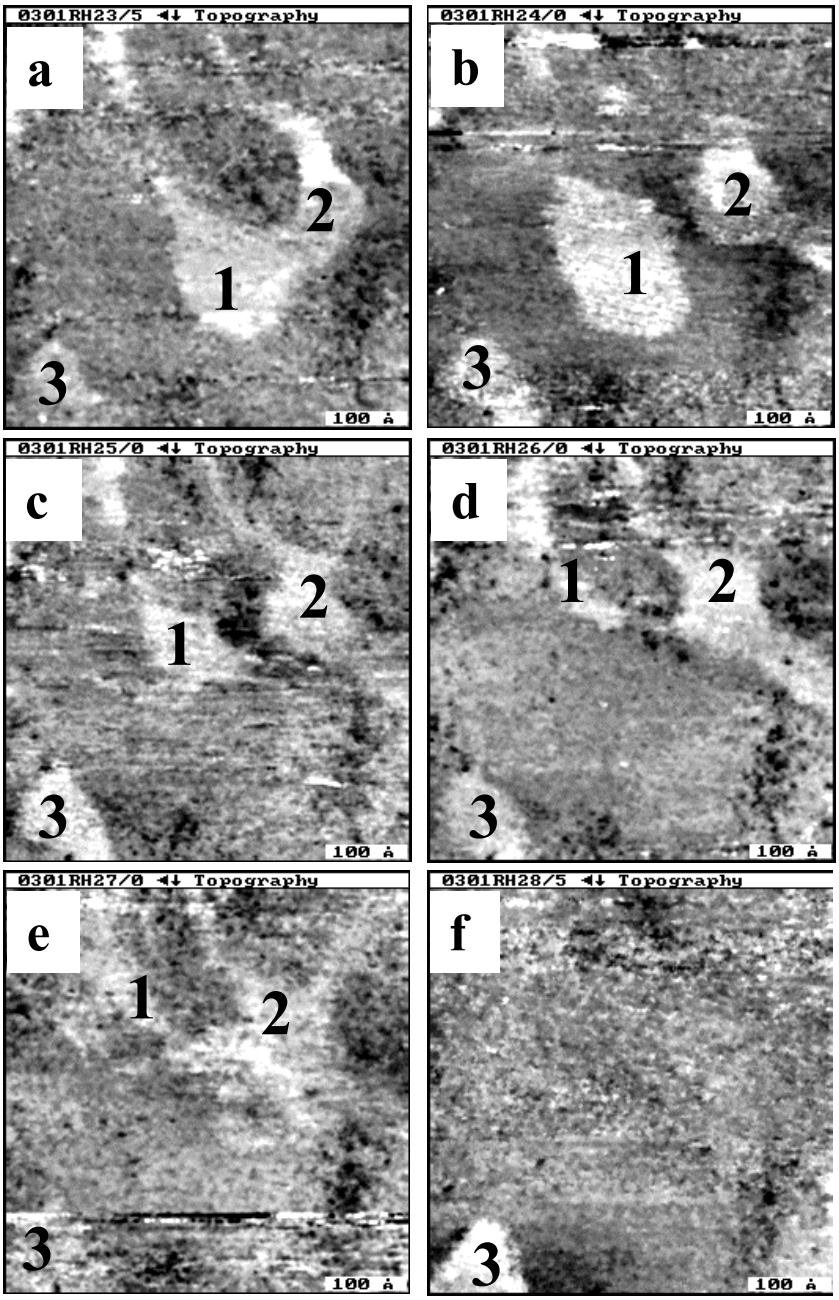

Figure 4.3 A sequence of 500 Å × 500 Å STM images taken in 0.01 Torr NO at 25ºC, showing the evolution of a domain of the (3 × 3) structure (I = 214 pA, V = 101 mV). The brighter area is the (3 × 3) structure and the darker background is the (2 × 2) structure. The images were taken 55 seconds apart. In image a, several (3 × 3) domains can be seen, labeled 1, 2 and 3. Initially 1 and 2 are part of a larger domain. In images b-e, this domain splits in half and domain 1 dissipates. In image f, 1 and 2 have dissipated, but 3 remains. In the next image, domain 3 has also dissipated, leaving a surface entirely covered by the (2 × 2) structure (not shown).

barrier, of course, is not the energy difference between the two structures, as we discuss next.

Until now, we have described experiments performed at room temperature. To study the phase equilibrium and the energy difference between the two structures, experiments were performed at temperatures between 300 K and 350 K. As expected, the phase transition pressure P increases as a function of temperature T. Figure 4 is a plot of $\ln(P)$ vs. $1/T$, where each point represents a pressure and temperature in which both (2 × 2) and (3 × 3) structures were observed on the surface. In the region close to the line, both structures are visible, even after long periods of time (more than 12 hours). In the region above the line, only the (3 × 3) structure is observed; below the line only the (2 × 2) structure is observed. The slope of the straight line is 1.1 ± 0.2 eV/k (k = Boltzman constant). The relation between this slope and the heats of adsorption is discussed below.

The state of the gas-surface system is described by three variables P, T and φ, where φ is the two-dimensional surface pressure. When the system consists of a gas phase and two surface phases (1 and 2, for the (2 × 2) and (3 × 3) phases, respectively), the equilibrium condition $\mu(P,T) = \mu_1(P,T,\varphi) = \mu_2(P,T,\varphi)$ places two constraints on P, T and φ, leaving one degree of freedom. It is this degree of freedom that is represented by the line in Figure 4.4. According to Hill [15], when a perfect gas is in equilibrium with two surface phases

$$\frac{d\ln P}{dT} = \frac{\Gamma_2(H_2 - H_g) - \Gamma_1(H_1 - H_g)}{kT^2(\Gamma_1 - \Gamma_2)},$$

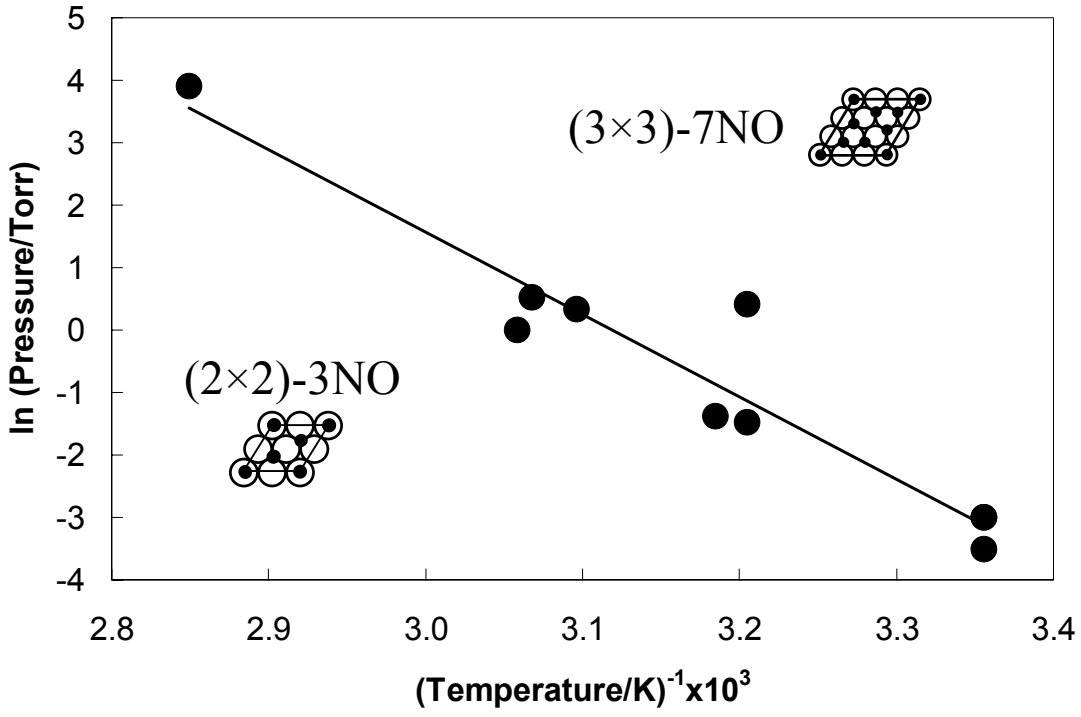

Figure 4.4 Plot of ln(P) vs. $1/T$ for values where the (2 × 2) to (3 × 3) transition takes place. The line through the experimental points (•) separates regions where the (2 × 2) structure is stable (below) and where the (3 × 3) structure is stable (above). The slope of this line is 1.1 ± 0.2 eV/k.

where H_i is the molar enthalpy of phase i and the Γ_i terms are the coverages for the surface phases. Recognizing that (H_1-H_g) and (H_2-H_g) are heats of adsorption, which we will call h_1 and h_2,

$$\frac{d\ln P}{d(1/T)} = \frac{\frac{\Gamma_1}{\Gamma_2}h_1 - h_2}{k\left(\Gamma_1/\Gamma_2 - 1\right)}.$$

The heat of adsorption for Rh(111) surfaces saturated with NO in low-pressure conditions has been measured to be 1.0 ± 0.1 eV [5]. Under these conditions the surface forms the (2 × 2)-3NO structure, so h_1 = 1.0 eV. From the slope in Figure 4.4 and given that Γ_2 = 0.778 and Γ_1 = 0.75, we calculate the heat of adsorption for the (3 × 3)-7NO structure to be 0.9 ± 0.1 eV. The difference in the heat of adsorption for the two structures is therefore of order 0.1 eV, a result anticipated from the observation that the two phases can occupy similar areas of the surface.

4.4 Summary

The novel observation of molecularly resolved surface phenomena at high pressure and temperature heralds the beginning of a new era in surface science. By bridging the pressure and temperature gaps with high-pressure, high-temperature STM, we have the opportunity to study molecular level structures and processes at gas-surface interfaces under conditions that were previously inaccessible. We have shown the transition from the (2 × 2)-3NO structure, which is known from low-pressure surface science experiments, to a new (3 × 3) structure, which only forms in equilibrium with the gas phase at high pressure. By directly observing the transition between these structures at several temperatures and pressures, we could measure the heat of adsorption in the new

structure to be 0.9 ± 0.1 eV, and from the dynamic behavior of the phase boundary, we deduced an energy barrier of approximately 0.7 eV. It is clear that these are the types of studies that are most relevant to a molecular level understanding of surface catalyzed reactions.

References

(1) Jensen, J. A.; Rider, K. B.; Salmeron, M.; Somorjai, G. A. *Phys. Rev. Lett.* **1998**, *80*, 1228-1231.

(2) Root, T. W.; Schmidt, L. D.; Fisher, G. B. *Surf. Sci.* **1983**, *134*, 30-45.

(3) Root, T. W.; Fisher, G. B.; Schmidt, L. D. *J. Chem. Phys.* **1986**, *85*, 4679-4686.

(4) Kim, Y. J.; Thevuthasan, S.; Herman, G. S.; Peden, C. H. F.; Chambers, S. A.; Belton, D. N.; Permana, H. *Surface Science* **1996**, *359*, 269-279.

(5) Borg, H. J.; Reijerse, J.; Vansanten, R. A.; Niemantsverdriet, J. W. *J. Chem. Phys.* **1994**, *101*, 10052-10063.

(6) Zasada, I.; Van Hove, M. A.; Somorjai, G. A. *Surf. Sci.* **1998**, *418*, L89-L93.

(7) Jensen, J. A.; Rider, K. B.; Chen, Y.; Salmeron, M.; Somorjai, G. A. *J. Vac. Sci. Technol. B* **1999**, *17*, 1080-1084.

(8) McIntyre, B. J.; Salmeron, M.; Somorjai, G. A. *Rev. Sci. Instrum.* **1993**, *64*, 687-691.

(9) Zang, Z. H.; Wu, Z. L.; Yau, S. L. *Langmuir* **1999**, *15*, 8750-8756.

(10) Castner, D. G.; Sexton, B. A.; Somorjai, G. A. *Surf. Sci.* **1978**, *71*, 519-540.

(11) Rider, K. B.; Hwang, K. S.; Salmeron, M.; Somorjai, G. A. *Phys. Rev. Lett.* **2001**, *86*, 4330-4333.

(12) Rose, M.; Salmeron, M., unpublished data.

(13) Rose, M.; Salmeron, M.; Sautet, P., unpublished data.

(14) This energy barrier is estimated using t (1 sec) = $\tau\exp(E/kT)$, with $\tau = 10^{-13}$ sec. A change of this value by an order of magnitude changes the value of E by 17%.

(15) Hill, T. L. *J. Chem. Phys.* **1949**, *17*, 520-535.

Chapter 5: CO/NO Structure on Rh(111)

This chapter discusses the coadsorption of CO and NO on Rh(111) at room temperature was studied with scanning tunneling microscopy (STM) in the catalytically relevant range of ~1 Torr, where the surface is in equilibrium with the gas mixture. For low NO partial pressures, a mixed layer with (2 × 2) structure is formed. The difference in binding energy between CO and NO on top sites was determined from the measured surface (by direct counting in STM images) and gas mole fractions of each species. A model for the molecular structure is proposed based on the analysis of exchange events between CO and NO molecules in the images. In this model as the partial pressure of NO increases, NO molecules occupy hollow sites first, by displacing CO, and top sites later, where they coexist with CO. As the surface fraction of NO increases, favorable NO-NO interactions cause the formation of segregated NO-rich regions. As with pure NO, a phase transition from the (2 × 2)-NO to the (3 × 3)-NO structure takes place in the NO-rich regions at high NO concentration.

5.1 Introduction

The interaction between coadsorbed CO and NO on rhodium is of interest due to the reduction of NO by CO in automobile catalytic converters. Modern engines produce exhaust gases with combined CO and NO partial pressures of approximately 5 Torr. Rhodium particles in the catalytic converter are responsible for catalyzing the reaction $CO + NO \rightarrow 1/2\ N_2 + CO_2$. Nearly all the kinetic models proposed [1-12] agree ([5] and [6] are exceptions) that the initial steps are the adsorption of CO and NO followed by the dissociation of NO. Although many studies in ultra high vacuum (UHV) and in ambient

pressures have been performed in an effort to understand this reaction [13], a detailed molecular understanding of the CO and NO structures and interactions in the Torr pressure range has not previously been acquired.

In this paper we report on investigations of the coadsorption of two molecules, CO and NO, at high pressures, in equilibrium with the gas phase using our high-pressure STM. We detected a mixed molecular surface structure with a (2 × 2) unit cell below 65% NO coverage. STM can monitor the exchange of CO and NO as the partial pressures of these gases are varied. The difference in CO and NO binding energies at top metal sites has been determined and the surface segregation of NO is monitored as the NO pressure is increased. The observations can be explained by a model in which CO and NO occupy and displace each other at top and hollow sites on the Rh(111) crystal face.

5.2 Experimental

All experiments were carried out in a system consisting of an ultra-high vacuum chamber containing the surface science analysis and preparation techniques, and a smaller chamber attached to it containing the STM [14,15]. The STM, from RHK Technologies, was operated in the 10^{-10} - 10^{3} Torr pressure and 300 K – 700 K temperature ranges. The base pressure of the system was 5×10^{-10} Torr, with the background made up primarily of H_2, CO, and water.

The sample was prepared by sputtering with 400 eV oxygen ions for 10 minutes followed by annealing in vacuum at 973 K for 2 minutes. Just before the sample was exposed to CO or NO, it was flashed again briefly to 973 K. The sample temperature

was monitored with a chromel-alumel thermocouple mounted in the sample holder in contact with the edge of the crystal, and sample cleanliness was checked with Auger spectroscopy. The clean, room temperature sample was then transferred to the STM chamber. Large scale images of the sample showed steps with no preferred orientation, with a spacing that corresponds to a crystal miscut angle less than 1º.

To prevent dissociation of NO, a surface layer of pure CO was prepared by establishing a background pressure of this gas of 10^{-7} Torr over the entire system. Then the gate valve separating the STM chamber from the chamber with the surface science instruments was closed. Because the background pressure was kept while the gate valve was being closed, CO was always the majority species in the gas phase. NO was added later in the STM chamber, after the desired CO pressure had been established. All STM images reported here were acquired with the sample at room temperature.

5.3 Results

5.3.1 Mixed (2 × 2)-3(CO-NO) Structure

Figure 5.1a shows an STM image of the (2 × 2) structure formed by CO and NO after addition of 0.15 Torr of NO to the initial 0.50 Torr CO pressure. Although most of the surface is covered with CO (each spot corresponding to a top CO site), new spots 0.3 Å higher than those from the surrounding CO appear (brighter spots). These bright spots represent 1% of the total in this case. Figure 5.1b shows the surface in a gas mixture consisting of 0.70 Torr of NO and 0.50 Torr of CO. In this case about a quarter of the spots changed contrast from dark to bright. As will be discussed below, the bright spots correspond to top-site NO molecules.

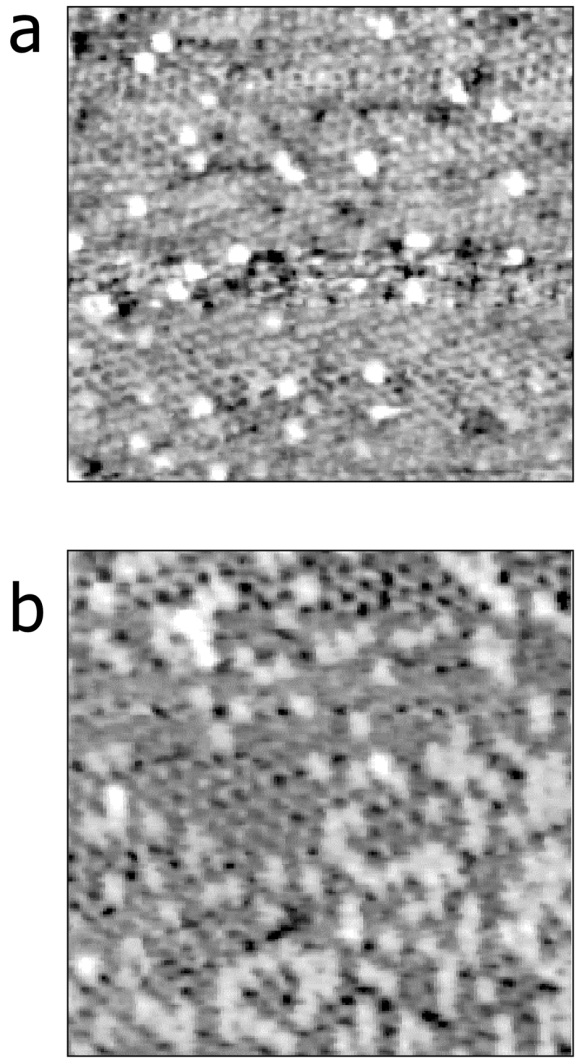

Figure 5.1 STM images of Rh(111) in equilibrium with a mixture of CO and NO. These 120 Å × 120 Å images display (2 × 2) pattern with a corrugation of 0.1 Å, which is characteristic of the (2 × 2)-3CO structure. The brighter unit cells are due to NO adsorption on the top-sites; neither CO nor NO can be seen when it is adsorbed on the hollow-sites. Image 1a was taken in 0.50 Torr CO + 0.15 Torr NO (I = 150 pA, V = 100 mV); image 1b was taken in 0.50 Torr CO + 0.70 Torr NO (I = 224 pA, V = 100 mV). The corrugation of the NO unit cells is 0.5 Å.

Figure 5.2 shows a plot of $1/x_{NO,t}$ vs. $1/x_{NO,g} - 1$, where $x_{NO,t}$ and $x_{NO,g}$ are the mole fractions of NO on surface top-sites and in the gas phase, respectively. The error bars were calculated from scans averaging 500 molecules each. Due to the finite size of the images it is not surprising that the larger error bars are obtained at the smallest NO coverage. As discussed below the slope of the straight line fit should be $e^{-\Delta Et/kT}$. The energy ΔE_t, is the difference between the heats of adsorption of CO and NO on top-sites in the coadsorbed layer ($E_{NO,t} - E_{CO,t}$). In spite of the scattering in the data, the exponential relationship greatly reduces the error in ΔE_t, which is found to be -66 ± 5 meV (=1.5 ± 0.1 kcal/mol).

5.3.2 Site Exchange Processes

When the surface is covered with pure CO or NO, sequential images of the same area appear identical, so that processes such as adsorption, desorption, and diffusion on the surface cannot be observed. When the surface contains both CO and NO, however, top site CO and NO can be distinguished. Inspection of successive images indicates that the surface remains remarkably unchanged except for a few occasional events where a bright spot changes into a dark one and vice-versa, indicating that CO and NO have desorbed, exchanged, or moved. Figure 5.3 shows a pair of images, each one acquired in 55 seconds, obtained sequentially on the same area of the surface. Careful inspection reveals a few displacements and/or substitutions, two of them marked with arrows. After analyzing ten successive images, each one containing roughly 400 top sites, 64 such events were recorded. This represents a small fraction of the top sites experiencing any change (64 in ~4000). The majority of events (56/64) correspond to CO and NO

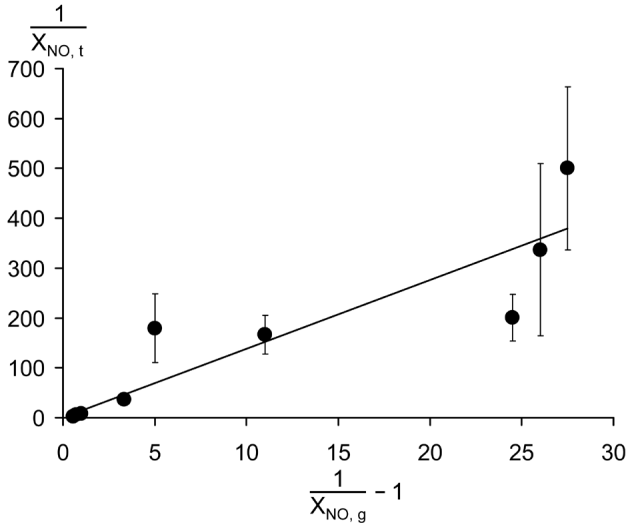

Figure 5.2 Plot of top-site NO coverage and NO partial pressure. $1/x_{NO,t}$ was plotted vs. $(1/x_{NO,g} - 1)$, where $x_{NO,t}$ is the mole fraction of NO on top-sites (obtained from the images), and $x_{NO,g}$ is the mole fraction of NO in the gas phase. The slope of the least squares fit line is $e^{-\Delta Et/kT}$, where ΔE_t is the difference in adsorption energy between CO and NO on the top-site. We calculate this difference to be -66 ± 5 meV. The negative sign indicates that CO binds more strongly to the top-site than NO.

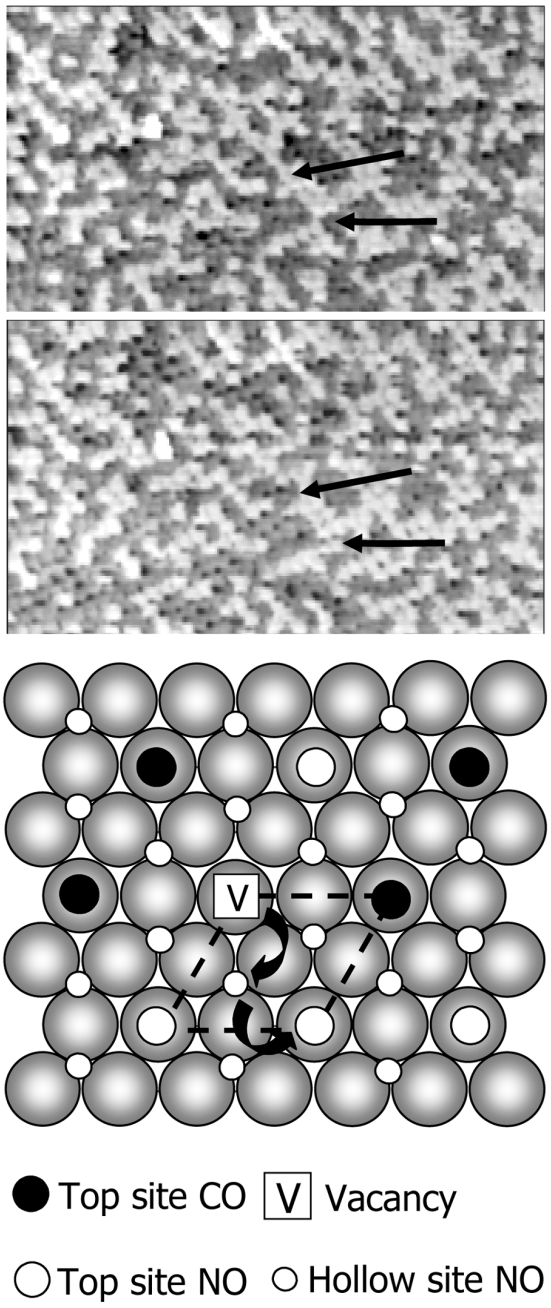

Figure 5.3 Pair of sequential STM images taken 55 seconds apart. These 200 Å × 115 Å images were taken on the same area of the surface in 0.50 Torr CO + 0.92 Torr NO (I = 260 pA, V = 50 mV). The top arrow shows one top-site occupied by NO in the top image and by CO in the bottom one. The bottom arrow shows the opposite. The diagram shows how a vacancy (boxed V) can diffuse across the unit cell and be substituted by a neighboring NO molecule, which is found in most of the hollow sites.

molecules apparently exchanging place with neighboring top sites. A much smaller fraction (5/64) corresponded to a molecule moving two unit cells away, and just 3/64 events resulted in the appearance or disappearance of a top-site NO molecule.

5.3.3 NO Segregation and Phase Transformation

Another interesting observation is that the spatial distribution of NO molecules is not random, particularly when the top-site occupation is near 50% NO. As the images in Figure 5.3 show, there is a preference for NO molecules to have other NO molecules in neighboring top sites, with a tendency to form chains along the substrate close packed directions.

When the NO partial pressure is two to four times greater than the CO partial pressure, segregation of areas that are rich in NO takes place producing bright and dark regions in the STM images. The bright regions are dominated by NO and often have elongated shapes as shown in the two images of Figure 5.4. At sufficiently high NO pressure, eventually (3 × 3) areas develop inside the bright NO-rich regions. The image in Figure 5.5 shows an example of a (3 × 3) region (enclosed by the white broken line) formed in the mixed CO-NO layer in equilibrium with 0.10 Torr CO and 0.32 Torr NO. As in the case of pure NO, the contrast in the (3 × 3) cells is even higher than that in the NO (2 × 2) cells.

The order of introduction of gases does not affect the final state of the surface. By alternately increasing the NO partial pressure and then the CO partial pressure, the surface structure can be changed from (2×2) to (3×3) and vice versa several times.

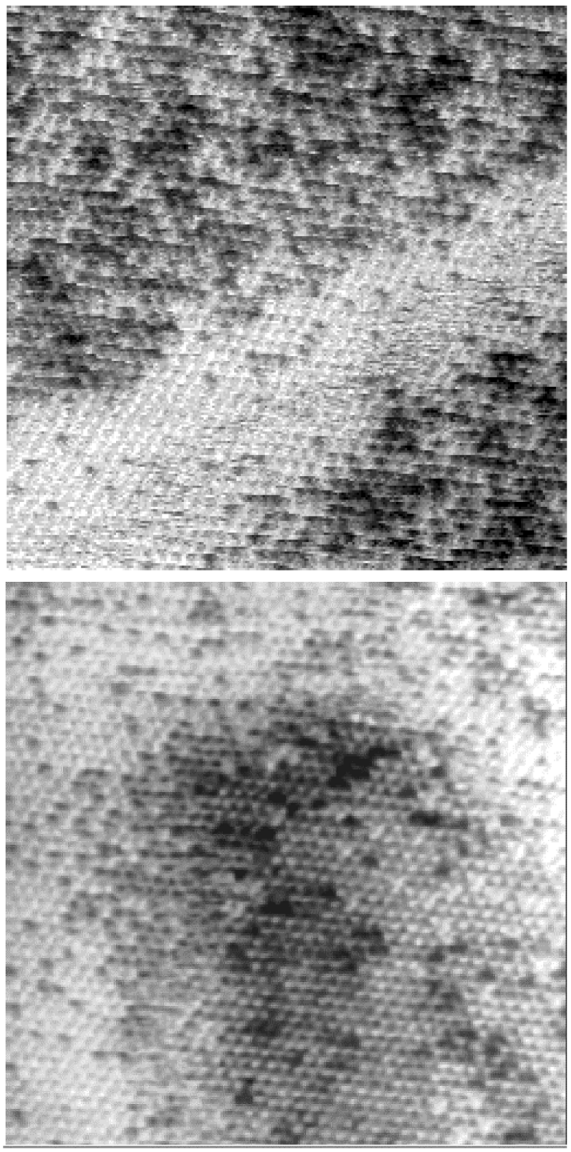

Figure 5.4 STM images showing formation of NO-rich regions. These 200 Å × 200 Å images were taken in 0.10 Torr CO + 0.32 NO (I = 177 mV, V = 100 mV). The (2 × 2) structure is visible with the top-sites being covered with a mixture of CO and NO. The brighter regions have a higher concentration of NO on the top-sites.

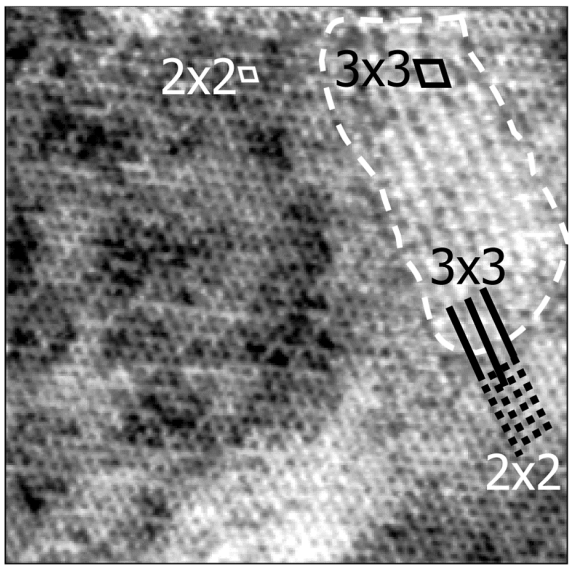

Figure 5.5 STM image showing formation of the (3 × 3) structure. The 200 Å × 200 Å image was taken in 0.10 Torr CO + 0.32 Torr NO (I = 190 pA, V = 100 mV). The brighter, nearly pure NO regions of the surface are the nucleation sites for the formation of the (3 × 3) structure that is characteristic of high-pressure NO adsorption. In the absence of CO, the (2 × 2) to (3 × 3) phase transition occurs when the pressure rises above 0.03 Torr.

5.4 Discussion

5.4.1 Mixed (2×2)-3(CO-NO) Structure

Carbon monoxide adsorbs molecularly [16-22] forming many different structures [16,23-29]. The known adsorption structures of CO are summarized in Table 5.1. The densest layer has a (2 × 2)-3CO structure with a unit cell containing one CO molecule in a top site and two molecules in three-fold hollow sites [20-22,30,31]. At 300 K this structure forms above 10^{-6} Torr and persists until the CO pressure is at least 700 Torr [32]. Two peaks, at 510 K and 430 K were observed by temperature programmed desorption (TPD), an indication that indeed two adsorption sites exist with different binding energy.

The adsorption of NO is more complex because it dissociates when the temperature is above 200 K and the coverage is below 1/3 ML [18,33-35]. Low energy electron diffraction (LEED) [36,37] and x-ray photoelectron diffraction (XPD) [38] studies have shown that at high coverage (0.75 ML) NO forms a (2 × 2)-3NO structure analogous to the one formed by CO. An important characteristic of the STM images of the dense (2 × 2) structures is that only top-site molecules produce a high contrast, while those bound to hollow sites have electronic structures and orbital symmetries that makes their contribution to the tunneling current much smaller than those on top-sites. Thus these molecules are not imaged [39].

Electron energy loss spectroscopy (EELS) and TPD experiments have shown that NO and CO have significantly different binding energies on the top and hollow sites [33,40]. In pure NO layers the molecule binds more strongly to hollow sites at both low

Surface Structure	**Coverage**	**Adsorption Sites**	**Reference**
(2×2)	0.25	Top	[19]
$(\sqrt{3} \times \sqrt{3})$R30º	0.33	Top	[17-19,27]
$(\sqrt{7} \times \sqrt{7})$R19º	0.43	Hollow	[32]
(2×1)	0.5	Top	[32]
$(\sqrt{7} \times \sqrt{7})$R19º	0.57	Top, Hollow	[32]
(2×2)	0.75	Top, Hollow	[18,19,22,27,28,31]
$(\sqrt{3} \times 7)$rect			[29]

Table 5.1 The known adsorption structures of CO on Rh(111)

and high coverage. In pure CO layers, however, the molecule binds more strongly to top sites at low coverage up to 0.3 monolayers (ML) but switches to hollow sites between 0.3 and 0.5 ML. At higher coverage, the top sites start to populate again [32]. When both molecules compete for sites, IR spectroscopy seems to indicate that under catalytic reaction conditions NO binds to hollow sites while CO binds to top sites [1,13].

Except when the NO partial pressure is very high, the surface shows a (2 × 2) structure formed by a mixture of molecules, as shown in Figures 5.1, 5.3 and 5.4. Since the number of bright spots is observed to increase with each increase in the NO partial pressure, we conclude that they correspond to the NO molecules. Unfortunately only the top site molecules are visible in the STM images, so no direct information on the other two molecules in the 3-fold hollow sites of the unit cell is available.

While we have not performed variable temperature experiments on this system, a previous STM study of pure NO on Rh(111) indicates that the surface is in equilibrium with the gas phase under the experimental conditions [41]. This was demonstrated by the observed phase transition between the (2 × 2) and (3 × 3)-NO structures, which occurred at the same temperature both after heating and cooling.

If the exchange of molecules between surface and gas phase molecules takes place primarily from top sites, which bind the molecules more weakly than the hollow sites, and if we assume that the binding energies on the top sites do not depend on the nature (CO or NO) of the surrounding molecules, then the gas and top-site mole fractions of CO and NO should be related by [42]:

$$\frac{x_{CO,t}}{x_{NO,t}} = \frac{x_{CO,g}}{x_{NO,g}} e^{-\Delta E_t / kT} \qquad (1)$$

where $x_{CO,t}$, $x_{NO,t}$ and $x_{CO,g}$, $x_{NO,g}$ are the mole fractions of CO and NO on surface top sites and in the gas phase, respectively. Later on we will discuss and justify these assumptions in more detail. The value of ΔE_t was found from the plot in Figure 5.2 to be -66 ± 5 meV, with the negative sign indicating that CO binds more strongly than NO on the top sites on the saturated surface. In spite of the large error in the values of the relative NO and CO top-site coverage, a relatively small value for error in the binding energy difference is obtained. This is due to the logarithmic dependence of ΔE_t on the mole fractions. One should keep in mind the limiting assumptions involved in (1), where interactions between neighboring top-site NO molecules were neglected. We know however that this interaction is important at high NO coverage and that it gives rise to the linear clustering and later segregation of NO-rich regions. For that reason the value of ΔE_t should be used with caution at high NO coverage, where (1) will predict values of $x_{NO,t}$ smaller than those found in the images.

Theoretical studies of low coverage and of isolated molecules predict that NO binds more strongly than CO on top sites [43,44]. However no calculations have been performed for the binding energy of the top sites in dense layers that could be compared with the present results.

5.4.2 Site Exchange Processes

The low frequency of events indicative of any molecular change in the images is at first remarkable. It indicates that in spite of the high collision rate of gas molecules per site ($\sim 10^6$ s^{-1} at 1 Torr), most of the impinging molecules are reflected back into the gas phase. It also shows a nearly complete immobility of the molecules, which can be

attributed to the dense packing, which blocks diffusion, and the near absence of vacancies. More quantitatively, the probability of a change was measured to be 64/4000 per site over a period of about 600 seconds during acquisition of the 10 consecutive images. It indicates that molecular desorption events occur at a frequency of $\nu = 2.7 \times 10^{-5}\ s^{-1}$. Using the Arrhenius form $\nu = 10^{12} \times e^{-Et/kT}\ s^{-1}$, we can estimate a binding energy E_t of 1.0 eV (=23 kcal/mol) assuming a pre-exponential factor of $10^{12}\ s^{-1}$ (the value of E_t would change by only 6% per order of magnitude change in the pre-exponential).

The value of 1 eV is smaller than the calculated values for top site adsorption in the low coverage ($\sqrt{3}\times\sqrt{3}$) structure of 1.68 eV and 1.90 eV for NO by van Santen et al. [43] and Sautet et al. [44] respectively, or of 1.46 eV for CO [43]. Our lower estimated value is not surprising however, because in the dense (2×2)-3(CO-NO) structure the top sites must feel the repulsion of the neighboring hollow site molecules. Because CO binds 66 meV stronger than NO, its rate of desorption should be approximately 13 times lower. As we discuss below, however, the visible events in the images are likely to be initiated by CO rather than NO desorption. The value of 1 eV estimated above could be better compared with the value we extrapolated from the CO TPD data of Root et al. [40], who studied the coadsorption of CO and NO. After NO exposure to the CO-covered surface, these authors found a shoulder at 370 K for CO desorption. This temperature implies a binding energy of 1.0 eV, which agrees with our estimate based on the observed frequency of changes (again with the same incertitude in the pre-exponential values).

These observations could be explained with the following model. We assume that when NO is introduced, it substitutes for CO primarily in the hollow sites. This is why the images in Figure 5.1 show only few bright NO spots, because only top-site NO is

visible. This assumption agrees with the TPD results of Root et al. [40] These authors observed that after exposing NO to the CO-saturated surface, CO desorbs almost exclusively in a TPD peak at the same temperature as the shoulder in the TPD of the (2 × 2) structure of pure CO, which is attributed to the top sites. NO desorbs later, after the CO has already completely desorbed.

From then on, with the population of hollow sites comprised largely of NO, the equilibrium with the gas phase is maintained by adsorption/desorption of CO and NO in top sites and lends justification *a posteriori* to the use of formula (1) above. Once a vacancy is produced by a desorption event, it can be filled either directly from the gas phase or by diffusion of an NO molecule from a neighboring hollow site (see diagram in Figure 5.3). Unless kinetic barriers to adsorption are assumed, direct filling at this point from the gas phase should lead to a nearly 50% chance that an original top-site NO (which should desorb 13 times more frequently than CO) would be replaced by a CO for a gas composed of 50% NO, thus yielding a net loss of one bright site. Similarly, a desorbing top-site CO immediately filled by a gas phase molecule has about a 50% chance of leading to a net gain of a bright spot. Clearly this is not what is observed, since this would imply many instances of independent gains or losses instead of just exchanges.

It appears then that vacancy diffusion to a neighboring hollow site is more likely. A desorbing top-site CO could then be filled by an adjacent hollow-site NO, changing its appearance in the STM images from dark to bright; if the desorbing molecule was NO instead, refilling by an adjacent hollow site NO molecule would not change top-site contrast and the event would not be observable by STM. The hollow-site vacancy will probably continue to diffuse to a top site occupied by NO since its binding energy is

lower (by 66 meV) and finally be refilled from the gas phase. This top site is probably very close to the original, since at room temperature its lifetime should be very short. Restoration of the equilibrium fractional coverages demands that, in the average, a CO molecule from the gas phase should fill the vacancy. The details of the mechanisms involved are not presently understood, though they probably must include the energetics of the interactions between neighboring CO and NO molecules and their dependence on site geometry. Better statistics and more experimental data are necessary to fully understand this.

5.4.3 NO Segregation and Phase Transformation

The alignment of top-site NO molecules observed in Fig. 3 suggests that second nearest neighbor (top-site/top-site) NO-NO interactions are more favorable than NO-CO interactions. This implies also that the difference between the NO-NO and NO-CO second nearest interactions is of the order of kT, 25 meV (=kT at room temperature). For comparison, at low coverage ($\theta = 1/3$), Payne et al. [25] reported a CO-CO attraction of 7 meV. At higher partial pressures of NO, where images show light and dark areas as in Figure 5.4, the degree of brightness is probably correlated with the concentration of NO.

In previous work, we reported that pure NO forms a (2×2)-3NO structure in equilibrium with the gas phase up to 0.03 Torr and then undergoes a phase transition to a (3×3)-7NO structure [41]. In this new structure, the top NO is again the only molecule imaged by the STM in the unit cell. In addition, it shows higher contrast than that of the top site in the (2×2)-3NO structure. The presence of CO considerably alters the equilibrium NO pressure required for this transition, which now occurs at a much higher

NO partial pressure. When this pressure is high enough, however, (3 × 3) areas develop inside the bright regions, as shown in Figure 5.5. As indicated above, in order for the (3 × 3) structure to form the NO partial pressure must be three to five times greater than the CO partial pressure at room temperature. For 0.1 Torr of CO, for example, this is ten times larger than that required with pure NO.

In addition to occurring in the (3 × 3) areas, high-contrast top-site NO molecules that are brighter than those normally found in the (2 × 2) structure have been occasionally observed in isolation. This is presumably a precursor to an entire island of (3 × 3). This result suggests that the high contrast present in the (3 × 3)-7NO structure is not due to a larger unit cell allowing the tip to better follow the molecular contours, as these isolated high-contrast NO molecules occur in a (2 × 2) unit cell.

5.5 Conclusions

We have studied the molecular structure of the surface layer formed on Rh(111) in equilibrium with NO-CO gas mixtures at partial pressures in the regime relevant to automobile catalytic converters. At low NO partial pressures, the molecules mix into a (2 × 2)-3(CO-NO) structure. In the dense (2 × 2) structures formed at high pressure, neither CO nor NO is visible in the STM images when adsorbed on hollow-sites. They do appear as distinct spots when on top sites with an apparent height difference of 0.3 Å in favor of NO. From the equilibrium concentration of top site molecules, we find that top-site CO is more stable than top-site NO by 66 ± 5 meV.

Based on the low rate of changes and the NO pressure necessary to produce bright NO spots in the images, we have proposed a model where NO substitutes for CO in the

hollow sites first and then on the top sites later. Molecular desorption from the top sites occurs at frequencies of the order of 10^{-5} s^{-1}, which implies an adsorption energy of 1.0 eV. The occasional exchange of contrast observed in the STM images between neighboring CO and NO top sites is explained by a vacancy- mediated diffusion mechanism, though the details are not presently understood.

There appears to be a slight preference for NO molecules to occupy adjacent top-sites in the (2 × 2) lattice, which causes the formation of NO-rich islands at higher NO partial pressures. The presence of CO in the gas phase increases the NO partial pressure that is necessary for the formation of the NO (3 × 3) structure until the NO partial pressure is three to five times greater than the CO partial pressure. When the (3 × 3) structure forms, it nucleates on the NO-rich areas mentioned above.

References

(1) Permana, H.; Ng, K. Y. S.; Peden, C. H. F.; Schmieg, S. J.; Lambert, D. K.; Belton, D. N. *J. Catal.* **1996**, *164*, 194-206.

(2) Campbell, C. T.; White, J. M. *Appl. Surf. Sci.* **1978**, *1*, 347-359.

(3) Dubois, L. H.; Hansma, P. K.; Somorjai, G. A. *J. Catal.* **1980**, *65*, 318-327.

(4) Hecker, W. C.; Bell, A. T. *J. Catal.* **1983**, *84*, 200-215.

(5) Hendershot, R. E.; Hansen, R. S. *J. Catal.* **1986**, *98*, 150-165.

(6) Lintz, H. G.; Weisker, T. *Appl. Surf. Sci.* **1985**, *24*, 259-267.

(7) Schwartz, S. B.; Fisher, G. B.; Schmidt, L. D. *Journal of Physical Chemistry* **1988**, *92*, 389-395.

(8) Peden, C. H. F.; Goodman, D. W.; Blair, D. S.; Berlowitz, P. J.; Fisher, G. B.; Oh, S. H. *Journal of Physical Chemistry* **1988**, *92*, 1563-1567.

(9) Cho, B. K.; Shanks, B. H.; Bailey, J. E. *J. Catal.* **1989**, *115*, 486-499.

(10) Ng, K. Y. S.; Belton, D. N.; Schmieg, S. J.; Fisher, G. B. *J. Catal.* **1994**, *146*, 394-406.

(11) Peden, C. H. F.; Belton, D. N.; Schmieg, S. J. *J. Catal.* **1995**, *155*, 204-218.

(12) Permana, H.; Ng, K. Y. S.; Peden, C. H. F.; Schmieg, S. J.; Belton, D. N. *Journal of Physical Chemistry* **1995**, *99*, 16344-16350.

(13) Zhdanov, V. P.; Kasemo, B. *Surf. Sci. Rep.* **1997**, *29*, 35-90.

(14) Jensen, J. A.; Rider, K. B.; Chen, Y.; Salmeron, M.; Somorjai, G. A. *J. Vac. Sci. Technol. B* **1999**, *17*, 1080-1084.

(15) McIntyre, B. J.; Salmeron, M.; Somorjai, G. A. *Rev. Sci. Instrum.* **1993**, *64*, 687-691.

(16) Peterlinz, K. A.; Curtiss, T. J.; Sibener, S. J. *J. Chem. Phys.* **1991**, *95*, 6972-6985.

(17) Koestner, R. J.; Van Hove, M. A.; Somorjai, G. A. *Surf. Sci.* **1981**, *107*, 439-458.

(18) Castner, D. G.; Sexton, B. A.; Somorjai, G. A. *Surf. Sci.* **1978**, *71*, 519-540.

(19) Thiel, P. A.; Williams, E. D.; Yates, J. T.; Weinberg, W. H. *Surf. Sci.* **1979**, *84*, 54-64.

(20) Beutler, A.; Lundgren, E.; Nyholm, R.; Andersen, J. N.; Setlik, B.; Heskett, D. *Surf. Sci.* **1997**, *371*, 381-389.

(21) Beutler, A.; Lundgren, E.; Nyholm, R.; Andersen, J. N.; Setlik, B. J.; Heskett, D. *Surf. Sci.* **1998**, *396*, 117-136.

(22) Gierer, M.; Barbieri, A.; Van Hove, M. A.; Somorjai, G. A. *Surf. Sci.* **1997**, *391*, 176-182.

(23) Wei, D. H.; Skelton, D. C.; Kevan, S. D. *Surf. Sci.* **1997**, *381*, 49-64.

(24) Payne, S. H.; Jun, Z.; Kreuzer, H. J. *Surf. Sci.* **1992**, *264*, 185-196.

(25) Payne, S. H.; Kreuzer, H. J.; Peterlinz, K. A.; Curtiss, T. J.; Uebing, C.; Sibener, S. J. *Surf. Sci.* **1992**, *272*, 102-110.

(26) Peterson, L. D.; Kevan, S. D. *J. Chem. Phys.* **1991**, *94*, 2281-2293.

(27) Delouise, L. A.; White, E. J.; Winograd, N. *Surf. Sci.* **1984**, *147*, 252-262.

(28) Grant, J. T.; Haas, T. W. *Surf. Sci.* **1970**, *21*, 76-&.

(29) Mate, C. M.; Bent, B. E.; Somorjai, G. A. *J. Electron Spectrosc. Relat. Phenom.* **1986**, *39*, 205-212.

(30) Van Hove, M. A.; Koestner, R. J.; Somorjai, G. A. *Phys. Rev. Lett.* **1983**, *50*, 903-906.

(31) Van Hove, M. A.; Koestner, R. J.; Frost, J. C.; Somorjai, G. A. *Surf. Sci.* **1983**, *129*, 482-506.

(32) Cernota, P.; Rider, K.; Yoon, H. A.; Salmeron, M.; Somorjai, G. *Surf. Sci.* **2000**, *445*, 249-255.

(33) Root, T. W.; Fisher, G. B.; Schmidt, L. D. *J. Chem. Phys.* **1986**, *85*, 4679-4686.

(34) Root, T. W.; Schmidt, L. D.; Fisher, G. B. *Surf. Sci.* **1983**, *134*, 30-45.

(35) Borg, H. J.; Reijerse, J.; van Santen, R. A.; Niemantsverdriet, J. W. *J. Chem. Phys.* **1994**, *101*, 10052-10063.

(36) Kao, C. T.; Blackman, G. S.; Van Hove, M. A.; Somorjai, G. A.; Chan, C. M. *Surf. Sci.* **1989**, *224*, 77-96.

(37) Zasada, I.; Van Hove, M. A.; Somorjai, G. A. *Surf. Sci.* **1998**, *418*, L89-L93.

(38) Kim, Y. J.; Thevuthasan, S.; Herman, G. S.; Peden, C. H. F.; Chambers, S. A.; Belton, D. N.; Permana, H. *Surf. Sci.* **1996**, *359*, 269-279.

(39) Sautet, P.; Rose, M. K.; Dunphy, J. C.; Behler, S.; Salmeron, M. *Surf. Sci.* **2000**, *453*, 25-31.

(40) Root, T. W.; Schmidt, L. D.; Fisher, G. B. *Surf. Sci.* **1985**, *150*, 173-192.

(41) Rider, K. B.; Hwang, K. S.; Salmeron, M.; Somorjai, G. A. *Phys. Rev. Lett.* **2001**, *86*, 4330-4333.

(42) It is also assumed that the pre-exponential factors for CO and NO desorption are the same.

(43) Koper, M. T. M.; van Santen, R. A.; Wasileski, S. A.; Weaver, M. J. *J. Chem. Phys.* **2000**, *113*, 4392-4407.

(44) Loffreda, D.; Simon, D.; Sautet, P. *Chem. Phys. Lett.* **1998**, *291*, 15-23.

Chapter 6: CO/NO Reaction on Rh(111)

The previous chapter described how CO and NO adsorb and order on Rh(111) at room temperature. The high-pressure results are a step closer to the realistic pressure conditions of a catalytic converter. This chapter describes experiments in the mTorr and Torr pressure ranges that took the next step and elevated the temperature in order to increase the rate catalytic converter reactions. Upon heating to 473 K, step mobility was observed by scanning tunneling microscopy (STM) while the reaction was tracked by mass spectrometry (MS). As the temperature was increased to over 523 K, mobility decreased, possibly due to a decreased residence time of adsorbate molecules. The apparent activation energy of the reaction was calculated to be 34 kcal/mol.

6.1 Introduction

Studying the reaction of CO and NO on Rh(111) is important because this system is a model for the automobile catalytic converter. Typical automobile exhaust consists of about 5 Torr total of CO and NO [1]. In order to reduce pollutants, automobiles use a three-way catalyst that contains three catalytic metals: Pt, Pd, and Rh. Rh is essential for the reduction of NO to N_2, by the following reaction: $CO + NO \rightarrow 1/2\ N_2 + CO_2$. There are numerous mechanisms proposed [2-13], a commonly accepted one is:

$$NO_{gas} \rightleftarrows NO_{ads}$$

$$CO_{gas} \rightleftarrows CO_{ads}$$

$$NO_{ads} \rightarrow N_{ads} + O_{ads}$$

$$2N_{ads} \rightarrow (N_2)_{gas}$$

$$CO_{ads} + O_{ads} \rightarrow (CO_2)_{ads}.$$

As discussed later, this mechanism does not include a possible side reaction involving the formation of N_2O. While reaction kinetics have been extensively studied under a wide range of pressures, a microscopic view of how the Rh surface looks during the reaction has not yet been acquired.

We have studied the reaction of CO and NO on Rh(111) in the mTorr and Torr pressure regimes using STM and MS. The apparent activation energy of the reaction was calculated and compared to existing theoretical and experimental values. STM studies showed that during the reaction, the steps of Rh appear to be mobile.

6.2 Experimental

All experiments were performed in the high-pressure, high-temperature scanning tunneling microscope (HPHTSTM) apparatus described in Chapter 3. It was operated from 10^{-10} to 10^{3} Torr in pressure and from 298 K to 573 K in temperature. The base pressure of 5×10^{-10} Torr consisted mainly of H_2, CO, and water. Both STM and MS experiments were performed in the STM chamber, with MS measurements taken by using a feedthrough from the STM chamber to a leak valve below the MS on the UHV chamber.

The sample was prepared by sputtering with 400 eV oxygen ions for 10 minutes followed by annealing in vacuum at 973 K for 2 minutes. Just before the sample was exposed to reaction gases, it was flashed again briefly to 973 K. The sample temperature was monitored with a chromel-alumel thermocouple mounted in the sample holder in contact with the edge of the crystal, and sample cleanliness was checked with Auger spectroscopy. The clean, room temperature sample was then transferred to the STM

chamber. Large scale images of the sample showed steps with no preferred orientation, with a spacing that corresponds to a crystal miscut angle less than 1º.

To prevent dissociation of NO, a surface layer of pure CO was prepared by establishing a background pressure of this gas of 10^{-7} Torr in the STM chamber after transfer of the sample. Because the background pressure was kept while the gate valve to the ion pump was being closed, CO was always the majority species in the gas phase. NO was added later in the STM chamber, after the desired CO pressure had been established.

6.3 Results and Discussion: Mass Spectrometry

Using a 4 ft. long feedthrough from the STM chamber to the UHV chamber, reactions in the STM chamber can be monitored using mass spectrometry. For the reaction of CO and NO on Rh(111), masses 28 (CO and N_2), 30 (NO), 44 (CO_2), and 18 (water as an unchanging standard) are monitored. The reaction was studied in the mTorr pressure range from 469 K to 535 K. At the lower temperature bound, STM experiments suggest step mobility, as described below. The upper temperature bound is near the maximum operating temperature of the STM.

Typical spectra, taken after starting with 10 mTorr each of CO and NO, are shown in Figure 6.1. In all spectra, mass 28 is the most abundant and mass 18 remains negligible. Mass 30 is the second most abundant in the room temperature and 480 K spectra, while mass 44 is second in the 535 K spectrum. CO appears much higher than NO due to background CO present in the feedthrough, and is normalized for in the rate calculations.

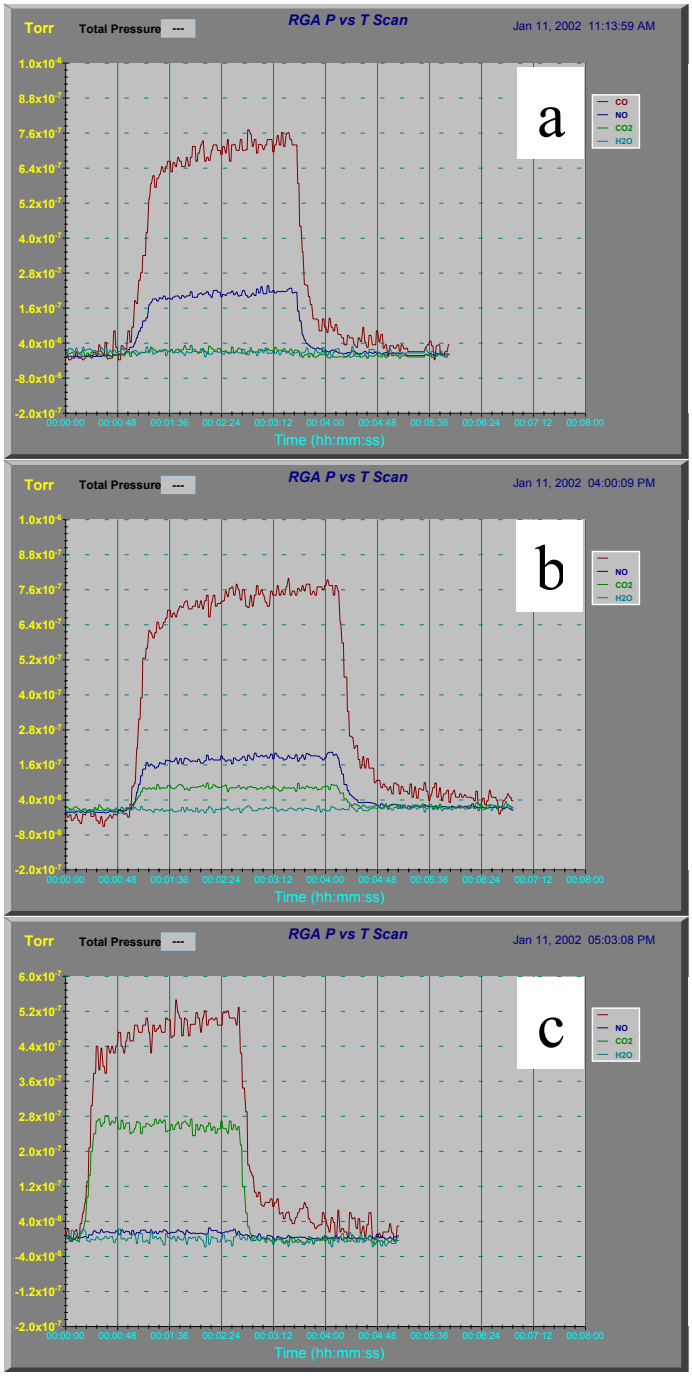

Figure 6.1 Mass spectra showing the reaction of NO and CO on Rh(111). The starting gas mixture in each gas was 10 mTorr each of CO and NO. Spectrum (a) was taken at 298 K, spectrum (b) was taken at 480 K after 4.5 hrs., and spectrum (c) was taken at 535 K after 1.0 hr. In all spectra, mass 28 is the most abundant and mass 18 remains negligible. Mass 30 is the second most abundant in the room temperature and 480 K spectra, while mass 44 is second in the 535 K spectrum.

To calculate the reaction rate, the decrease of NO and increase of CO_2 were measured as the indicators of reaction progress. Mass 28 contained contributions from both CO, a product, and N_2, a reactant. After normalizing for the excess CO background, the measured MS results were used to identify the ratios of gases in the feedthrough and hence the STM chamber. From the known initial gas pressures, the final gas pressures can be calculated after examining the overall equation $CO + NO \rightarrow 1/2\ N_2 + CO_2$:

$$P_f^{28} = P_i^{28} - \tfrac{1}{2}x$$

$$P_f^{30} = P_i^{30} - x$$

$$P_f^{44} = x,$$

where x is determined by comparison with the final gas ratios. With the initial and final pressures known, the moles of product can be calculated using the Ideal Gas Law:

$$PV = nRT,$$

where V is the known volume of the STM chamber, 10 L. From this a turnover rate in molecules $site^{-1}\ s^{-1}$ can be calculated:

$$k = \frac{n/N_A}{A \cdot t}\ [14],$$

where n moles of product are produced in time t, and A is the number of active sites on the catalyst. In this case, the sample is a flat disc with a diameter of 1 cm, and A can be calculated since there are three active sites per (2 × 2) unit cell, as shown in Chapter 4.

By measuring the turnover rate at different temperatures, the apparent activation energy for the reaction can be calculated using the Arrhenius equation:

$$k = \nu e^{-E_a/RT}.$$

Figure 6.2 shows a plot of ln(k) vs. 1/T of the CO/NO reaction starting with 10 mTorr each of CO and NO. From the slope of this line, the apparent activation energy of the CO/NO reaction is 34 kcal/mol. This is significantly higher than the 24 kcal/mol predicted by theory [15]. One possible explanation for this is that a side reaction, $NO_{ads} + N_{ads} \rightarrow (N_2O)_{gas}$, was not accounted for in the mechanism we used.

Belton et al. [2,12,13] showed that at elevated pressures, the N_2O formation reaction does occur in the CO/NO system, with the selectivity for N_2O increasing with increasing temperature below 550 K. If this reaction were occurring in our system, then our apparent activation energy would be too high. Unfortunately, we are currently unable to determine whether or not this is the case, as N_2O has the same mass as CO_2.

Due to limitations of the feedthrough, MS measurements are best done in the mTorr pressure range. Since the diameter of the feedthrough is ¼" for much of its length, diffusion limits the MS response time at higher pressures, as seen in Figure 6.3. Here the ratio of masses 28 to 30 does not noticeably change after over an hour, even at 530 K. There are trace amounts of CO_2 since the pressure was increased to the Torr range after a mTorr reaction had previously been run without pumping in between.

6.4 Results and Discussion: Scanning Tunneling Microscopy

The surface was studied by STM under reaction conditions in the mTorr and Torr pressure ranges of CO and NO. Above 400 K, molecular resolution is lost in the STM, presumably due to the mobility of adsorbate molecules on the surface. Below 473 K, steps remain clearly visible and well defined in environments of CO and NO from 10 mTorr of each gas to 1 Torr of each gas. Starting at 473 K, step edges start to blur and in

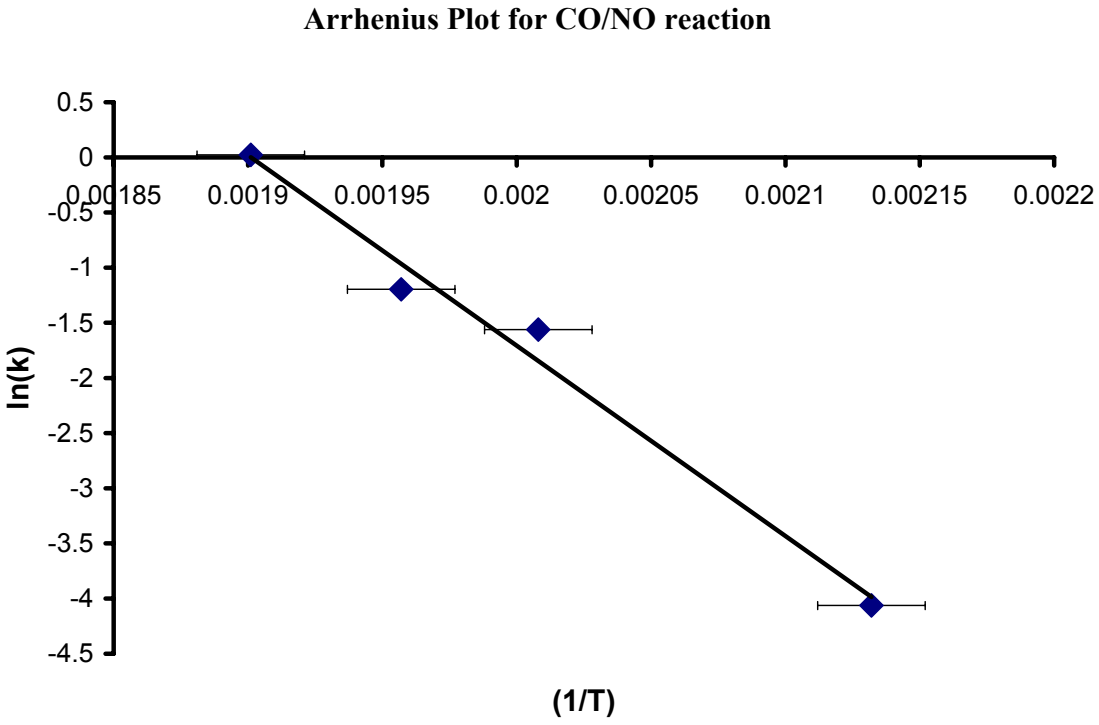

Figure 6.2 Arrhenius plot used to calculate the apparent activation energy for the CO/NO reaction on Rh(111). The slope of the line is $-E_a/R$. The apparent activation energy found is 34 kcal/mol.

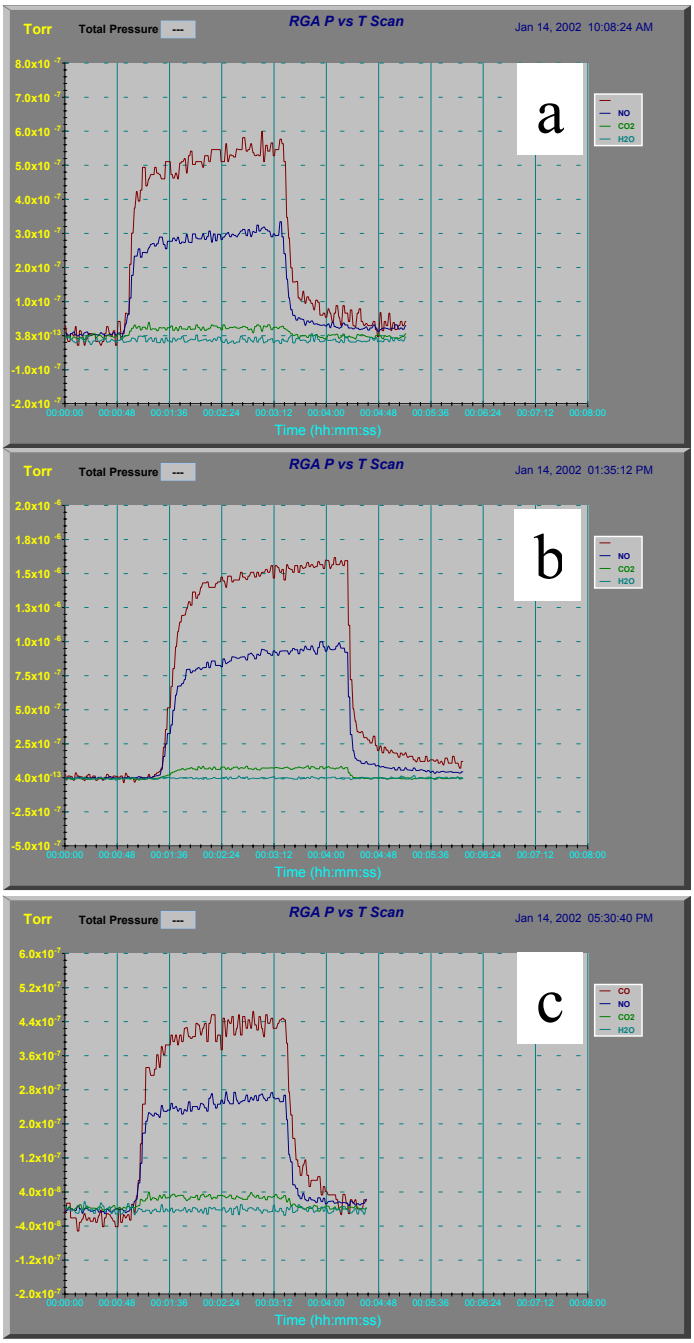

Figure 6.3 Mass spectra taken after starting with 1 Torr each of CO and NO on Rh(111). Spectrum (a) was taken at 298 K, spectrum (b) was taken at 474 K after 2 hrs., and spectrum (c) was taken at 530 K after 1 hr. In all spectra, mass 28 is the most abundant, mass 30 is the second most abundant and masses 18 and 44 remain negligible. The reduced amount of product detected at elevated temperatures is due to instrumental limitations when operating in the Torr pressure regime.

some cases disappear entirely, as shown in Figures 6.4 and 6.5. This is not simply due to the destruction of the tip, as step edges become visible and sharply defined again if the surface is cooled back to room temperature. Interestingly, at 10 mTorr each of CO and NO, step-edge definition returns if the surface is heated above 523 K, as shown in Figure 6.4. While visible, steps do not appear sharp at 523 K in 1 Torr each of CO and NO, as shown in Figure 6.5.

Step-edge mobility and surface restructuring has been previously observed under high pressures of reactive gases [16,17]. In appears in this case that reacting adsorbate molecules cause increased mobility in metal surface atoms. As the temperature increases, there will be fewer molecules on the surface. It is possible that at 523 K in 20 mTorr of gas, there are not enough adsorbate molecules on the surface to increase the surface mobility of metal atoms. When the pressure is increased by two orders of magnitude, enough molecules may be on the surface to cause step-edge mobility.

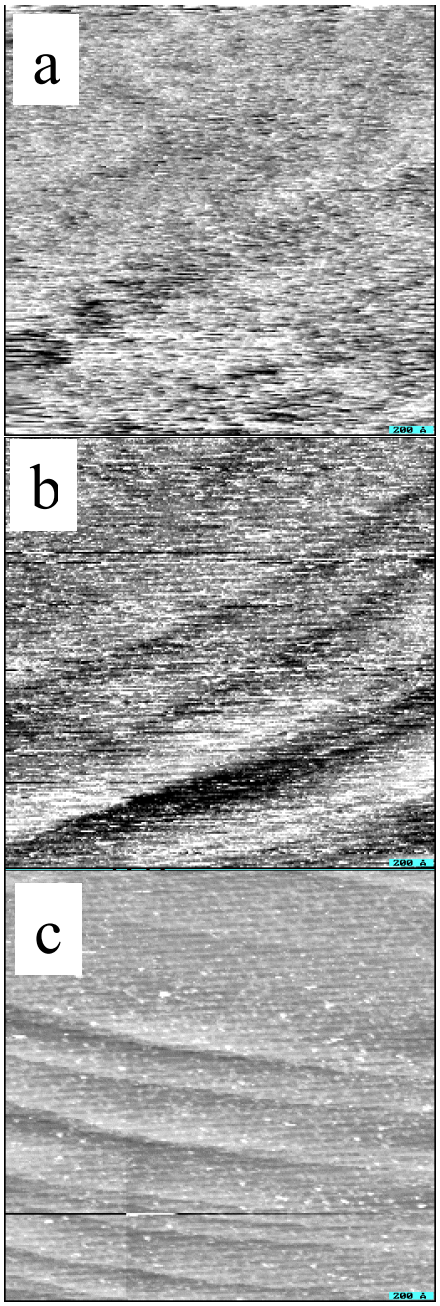

Figure 6.4 STM images of Rh(111) during the CO/NO reaction. These 2000 Å × 2000 Å images were taken after the chamber was filled with 10 mTorr each of CO and NO. Image (a) was taken at 476 K, image (b) was taken at 493 K, and image (c) was taken at 536 K. Images (a) and (b) show blurred step edges, indicating mobile surface atoms. In image (c), the step edges are as sharp as they appear at room temperature.

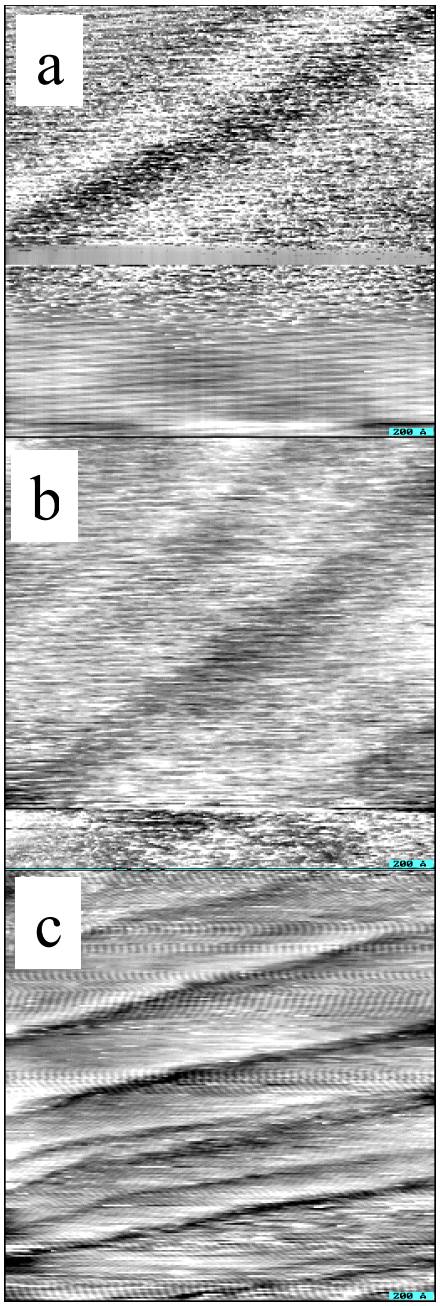

Figure 6.5 STM images of Rh(111) during the CO/NO reaction. These 2000 Å × 2000 Å images were taken after the chamber was filled with 1 Torr each of CO and NO. Image (a) was taken at 474 K, image (b) was taken at 498 K, and image (c) was taken at 526 K. Images (a) and (b) show blurred step edges, indicating mobile surface atoms. In image (c), the step edges are sharper, but as well defined as they appear at room temperature.

6.5 Conclusions

The reaction of CO and NO was studied on Rh(111) using a high-pressure, high-temperature STM and MS. Using a feedthrough from the high-pressure STM chamber to the MS on the UHV chamber, the reaction was monitored from 473 K to 533 K. Using the measured rates at different temperatures, the apparent activation energy was found to be 34 kcal/mol. This is higher than theoretical predications, most likely due to a side reaction producing N_2O that we did not account for. STM results showed that steps remained well defined until the temperature was increased to 473 K. Then the steps blurred, possibly due adsorbate-induced metal atom mobility. As the temperature continued to increase, metal atom mobility slowed, as the steps regained their distinct edges. This happened earlier at lower pressures, suggesting that many molecules need to be adsorbed before there is much metal atom mobility.

References

(1) Taylor, K. C. *Catal. Rev.-Sci. Eng.* **1993**, *35*, 457-481.

(2) Permana, H.; Ng, K. Y. S.; Peden, C. H. F.; Schmieg, S. J.; Lambert, D. K.; Belton, D. N. *J. Catal.* **1996**, *164*, 194-206.

(3) Campbell, C. T.; White, J. M. *Appl. Surf. Sci.* **1978**, *1*, 347-359.

(4) Dubois, L. H.; Hansma, P. K.; Somorjai, G. A. *J. Catal.* **1980**, *65*, 318-327.

(5) Hecker, W. C.; Bell, A. T. *J. Catal.* **1983**, *84*, 200-215.

(6) Hendershot, R. E.; Hansen, R. S. *J. Catal.* **1986**, *98*, 150-165.

(7) Lintz, H. G.; Weisker, T. *Appl. Surf. Sci.* **1985**, *24*, 259-267.

(8) Schwartz, S. B.; Fisher, G. B.; Schmidt, L. D. *J. Phys. Chem.* **1988**, *92*, 389-395.

(9) Peden, C. H. F.; Goodman, D. W.; Blair, D. S.; Berlowitz, P. J.; Fisher, G. B.; Oh, S. H. *J. Phys. Chem.* **1988**, *92*, 1563-1567.

(10) Cho, B. K.; Shanks, B. H.; Bailey, J. E. *J. Catal.* **1989**, *115*, 486-499.

(11) Ng, K. Y. S.; Belton, D. N.; Schmieg, S. J.; Fisher, G. B. *J. Catal.* **1994**, *146*, 394-406.

(12) Peden, C. H. F.; Belton, D. N.; Schmieg, S. J. *J. Catal.* **1995**, *155*, 204-218.

(13) Permana, H.; Ng, K. Y. S.; Peden, C. H. F.; Schmieg, S. J.; Belton, D. N. *J. Phys. Chem.* **1995**, *99*, 16344-16350.

(14) Somorjai, G. A. *Introduction to Surface Chemistry and Catalysis*; John WIley & Sons: New York, 1994.

(15) Zhdanov, V. P.; Kasemo, B. *Surf. Sci. Rep.* **1997**, *29*, 35-90.

(16) Rider, K. B. *Ph.D. Thesis, University of California* **2001**.

(17) Hendriksen, B. L. M.; Frenken, J. W. M. *Phys. Rev. Lett.* **2002**, *89*, art. no.-046101.

Chapter 7: Ethylene Hydrogenation and CO Poisoning on Rh(111) and Pt(111): Structure and Reaction

In an effort to obtain molecular-resolution images with the high-pressure scanning tunneling microscope (STM), ethylene hydrogenation and its poisoning was studied, as ethylene hydrogen is fast enough at room temperature to monitor with a mass spectrometer (MS) or gas chromatograph (GC). This chapter describes STM experiments on CO poisoning of ethylene hydrogenation on platinum and rhodium single crystals. Reaction studies using gas chromatography on Pt(111) show that CO poisons the reaction, and the measured activation energy in the presence of CO (20.2 kcal/mol) is higher than without CO (9.6 kcal/mol). Similarly, CO on platinum nanoparticles reduces the reaction rate of ethylene hydrogenation, though the activation energy does not change significantly. STM studies on Rh(111) and Pt(111) show that in the absence of CO, hydrogen and ethylidyne species that are present on the surface in large concentrations diffuse rapidly on the surface and thus, cannot be imaged. When CO is introduced, ordered structures appear on the surface. Based on these results, a model is proposed for CO poisoning on single crystals in which CO adsorbs on vacant hollow sites, preventing the diffusion of ethylidyne. With the immobile adsorbates filling the surface, ethylene from the gas phase has no room to adsorb, and ethylene hydrogenation is prevented.

7.1 Introduction

The metal catalyzed hydrogenation of ethylene was discovered by Sabatier [1], and it was an important part of his Nobel Prize winning research. This was the first catalytic reaction for which a mechanism was proposed in 1934 by Horiuti and Polanyi

[2], which postulated hydrogen molecule dissociation on the metal surface and the sequential hydrogenation of ethylene to C_2H_5 and then to C_2H_6. Since the late seventies our laboratory was engaged in molecular studies of the mechanism of this reaction on platinum and rhodium crystal surfaces, and a detailed picture of many of the elementary reaction steps has emerged. Using low energy electron diffraction (LEED) and sum frequency generation (SFG)-surface vibrational spectroscopy, the structure of adsorbates has been determined [3-7]. Three species: π-bonded ethylene (C_2H_4), di-σ bonded ethylene (C_2H_4), and ethylidyne (C_2H_3), have been identified on the surface under reaction conditions, see Figure 7.1. The latter two species are bound to the metal surfaces strongly enough to be stable even in vacuum. π-bonded ethylene is weakly bound and present on the surface only at high pressures of hydrogen and ethylene under the reaction conditions. Scanning tunneling microscopy (STM) studies [8] and modeling [9] indicate that the ethylidyne species are mobile on the surface at 300 K shuttling between 3-fold fcc and hcp sites with an activation energy of 0.1 eV. Ethylidyne also restructures the Pt(111) and Rh(111) surfaces as it forms, as has been detected by LEED surface crystallography studies. These structures are shown in Figure 7.2 [10]. This restructuring is also confirmed by density functional theory studies [11].

A mechanism for ethylene hydrogenation involving several elementary reaction steps can be proposed based on experimental observations, as displayed in Figure 7.3. In this mechanism, hydrogen molecules adsorb dissociatively on an ethylidyne-covered metal surface. Ethylidyne diffusion between fcc and hcp 3-fold hollow sites opens up holes in the ethylidyne overlayer where π-bonded ethylene weakly adsorbs on the metal. The ethylene is then stepwise hydrogenated through an ethyl intermediate to ethane.

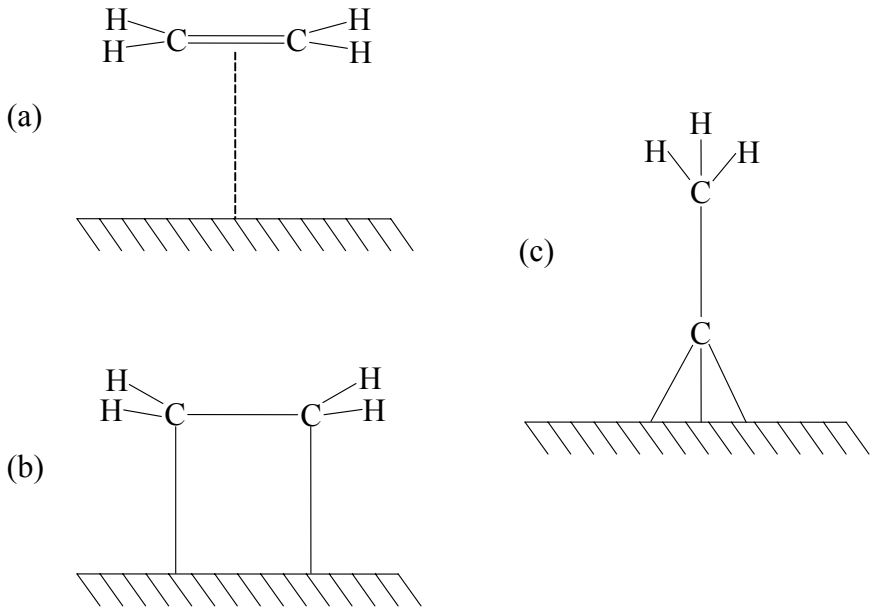

Figure 7.1 The three surface structures formed by adsorbed ethylene on Pt(111) and Rh(111): a) π-bonded ethylene. b) di-σ bonded ethylene. c) ethylidyne.

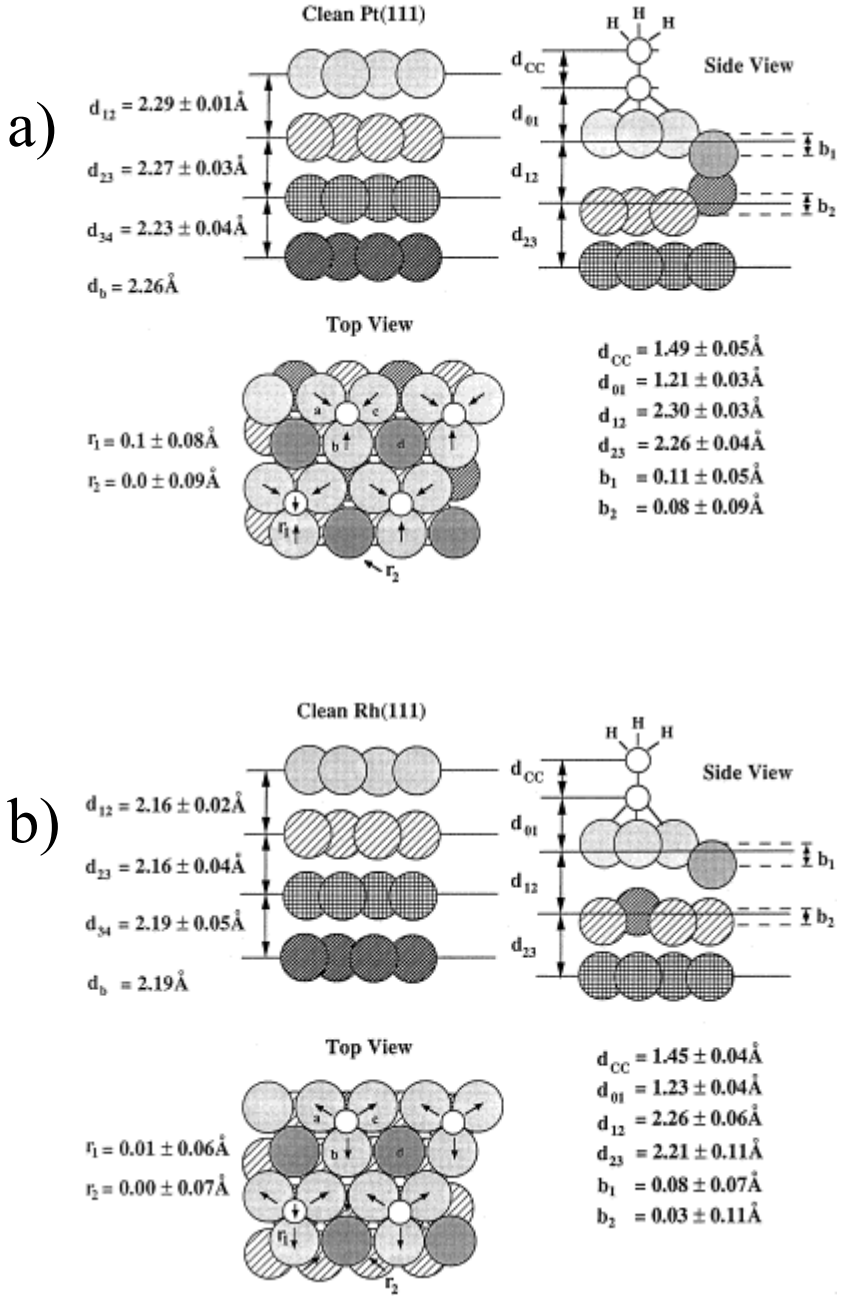

Figure 7.2 a) Structure of chemisorbed ethylidyne on Pt(111). b) Structure of chemisorbed ethylidyne on Rh(111). From [10].

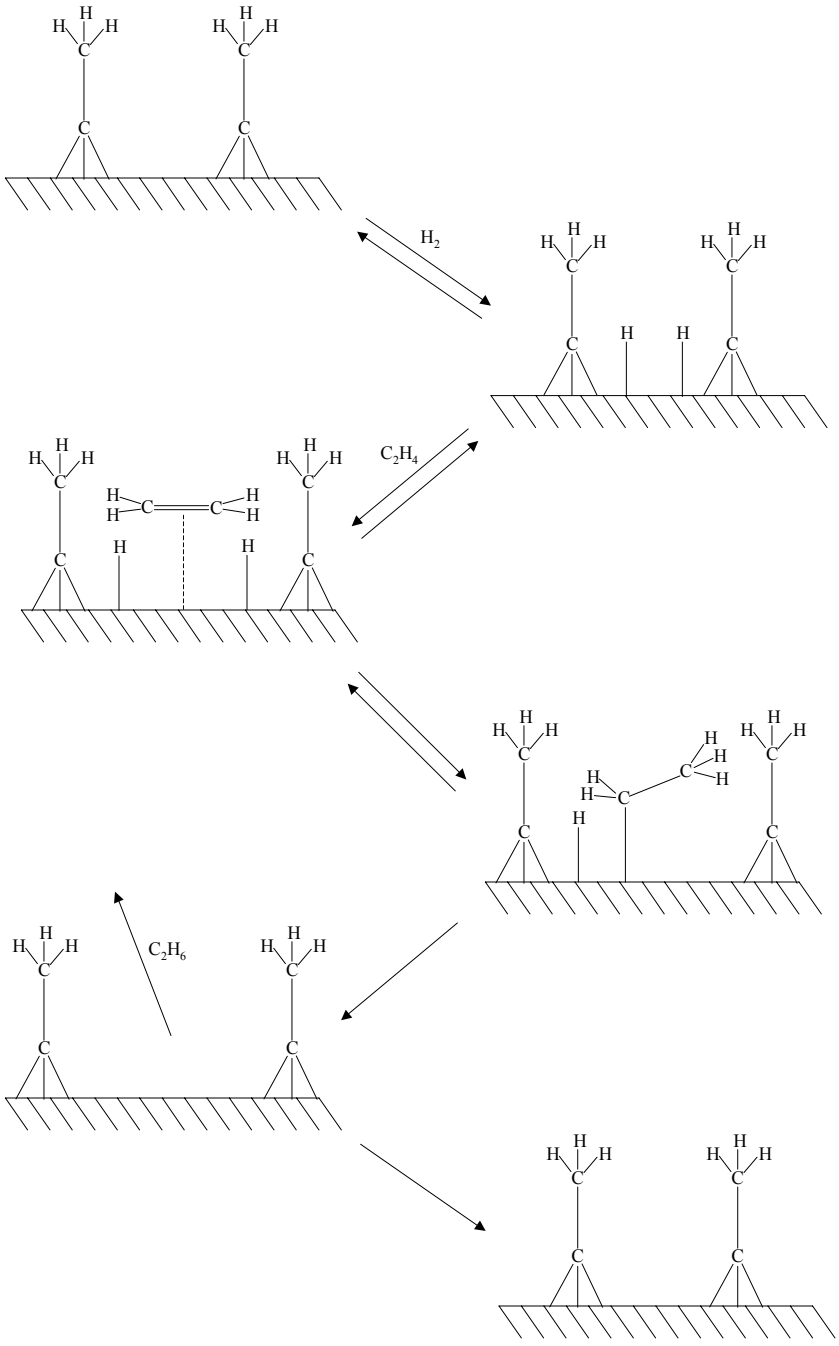

Figure 7.3 Proposed mechanism for ethylene hydrogenation on Pt(111) and Rh(111).

Isotope exchange experiments indicate that ethylidyne is a spectator [12]. π-bonded ethylene hydrogenation turnover accounts for most of the ethane that forms. Its concentration is only 4% of a monolayer. This mechanism was elucidated from experiments on Pt, and chemical reaction studies have shown that ethylidyne formation and stepwise hydrogenation of π-bonded ethylene are also mechanistically probable on Rh [13].

We discovered that CO, when introduced in the reaction chamber during ethylene hydrogenation, poisons the catalytic reaction. In this paper we discuss the experimental evidence for this poisoning effect and propose mechanisms that explain this interesting effect based on our studies of reaction rates using metal single crystals and metal nanoparticles on alumina. STM permits us to monitor the metal surfaces under reaction conditions.

7.2 Background

7.2.1 Reaction Rate Studies on Pt(111)

Yang et al. [14] studied the effect of CO on hydrogenation of ethylene to ethane over Pt(111) at temperatures between 400 and 523 K. Figure 7.4 shows the Arrhenius plot of ln[initial turnover frequency (TOF)] vs. 1/T for ethylene hydrogenation with (•) and without (■) CO over Pt(111), where TOF is defined as the number of ethane molecules generated per surface atom per second. Activation energies obtained from the slopes are 20.2 ± 0.1 and 9.6 ± 0.4 kcal/mol respectively. The result in the absence of CO is consistent with previous studies (10.8 kcal/mol for Pt(111) [12] and 9.9 kcal/mol for a Pt supported catalyst [15]).

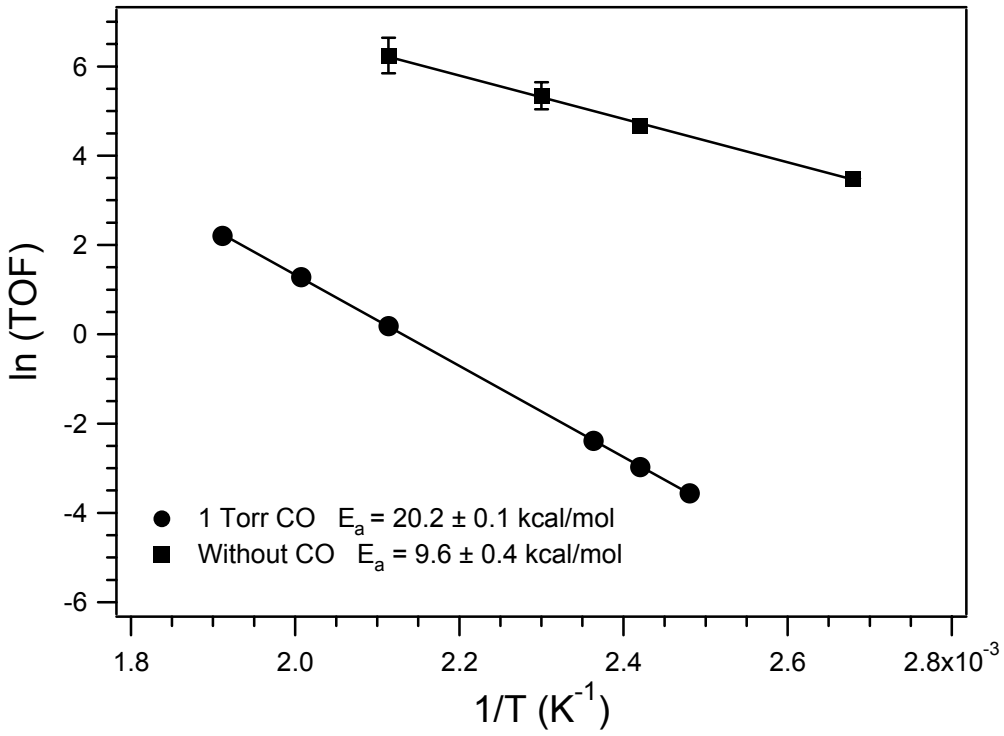

Figure 7.4 Logarithmic plot of turnover frequency (TOF) vs. 1/T for ethylene hydrogenation with (●) and without (■) CO over Pt(111): activation energies obtained from the slopes are 20.2 ± 0.1 and 9.6 ± 0.4 kcal/mol respectively.

The measured activation energy in the presence of CO, 20.2 ± 0.1 kcal/mol, is close to the desorption energy of CO on Pt(111). In the mTorr and above pressure range, CO is known to form a structure on the surface with a coverage of 0.60 ML [16]. At this coverage, the heat of adsorption of CO is 22 ± 4 kcal/mol [17]. The similarity between the ethylene hydrogenation activation energy and the CO adsorption energy will be shown to be due to CO blocking sites on the surface necessary for ethylene hydrogenation.

7.2.2 Reaction Rate Studies on Platinum Nanoparticles Deposited on Alumina

Zhu et al. [14] investigated the activation energies of ethylene hydrogenation reactions with and without CO on a Pt nanoparticle model catalyst from 313 to 523 K. An Al_2O_3-supported Pt nanoparticle array model catalyst with 28 ± 2 nm diameters and 100 ± 2 nm interparticle spacing was used. A field emission scanning electron microscope (FESEM) image of one such array is shown in Figure 7.5.

The reaction gas, which was recirculated, was 10 Torr C_2H_4, 100 Torr H_2, 800 Torr Ne, and varying amounts of CO. Generally speaking, the activity of Pt with 0.3 Torr of CO was less than 5% of the activity without CO at the same temperature. The temperature range investigated for ethylene hydrogenation without CO was from 313 to 423 K. Above 423 K, the reaction proceeds too fast to permit an accurate measurement of reaction rate. Since the catalytic activity of Pt was severely depressed in the presence of CO, the temperature range investigated for the hydrogenation reaction with CO was from 373 to 523 K. Below 373 K, the reaction was too slow and the catalytic reactivity

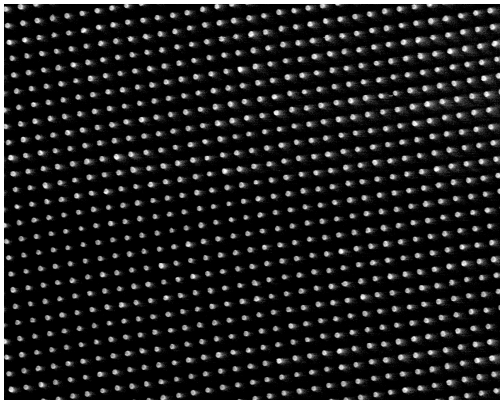

Figure 7.5 FESEM image of the platinum nanoparticle array showing a diameter of 28 ± 2 nm and a periodicity of 100 ± 2 nm.

was difficult to distinguish from the background reaction. Above 523 K side reactions become significant and compete with the ethylene hydrogenation pathway.

The Arrhenius plot for the ethylene hydrogenation with and without CO on the Pt nanoparticle model catalyst is shown in Figure 7.6. Assuming the geometrical shape of the nanoparticles and that all Pt sites are active, the metal surface area would be 7.0 mm^2. Previous work using the structure-insensitive ethylene hydrogenation reaction on the Pt nanoparticle array led to a calculated active metal surface area of 4.9 ± 2.5 mm^2 [18]. It is clear from the graph that the activation energy for ethylene hydrogenation without CO, 10.2 ± 0.2 kcal/mol, is practically the same as with 0.3 Torr CO, 11.4 ± 0.2 kcal/mol. Ethylene hydrogenation catalyzed by Pt nanoparticles in the presence of 0.6 Torr CO also yielded the same activation energy.

The difference between activation energies of ethylene hydrogenation on single crystals and nanoparticles in the presence of CO is interesting. It suggests that there are platinum sites in small concentration that are still available for ethylene hydrogenation on the nanoparticle arrays. Since CO hydrogenation is known to be enhanced at oxide-metal interfaces [19], these interface sites may remain free of CO and can continue hydrogenating ethylene.

7.3 Experimental

All STM experiments were performed in a high pressure, high temperature system combining a UHV surface analysis/preparation chamber with a variable pressure (10^{-10} to 10^3 Torr) and temperature (300 K to 675 K) STM. The base pressure of the system was 5×10^{-10} Torr, with the background made up primarily of H_2, CO, and water. The STM

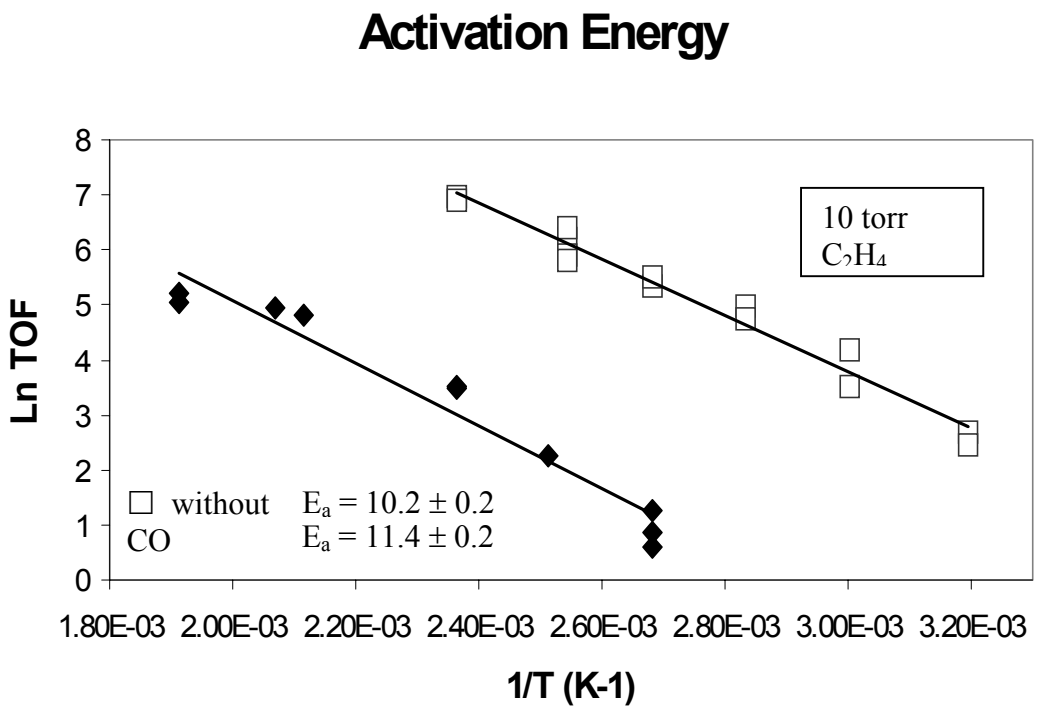

Figure 7.6 Arrhenius plot of the rate of ethylene hydrogenation on platinum nanoparticle arrays, with 0.3 Torr CO in the gas phase and without CO. The activation energy is 10.2 ± 0.2 kcal/mol without CO and 11.4 ± 0.2 kcal/mol with 0.3 Torr of CO.

chamber can be isolated by three gate valves and filled with any gas mixture. The composition of the gas in the STM chamber can be monitored by leaking gas through a feedthrough to the mass spectrometer on the UHV chamber. More specific capabilities of the instrument have been described in detail elsewhere [20].

The Rh(111) sample was prepared by sputtering with 400 eV oxygen ions for 10 minutes followed by annealing in vacuum at 973 K for 2 minutes. Just before the sample was exposed to the reaction gases, it was flashed again briefly to 973 K. The Pt(111) sample was prepared similarly, but was heated to 1133 K. The sample temperature in both cases was monitored with a chromel-alumel thermocouple mounted in the sample holder in contact with the edge of the crystal, and sample cleanliness was checked with Auger spectroscopy. The clean, room temperature sample was then transferred to the STM chamber. Large scale images of the sample showed steps with no preferred orientation, with a spacing that corresponds to a crystal miscut angle less than 1º. All experiments were performed at room temperature.

7.4 Results and Discussion

7.4.1 Ethylidyne and CO on Rh(111)

First, ethylidyne and CO coadsorption was studied on Rh(111). CO is known to also poison ethylene hydrogenation on Rh(111) [21]. Gas-phase ethylene is known to form ethylidyne on the surface of Rh(111) [7]. While ethylidyne forms ordered at low temperature and in vacuum conditions [22-24], at room temperature and above, ethylidyne is known to be too mobile on the surface of metal single crystals to be

observable by STM [8]. At low pressures and temperatures, CO is known to coadsorb with ethylidyne in a mixed c(4 × 2) structure [25], as shown in Figure 7.7.

STM experiments were performed the Torr and mTorr pressure range of ethylene and CO. Results showed that pure ethylidyne was not visible, as shown in Figures 7.8a and 7.8c. When CO was added, either 20 mTorr to 110 mTorr ethylene or 2 Torr to 10 Torr ethylene, an ordered structure appeared on the surface, as shown in Figures 7.8b and 7.8d. Further examination revealed that this ordered structure has a hexagonal (2 × 2) unit cell, as shown in Figure 7.9. This high-pressure structure is different from the mixed c(4 × 2) that has been imaged by STM in low-pressure conditions of CO and ethylidyne [26].

Unfortunately, we were unable to determine whether it is CO or ethylidyne that is being imaged by the STM. The corrugation, ~0.2 Å, is consistent with that of CO on Rh(111), but the corrugation of ethylidyne is unknown. While pure ethylidyne has been imaged by STM [8], the corrugation has never been measured. We also cannot positively determine that the structure is mixed CO and ethylidyne. It is possible that CO has simply displaced ethylidyne from the surface at these high pressures, as pure CO is known to form a (2 × 2) structure at these pressures [27]. If both CO and ethylidyne are on the surface, they could be segregated, as ethylidyne is known to form a (2 × 2) structure at low temperatures and pressures.

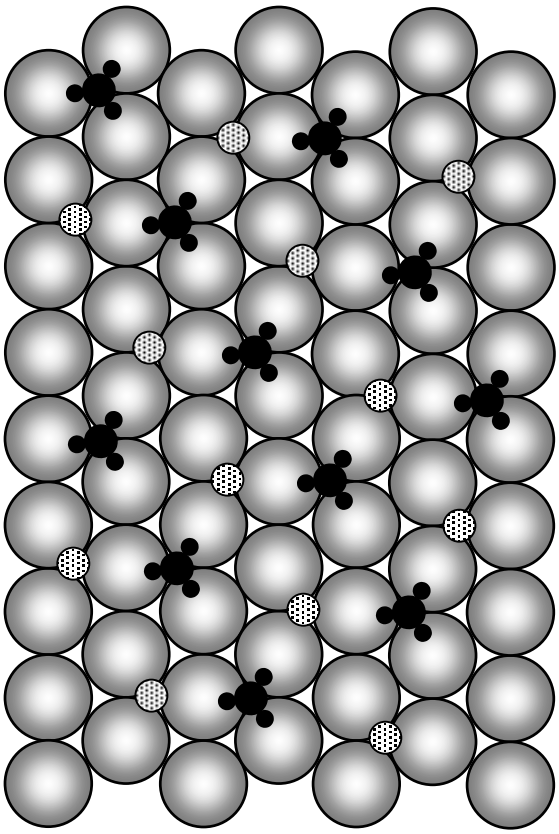

Figure 7.7 Coadsorbed ethylidyne (dark) and CO (shaded) on Rh(111) form a c(4 × 2) structure.

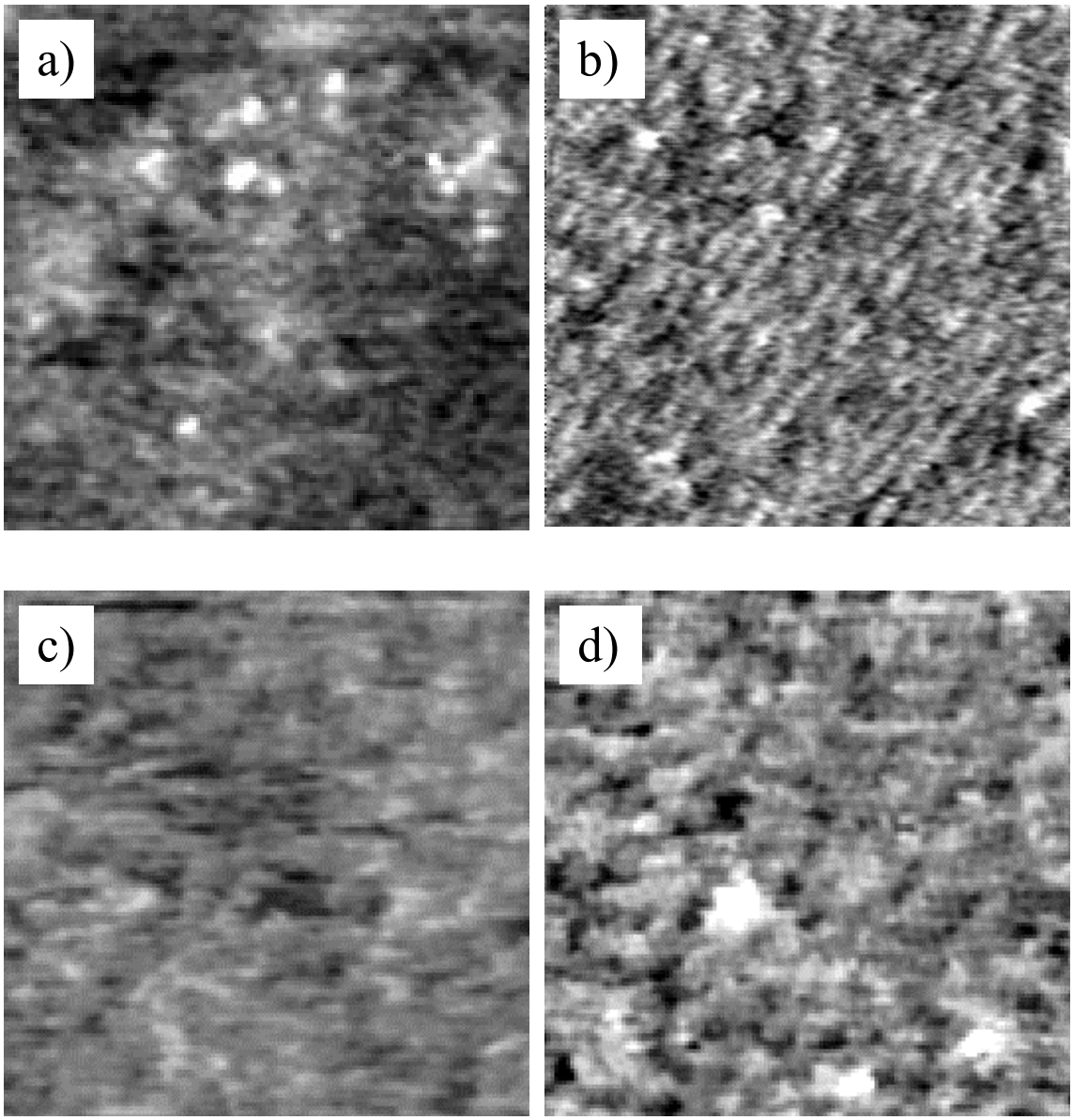

Figure 7.8 (100 Å)^2 STM images illustrating the ordering effect CO has on ethylidyne on Rh(111) taken in a) 110 mTorr ethylene; b) 110 mTorr ethylene + 20 mTorr CO; c) 10 Torr C_2H_4; d) 10 Torr ethylene + 2 Torr CO. The images in pure ethylene show no order, while those with CO show an ordered surface structure.

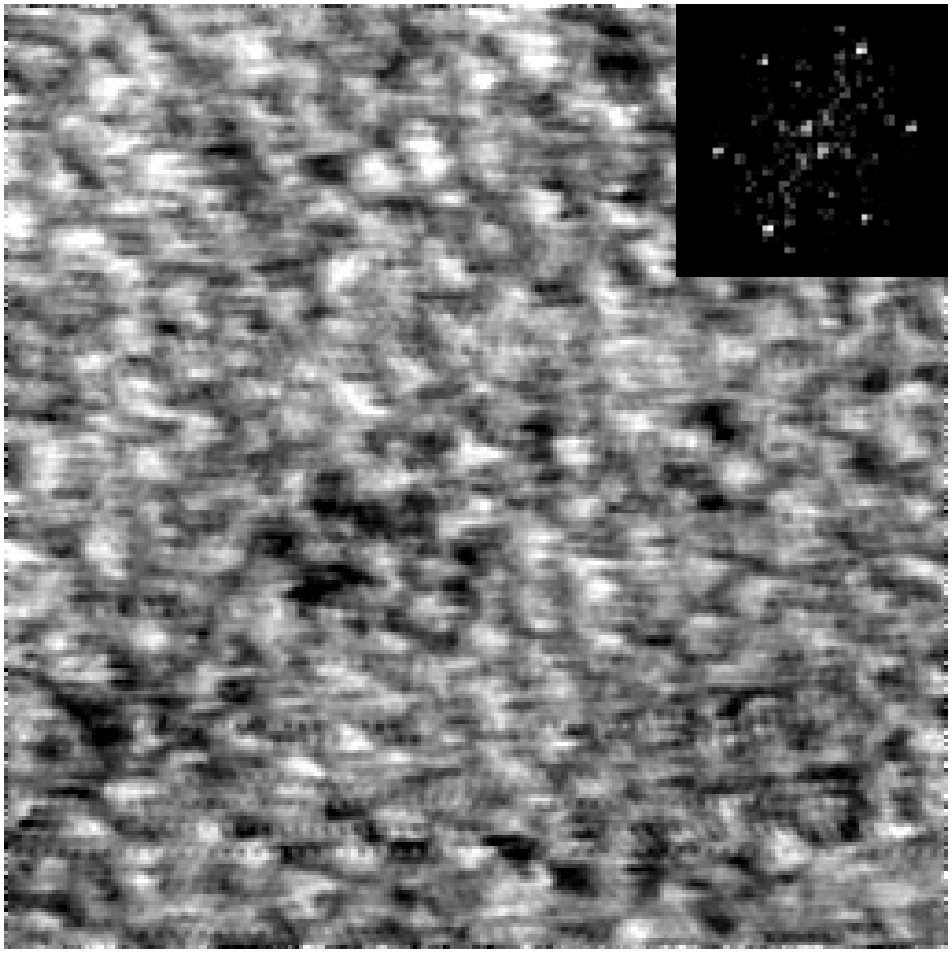

Figure 7.9 $(100\ \text{Å})^2$ STM image of the (2×2) hexagonal lattice formed in 100 mTorr ethylene and 10 mTorr CO. A fast Fourier transform (FFT) of the image, shown in the upper-right, further clarifies the hexagonal lattice.

7.4.2 Ethylene Hydrogenation and CO Poisoning on Rh(111)

Progressing to studying the ethylene hydrogenation reaction and its poisoning by STM led to much more definitive results. In these experiments, 20 mTorr of H_2 was first introduced, then 20 mTorr of ethylene, and finally 5 mTorr of CO.

When 20 mTorr of H_2 was introduced to a clean surface of Rh(111), no ordered structure was observed by STM, as shown in Figure 7.10a. This was expected as hydrogen adsorbs dissociatively at room temperature and the hydrogen atoms diffuse too quickly to be observed. After addition of 20 mTorr of ethylene to the hydrogen covered surface, no ordering could be observed in the images, as shown in Figure 7.10b, though SFG experiments have shown that ethylidyne is present on the surface under high pressures of hydrogen and ethylene [3]. Under these conditions the reaction rate can be measured with MS using the method described in Chapter 6. It is found to be 1.3×10^{-4} molecules site^{-1} s^{-1} at room temperature.

Addition of 5 mTorr CO to this mixture of hydrogen and ethylene, however, produced an ordered structure, as shown in Figure 7.10c. The ordered structure observed is the mixed c(4 × 2). SFG results have shown that under high pressures of hydrogen, ethylene, and CO, both CO and ethylidyne are on the surface [28]. Further evidence that the observed structure is mixed c(4 × 2) can be seen in Figure 7.11. In image b, the majority of the surface is covered with c(4 × 2) and appears light. The few patches that appear darker, one of which is outlined, are (2 × 2) of unknown composition. This shows that both CO and ethylidyne are on the surface, as otherwise only one structure would form. Comparison of the c(4 × 2) in image a, and that on the lower-left portion of image c, reveals that they are two different domains, rotated by 120º. This is expected due to

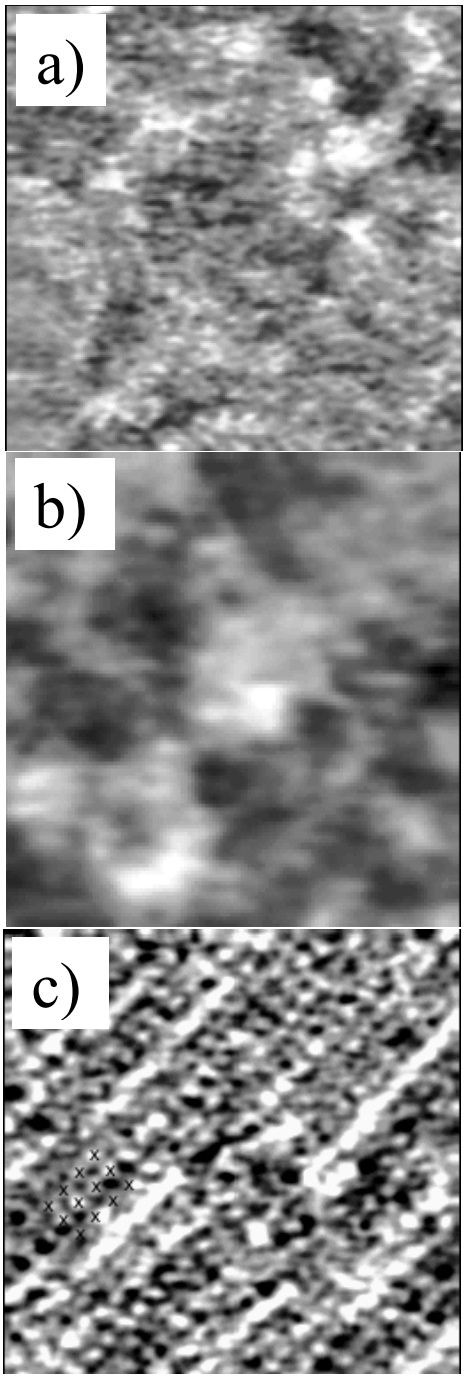

Figure 7.10 (100 Å)^2 STM images of Rh(111) taken under a) 20 mTorr H_2; b) 20 mTorr H_2 + 20 mTorr ethylene; c) 20 mTorr H_2 + 20 mTorr ethylene + 5 mTorr CO (I = 200 pA, V = 103 mV). An area of the rectangular c(4 × 2) structure has been marked with an "X" over each molecule. The images have been filtered to remove noise.

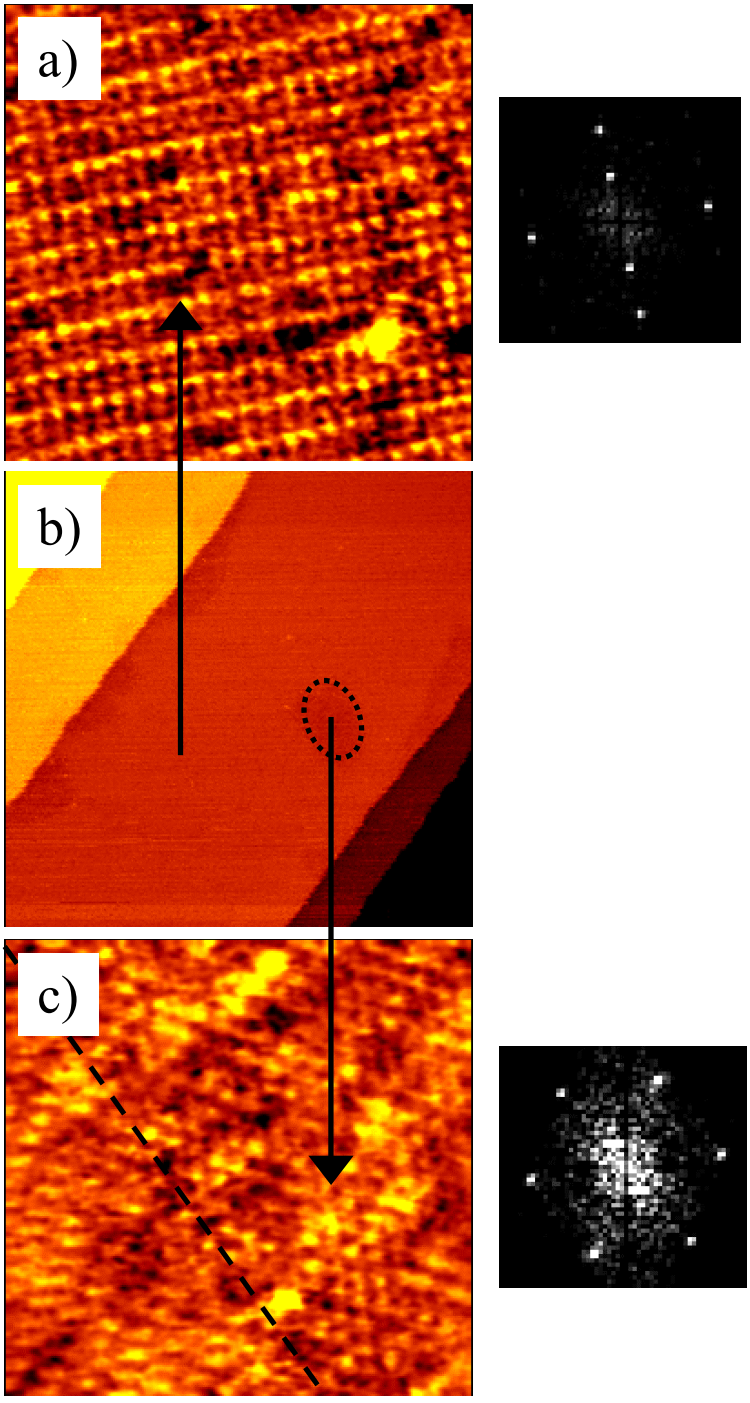

Figure 7.11 (100 Å)^2 STM images showing the predominant c(4 × 2) structure and patches of (2 × 2) on Rh(111) in 20 mTorr H_2 + 20 mTorr ethylene + 5 mTorr CO. Image b) is (1000 Å)^2 and shows that the surface is mostly c(4 × 2), shown in a). An FFT of the c(4 × 2) is shown next to the (100 Å)^2 image. A patch of (2 × 2) has been outlined and is shown c). An FFT of the (2 × 2) is shown next to the (100 Å)^2 image.

the rectangular periodicity of the unit cell compared to the hexagonal substrate lattice. Again, it is unknown whether CO or ethylidyne is being imaged. The periodicity measured in the c(4 × 2) structure indicates that only one or the other is being imaged. Like the high-pressure (2 × 2) described in the previous section, the corrugation is consistent for CO, but that does preclude ethylidyne. Once CO is introduced, ethylene hydrogenation is poisoned, and no further ethane can be detected.

7.4.3 Ethylene Hydrogenation and CO Poisoning on Pt(111)

Finally, ethylene hydrogenation and its poisoning by CO was studied on Pt(111) using STM. As for Rh(111), 20 mTorr of H_2 was first introduced, then 20 mTorr of ethylene, and finally 5 mTorr of CO.

Analogous to Rh(111), in 20 mTorr of H_2 is not visible on Pt(111) as it is too mobile at room temperature. Adding 20 mTorr ethylene did not cause any order to appear in the STM. Under these conditions, ethylene hydrogenation is occurring, as described earlier.

When 5 mTorr of CO is added, ethylene hydrogenation is poisoned, as described earlier. In the STM, an ordered structure appears, as shown in Figure 7.12. This structure is significantly different from the one seen on Rh(111). It is a hexagonal lattice with a unit cell length of about 11 Å. This is similar to a Moiré pattern seen in high pressures of pure CO on Pt(111) [16]. The corrugation is ~0.3 Å, consistent with that of CO on Pt(111). Further experiments are underway to better characterize the ordered structure under poisoned ethylene hydrogenation conditions.

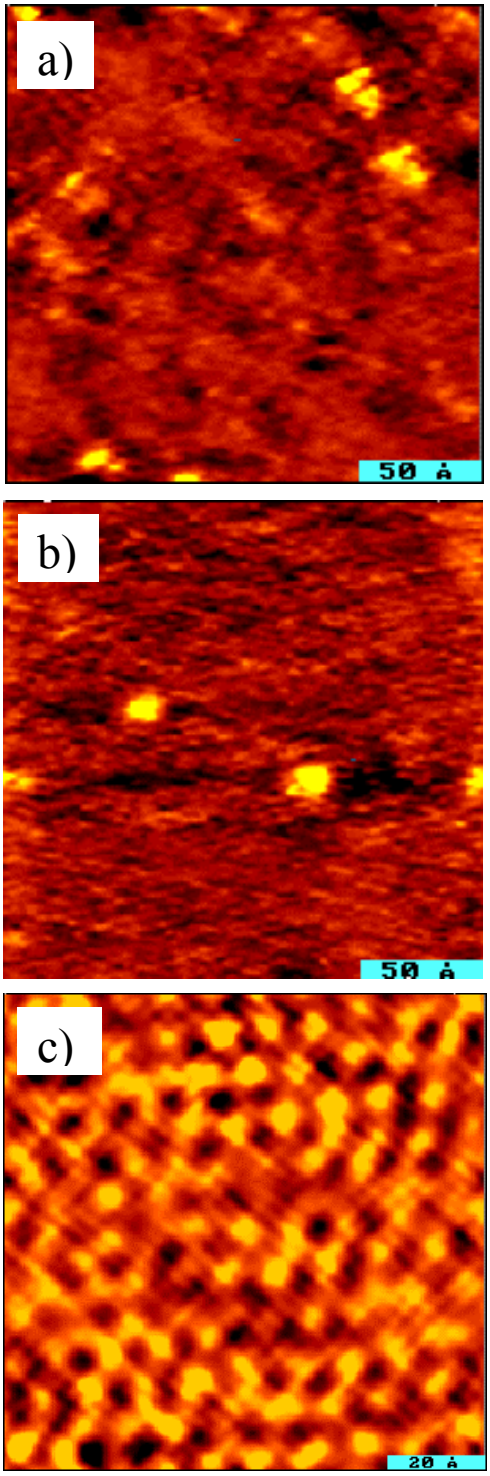

Figure 7.12 STM images of Pt(111) taken under a) 20 mTorr H_2, (200 Å)^2; b) 20 mTorr H_2 + 20 mTorr ethylene, (200 Å)^2; c) 20 mTorr H_2 + 20 mTorr ethylene + 5 mTorr CO, (100 Å)^2.

The observation of an ordered structure indicates that the ethylidyne on the surface has stopped diffusing on the surface. The time scale of an STM image is on the order of seconds, so an ordered image means that molecules are stationary on the surface for that amount of time. This lack of mobility would mean that vacant sites are not available for ethylene to adsorb, which would preclude ethylene hydrogenation. Thus, hydrogenation can only occur if some of the CO molecules desorb. This is why the activation energy for ethylene hydrogenation becomes that of the heat of desorption of carbon monoxide when it is poisoned.

7.5 Conclusions

We have studied CO poisoning of ethylene hydrogenation on rhodium and platinum single crystals as well as on platinum nanoparticles in the mTorr and Torr pressure regimes. GC studies on Pt(111) have shown that CO poisons the reaction, and the activation energy increases from 10.8 to 20.2 kcal/mol. This CO-poisoned activation energy is near the desorption energy of CO. Only when CO molecules desorb can ethylene hydrogenation take place and thus the activation energy for the reaction becomes similar to the heat of desorption for CO.

Studies of CO poisoning on platinum nanoparticles showed a decrease in activity when CO was present, but not a significant increase in activation energy. This suggests that the oxide-metal interface sites that are present in small concentration remain active for ethylene hydrogenation because they remain free of adsorbed CO.

STM studies of CO and ethylidyne on Rh(111) showed that pure ethylidyne is not visible at room temperature, as it is too mobile. Adding CO causes a high-pressure (2 × 2) structure to form, though details about the structure remain elusive.

STM studies of the ethylene hydrogenation system on Rh(111) show that when CO is introduced to a surface covered with hydrogen and ethylidyne, ordered structure appears on the surface, poisoning the reaction. The surface is predominantly mixed c(4 × 2), though there are some areas of (2 × 2). Analogous studies on Pt(111) also show that CO poisons ethylene hydrogenation and causes the adsorbates to order. However, the structure is hexagonal and resembles the Moiré pattern seen on Pt(111) in high pressures of pure CO.

Based on these results, we have proposed a model for CO poisoning on single crystals in which CO adsorbs on vacant hollow sites, preventing the diffusion of ethylidyne. With the immobile adsorbates filling the surface, there is no room for ethylene to adsorb, and hence ethylene hydrogenation cannot occur.

References

(1) For a review see: J. Horiuti, K. Miyahara, *Hydrogenation of Ethylene on Metallic Catalysts*, NSRDS-NBS, Vol. 13, 1968.

(2) Polanyi, M.; Horiuti, J. *Trans. Faraday Soc.* **1934**, *30*, 1164.

(3) Cremer, P. S.; Su, X. C.; Shen, Y. R.; Somorjai, G. A. *J. Am. Chem. Soc.* **1996**, *118*, 2942-2949.

(4) Doll, R.; Gerken, C. A.; Van Hove, M. A.; Somorjai, G. A. *Surf. Sci.* **1997**, *374*, 151-161.

(5) Cremer, P.; Stanners, C.; Niemantsverdriet, J. W.; Shen, Y. R.; Somorjai, G. *Surf. Sci.* **1995**, *328*, 111-118.

(6) Starke, U.; Barbieri, A.; Materer, N.; Vanhove, M. A.; Somorjai, G. A. *Surf. Sci.* **1993**, *286*, 1-14.

(7) Wander, A.; Van Hove, M. A.; Somorjai, G. A. *Phys. Rev. Lett.* **1991**, *67*, 626-628.

(8) Land, T. A.; Michely, T.; Behm, R. J.; Hemminger, J. C.; Comsa, G. *J. Chem. Phys.* **1992**, *97*, 6774-6783.

(9) Nomikou, Z.; Van Hove, M. A.; Somorjai, G. A. *Langmuir* **1996**, *12*, 1251-1256.

(10) Van Hove, M. A.; Somorjai, G. A. *J. Mol. Catal. A-Chem.* **1998**, *131*, 243-257.

(11) Ge, Q.; King, D. A. *J. Chem. Phys.* **1999**, *110*, 4699-4702.

(12) Zaera, F.; Somorjai, G. A. *J. Am. Chem. Soc.* **1984**, *106*, 2288-2293.

(13) Ellison, P.; Feinberg, M.; Yue, M. H.; Saltsburg, H. *J. Mol. Catal. A-Chem.* **2000**, *154*, 169-184.

(14) Hwang, K. S.; Yang, M.; Zhu, J.; Grunes, J.; Somorjai, G. A. *J. Molec. Catal. A* **submitted for publication**.

(15) Bond, G. C. *Transactions of the Faraday Society* **1956**, *52*, 1235-1244.

(16) Jensen, J. A.; Rider, K. B.; Salmeron, M.; Somorjai, G. A. *Phys. Rev. Lett.* **1998**, *80*, 1228-1231.

(17) Yeo, Y. Y.; Vattuone, L.; King, D. A. *J. Chem. Phys.* **1997**, *106*, 392-401.

(18) Grunes, J.; Zhu, J.; Anderson, E. A.; Somorjai, G. A. *Journal of Physical Chemistry B* **2002**, *106*, 11463-11468.

(19) Levin, M. E.; Salmeron, M.; Bell, A. T.; Somorjai, G. A. *J. Catal.* **1987**, *106*, 401-409.

(20) Jensen, J. A.; Rider, K. B.; Chen, Y.; Salmeron, M.; Somorjai, G. A. *J. Vac. Sci. Technol. B* **1999**, *17*, 1080-1084.

(21) Bent, B. E. *Ph.D. Thesis, University of California* **1986**.

(22) Steininger, H.; Ibach, H.; Lehwald, S. *Surf. Sci.* **1982**, *117*, 685-698.

(23) Koestner, R. J.; Frost, J. C.; Stair, P. C.; Vanhove, M. A.; Somorjai, G. A. *Surf. Sci.* **1982**, *116*, 85-103.

(24) Stair, P. C.; Somorjai, G. A. *J. Chem. Phys.* **1977**, *66*, 2036-2044.

(25) Blackman, G. S.; Kao, C. T.; Bent, B. E.; Mate, C. M.; Van Hove, M. A.; Somorjai, G. A. *Surf. Sci.* **1988**, *207*, 66-88.

(26) Cernota, P. D. *Ph.D. Thesis, University of California* **1999**.

(27) Cernota, P.; Rider, K.; Yoon, H. A.; Salmeron, M.; Somorjai, G. *Surf. Sci.* **2000**, *445*, 249-255.

(28) Kung, K. Y. *Ph.D. Thesis, University of California* **2000**.

Chapter 8: Concluding Remarks

This chapter summarizes the results and discussion of the previous chapters and discusses the future of the high-pressure, high-temperature STM project.

8.1 Summary

In this dissertation, an HPHTSTM was used to study model catalysts for the automobile catalytic converter and ethylene hydrogenation. High-pressure surface structures and reactions were studied.

High-pressure structures of NO were studied on Rh(111). In the mTorr pressure range below 0.03 Torr, NO forms a (2 × 2)-3NO structure, which is known from low-pressure surface science experiments. At approximately 0.03 Torr, NO undergoes a phase transformation to a new (3 × 3) structure, which only forms in equilibrium with the gas phase at high pressure. The corrugation of the (3 × 3) structure is significantly greater than that of the (2 × 2), and its absolute height is also higher, suggesting that the metal reconstructs under the (3 × 3) structure. By observing the time scale of the reversible phase transformation between the two surface structures, the energy barrier between the two was calculated to be 0.7 eV. By directly observing the phase transition at several temperatures and pressures, a phase diagram was constructed, and the heat of adsorption in the new structure was measured to be 0.9 ± 0.1 eV.

High-pressure coadsorption of CO and NO on Rh(111) was studied using STM in the catalytically important pressure regime. For low NO partial pressures, the molecules mix into a (2 × 2)-3(CO-NO) structure. I this mixed structure, top-site NO appears 0.3 Å higher than top-site CO. The number of top-site NO molecules increases as the NO

partial pressure increases. By comparing the equilibrium concentrations of top-site molecules and gas-phase molecules, we find that top-site CO is more stable than top-site NO by 66 ± 5 meV.

Occasionally neighboring CO and NO top-site molecules appear to exchange places. Based on the low rate of these exchanges and the NO pressure necessary to produce bright NO spots in the images, we have proposed a model where NO substitutes for CO in the hollow sites first and then on the top sites later. Molecular desorption is required for these exchange events, and desorption from the top sites occurs at frequencies of the order of 10^{-5} s^{-1}, which implies an adsorption energy of 1.0 eV. The exchange between neighboring CO and NO top sites is explained by a vacancy-mediated diffusion mechanism, though the details are not presently understood.

NO molecules appear to slightly prefer occupying adjacent top-sites in the (2 × 2) lattice, which causes the formation of NO-rich islands at higher NO partial pressures. The presence of CO in the gas phase increases the NO partial pressure that is necessary for the formation of the NO (3 × 3) structure until the NO partial pressure is three to five times greater than the CO partial pressure. When the (3 × 3) structure forms, it nucleates on the NO-rich areas mentioned above.

The reaction of CO and NO was then studied on Rh(111) using the STM and mass spectrometer. Using a feedthrough from the high-pressure STM chamber to the MS on the UHV chamber, the reaction was monitored from 473 K to 533 K. By measuring the rates at different temperatures, the apparent activation energy was found to be 34 kcal/mol. There is a side reaction producing N_2O that we did not account for, which probably explains why our result is higher than theoretical predications. STM results

showed that steps edges remained sharp until the temperature was increased to 473 K. Then the steps blurred, possibly due adsorbate-induced metal atom mobility. As the temperature continued to increase, metal atom mobility slowed, and the steps regained their distinct edges. The lower the pressure, the lower the temperature at which this occurred, suggesting that many molecules need to be adsorbed before there is a high degree of metal atom mobility.

CO poisoning of ethylene hydrogenation on rhodium and platinum single crystals as well as on platinum nanoparticles was studied in the mTorr and Torr pressure regimes. GC studies on Pt(111) have showed that CO poisons the reaction, and the activation energy increased from 10.8 to 20.2 kcal/mol. This CO-poisoned activation energy is near the desorption energy of CO. This suggests that ethylene hydrogenation can take place only after CO molecules desorb. This is why the activation energy for the reaction becomes similar to the heat of desorption for CO.

STM studies of the ethylene hydrogenation system on Rh(111) show that when CO is introduced to a surface covered with hydrogen and ethylidyne, ordered structure appears on the surface, poisoning the reaction. The surface is predominantly mixed c(4 × 2), though there are some areas of (2 × 2) of unknown composition. Analogous studies on Pt(111) also show that CO poisons ethylene hydrogenation and causes the adsorbates to order. However, the structure is hexagonal and resembles the Moiré pattern seen on Pt(111) in high pressures of pure CO. STM studies of CO and ethylidyne on Rh(111) showed while pure ethylidyne is too mobile to be visible at room temperature, adding CO causes a high-pressure (2 × 2) structure to form, though details about the structure remain elusive.

Based on these results, we have proposed a model for CO poisoning on single crystals in which CO adsorbs on vacant hollow sites, preventing the diffusion of ethylidyne. With the immobile adsorbates filling the surface, there is no room for ethylene to adsorb, and hence ethylene hydrogenation cannot occur.

8.2 Future Directions

This dissertation demonstrated that HPHTSTM can be used to examine surface structures that do not form in low-pressure conditions and help elucidate atom and molecule mobility during reactions. Concerning poisoning, other reactions can be studied, such as cyclohexene hydrogenation/dehydrogenation. This dissertation dealt with (111) surfaces, which are generally the most stable. Moving to more open surfaces such as Rh(110), as shown in Figure 1.2, may allow reactions like those in the automobile catalytic converter to be studied in temperature ranges where molecular resolution is still achievable. New HPHTSTMs may be able to image in up to 20 atm of gas. This would enable reactions such as ammonia synthesis to be studied under realistic pressure conditions.